The Dissertation Committee for Bingqing Wang Certifies that this is the approved version of the following dissertation:

Optical Designs and Image Processing Algorithms for Optical Coherence Tomography Detection of Glaucoma

Committee:

Henry G. Rylander III, Co-Supervisor

Thomas E. Milner, Co-Supervisor

James W. Tunnell

Andrew K. Dunn

Alan C. Bovik

Optical Designs and Image Processing Algorithms for Optical Coherence Tomography Detection of Glaucoma

by

Bingqing Wang, B.E.

Dissertation

Presented to the Faculty of the Graduate School of

The University of Texas at Austin

in Partial Fulfillment

of the Requirements

for the Degree of

Doctor of Philosophy

The University of Texas at Austin

August 2014

Dedication

To my parents Jianjun Wang and Yingying Yao who inspired me every time when I was trapped in difficulty. To my wife Liang Sun who always stood by my side sharing life's joy's and challenges.

Acknowledgements

I would like to thank my supervisors Dr. Henry G. Rylander III and Dr. Thomas E. Milner. Dr. Rylander is the most knowledgeable ophthalmologist I have ever seen. He walked me through the amazing world of eye physiology and medical devices. Without Dr. Rylander's help, I would never be able to extract any information from my clinical and animal studies.

Dr. Milner is a great scientist, engineer, and inventor. He trained me how to design and build an optical system, solved problems with me step by step when I was in trouble, guided me to bring academic research to solve real-world problems, and most importantly, taught me to view a problem logically and creatively.

I would like to thank Dr. Mia K. Markey for her helpful advices on the statistical analysis of my research data.

Many thanks go to Dr. Andrew K. Dunn, Dr. James W. Tunnell, and Dr. Alan C. Bovik for their kind service on my dissertation committee and helpful suggestions on improving the quality of this dissertation.

Thanks to my colleagues and friends in Biomedical Engineering Laser Laboratory. As my first PhD project, Badr Elmannaoui and Biwei Yin introduced me to polarization-sensitive optical coherence tomography. Later, I worked with Amit Paranjape and Shuang Liu on a clinical study, and with Jordan Dwelle on an animal study. Austin McAlroy and Andrew Klotz helped me in an image processing project. Besides, Jinze Qiu, Sahar Elahi, Tianyi Wang, and Bharadwaj Muralidharan also helped me on certain projects. It had been a joyful journey with all of them.

The work in the dissertation would be impossible without the support from Animal Research Center (ARC). Special thanks to ARC staffs who took care of the animals used in my research: Elena Lightfeather, Philip Koch, Andrew Tinsley, and Ricky Meyers.

I would like to acknowledge the undergraduate researchers who helped with my research: Stephanie Toeh, Daniel Joh, Kyleigh Futrell, Amy Mistry, and Carter Melton. I could never finish my projects on time without their great assistance on animal preparation and data processing.

Finally, I am deeply grateful to my family. My parents Jianjun Wang and Yingying Yao inspired me to pursue my dream of studying in a top graduate school half an earth away from home and unconditionally supported me throughout my life. My wife Liang Sun has been always taking care of me with great patience and encouraging me with endless love. I hope to express my deepest love to my family without whom I could never go this far.

Optical Designs and Image Processing Algorithms for Optical Coherence Tomography Detection of Glaucoma

Bingqing Wang, Ph.D.

The University of Texas at Austin, 2014

Co-Supervisor: Henry G. Rylander III

Co-Supervisor: Thomas E. Milner

Optical Coherence Tomography (OCT) is an optical tomography technique which provides high resolution non-invasive three-dimensional (3D) structural images of the sample based on coherent properties of light. The dissertation focuses on the use of OCT systems for detecting glaucoma, which is the second leading cause of blindness worldwide. First, as a prerequisite of analyzing ophthalmologic OCT images, a retinal sublayer segmentation algorithm is presented and implemented with GPU assisted computation. Then, a polarization-sensitive optical coherence tomography (PS-OCT) system was constructed for the study of glaucoma. Three closely related clinical and animal studies on early-stage glaucoma detection using either OCT or PS-OCT were performed. Statistical analysis of the study results indicates that the scattering property of retinal nerve fiber layer (RNFL) is the earliest indicator for glaucoma. Finally, to investigate the scattering properties of RNFL, a pathlength-multiplexed scattering-angle-diverse optical coherence tomography (PM-SAD-OCT) system was designed and built. PM-SAD-OCT images were collected from human and rodent retina as well as earthworm nerve cord. PM-SAD-OCT system shows promising potentials to detect neurodegenerative diseases including glaucoma.

Table of Contents

List of Tables

List of Figures

Chapter 1: Introduction

1.1. Organization of Dissertation

The dissertation focuses on the use of Optical Coherence Tomography (OCT) systems for glaucoma detection. It includes 5 chapters. Chapter 1 briefly introduces the physiology of human eyes and pathophysiology of glaucoma. Then, history and principles of optical coherence tomography (OCT) and its application in ophthalmology, especially glaucoma diagnostics, are reviewed.

Chapter 2 focuses on image processing of OCT retinal images. Segmentation of retinal sublayers is a prerequisite to analyze any ophthalmologic OCT images. A fully automatic three-dimensional (3D) multiphase active contour segmentation algorithm implemented with GPU assisted computation is presented in Chapter 2. The algorithm simultaneously detects all retinal sublayers in noisy environments with high accuracy. The proposed algorithm shows promising clinical value in segmenting and analyzing noisy ophthalmologic OCT images.

Chapter 3 describes polarization-sensitive optical coherence tomography (PS-OCT). PS-OCT extends the functionality of standard intensity OCT with measuring the polarimetric properties of the sample. The PS-OCT system and polarimetric processing algorithm are briefly described. PS-OCT has many potential advantages over standard OCT in glaucoma diagnostics by providing additional diagnostic information about the retinal nerve fiber layer (RNFL) birefringence and phase retardation.

Chapter 4 summarizes the results of three closely related clinical and animal studies related to early-stage glaucoma detection using either OCT or PS-OCT. The common objective of the three studies is to find the best parameter to detect early-stage glaucoma. According to the study results, a new measurement – RNFL reflectance –

outperforms any other glaucoma indicator including RNFL thickness, birefringence, and phase retardation. Although the underlying mechanism between RNFL reflectance changes and glaucoma progression remains unclear, a possible hypothesis is proposed.

Chapter 5 introduces another functional OCT methodology called pathlength-multiplexed scattering-angle-diverse optical coherence tomography (PM-SAD-OCT). A PM-SAD-OCT system is constructed to investigate the scattering properties of the sample and shows promising potential to detect neurodegenerative diseases including glaucoma. PM-SAD-OCT images are acquired from a) *in vivo* retina of healthy human subjects, b) *ex vivo* retina of rodents during retina degeneration, and c) *in vitro* nerve cord of earthworms during neurodegeneration. Application of PM-SAD-OCT may provide potentially valuable diagnostic information for clinical glaucoma diagnostics.

1.2. HUMAN EYE AND GLAUCOMA

1.2.1. Anatomy of Human Eye

As one of the most remarkable optical systems in the universe, the human eye reacts to light and produces vision. The eye is structurally and functionally viewed as having two principal anatomical segments: the anterior and posterior segments. If the whole eye is viewed as analogous to a camera, then the anterior segment functions as the camera lens which focuses the light onto the retina, while the posterior segment functions as the film which senses the light image, intensity and color.

Principal structures in the anterior segment include the cornea, iris, and lens (Figure 1). The region bounded between cornea and iris forms anterior chamber which is filled with aqueous humor. The region between iris and lens forms the posterior chamber which is filled with vitreous humor. Due to their relatively higher refractive indices, the

cornea and lens form a positive optical lens which refracts the light incident through the iris, and focuses the image onto the retina.

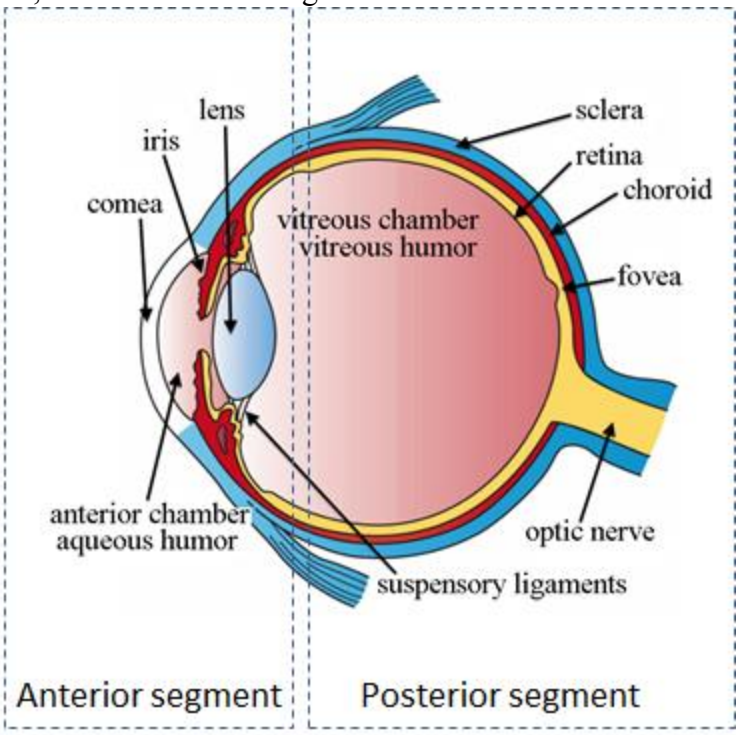

Figure 1: Anatomy of human eye [1].

The posterior segment includes vitreous humor, retina, optic nerve, and choroid (Figure 1). The retina is the anatomical element that senses the light and consists of multiple sublayers (Figure 2), including retinal nerve fiber layer (RNFL), inner plexiform layer (IPL), inner nuclear layer (INL), outer plexiform/nuclear layer (OPL/ONL), inner/outer segment photoreceptor layer (IS/OS), and retinal pigment epithelium (RPE). Among these retinal sublayers, RNFL, which is the most anterior sublayer, has a significant clinical diagnostic importance, because RNFL morphology is associated with various neurodegenerative diseases including glaucoma. RNFL is mainly composed of axon bundles of retinal ganglion cells (RGCs) as well as blood vessels which supply the

inner retina. The RGC axons in RNFL contain high density of microtubules and mitochondria, both of which are essential to maintain the functionality of RGC axons (Figure 3) [2]. RGC axons exit the eye through the optic nerve head (ONH), which forms a blind spot in the visual field.

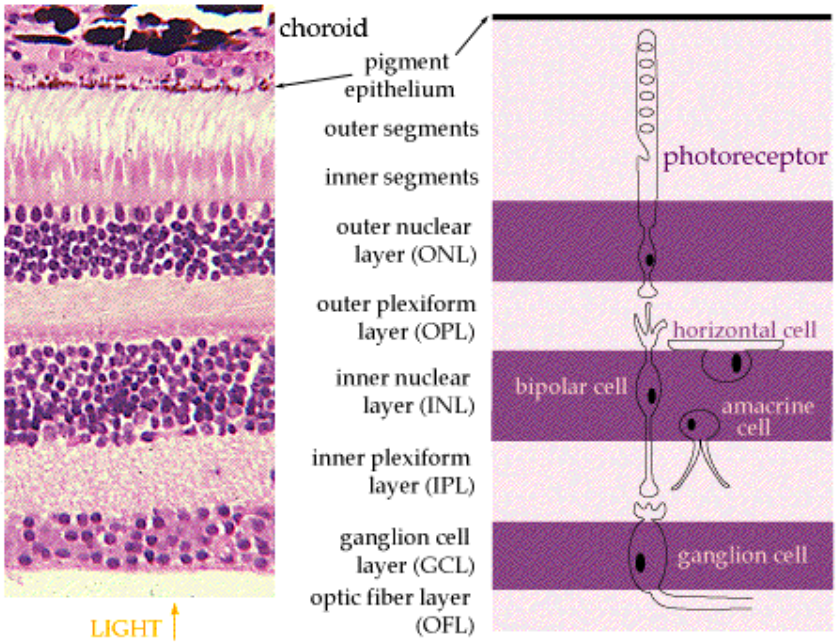

Figure 2: Anatomy of human retina [3].

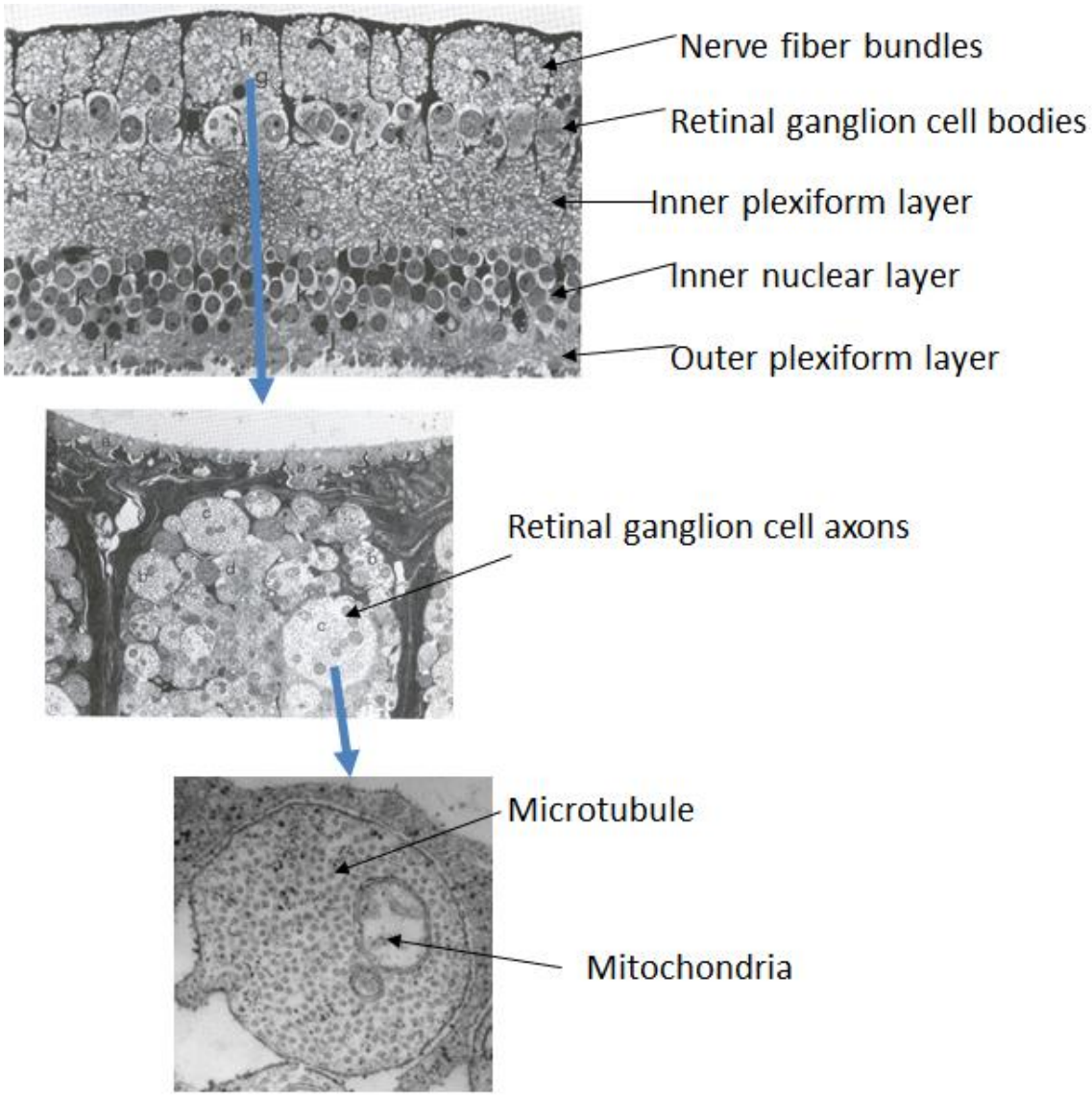

Figure 3: Transmission electron microscopy (TEM) histologic images of non-human primate retina at increasing zoom level [2].

1.2.2. Glaucoma

As a common group of ocular disorders, glaucoma is characterized by a progressive and irreversible loss of retinal ganglion cells (RGCs) and their axons in the retinal nerve fiber layer (RNFL). The axons are responsible for transmitting information from photoreceptor cells into the brain. The loss of these important signal transmitters

causes progressive loss of the visual field and eventually blindness if not arrested [4]. Glaucoma is considered to be the second leading cause of blindness worldwide after cataract [5, 6]. The mechanism of glaucomatous progression and damage is not yet fully understood. Traditionally glaucoma was considered to be caused by elevated intraocular pressure (IOP) [7]. Although elevated IOP is the most important and only modifiable risk factor for glaucoma, elevated IOP is neither sufficient nor necessary for clinical glaucoma diagnostics: some subjects may have high IOP but never develop glaucomatous damage, while others may develop glaucomatous damage at a relatively low IOP. Recently, numerous glaucomatous damage mechanisms have been proposed including ischemic changes [8], astrocytic reaction [9-11], autoimmune attack [12], and reactive ion species and nitric oxide metabolism [13, 14].

Although the mechanism of glaucomatous progression remains unclear, effective pharmacological interventions, e.g. Combigan, and surgical procedures, e.g. trabeculectomy for glaucoma are available to arrest the axonal degeneration in glaucoma. So, early treatment preventing irreversible vision loss is possible if objective and sensitive diagnostic techniques become available to assess the RNFL.

Currently, multiple techniques including tonometry, visual field testing, optic nerve evaluation, and optic nerve imaging have been applied in order to detect glaucoma before vision loss is noticed subjectively by the patient. However, due to the limited sensitivity and specificity of the current diagnostic techniques, an estimated 50% of glaucoma cases in the USA are undiagnosed [15].

The goal of the dissertation is to explore new diagnostic tools for early stage glaucoma detection. Two promising diagnostic techniques are proposed based on measuring the birefringence and scattering properties of RNFL. Besides the techniques

proposed in the dissertation, another promising glaucoma diagnosis has been proposed recently based on characterizing ONH blood flow [16, 17].

1.3. OPTICAL COHERENCE TOMOGRAPHY (OCT)

Optical Coherence Tomography (OCT) is an optical tomography technique which provides high resolution non-invasive three-dimensional (3D) structural images of the sample based on coherent properties of light. Because of its capability of 3D non-invasive imaging and resolution advantages over competing approaches, OCT has quickly gained wide application in medical diagnostics, especially in ophthalmic and cardiovascular imaging.

1.3.1. Time Domain OCT

OCT was first demonstrated in 1991 as a time domain approach [18] and transformed to the Fourier domain later [19, 20]. Time domain OCT (Figure 4) is typically based on a two-beam interferometer (e.g., Michelson interfereometer) with a low coherence laser or superluminescent diode light source. Light from the source is divided into two paths by a beam splitter. Sample is fixed in the sample arm, while a reflective mirror on a translational stage is found in the reference arm. Light backscattered from the sample and reference is combined again at the beam splitter and interferes with each other. Interference signal is acquired by a photodetector in the detection arm. The reference mirror translates along beam axis in reference arm to vary the optical pathlength and form a depth scan or A-scan that contains information on depth-resolved reflected signal strength from the sample. A two-dimensional scan or B-scan is acquired by scanning the beam laterally on the sample, usually with a galvanometer scanner. The acquisition speed of time domain OCT is constrained by the moving mirror in the reference arm, which needs to be mechanically scanned.

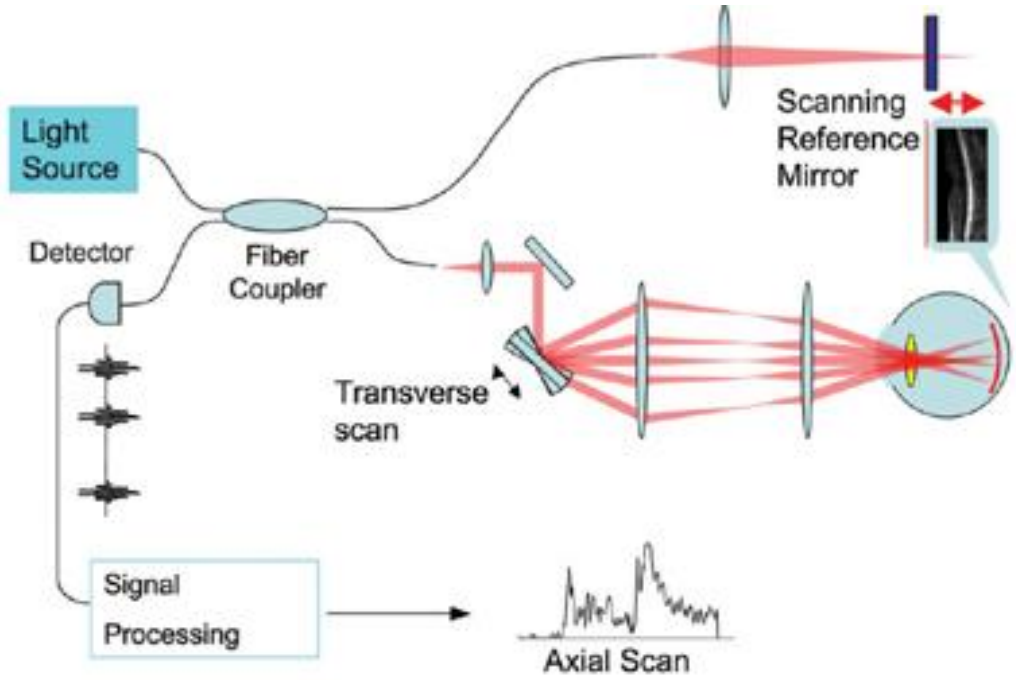

Figure 4: Schematic of a basic time domain OCT [21].

1.3.2. Fourier Domain OCT

Fourier domain OCT has a similar basic structure as time domain OCT, except that Fourier domain OCT records the spectrum of the backscattered and interfering light. According to the Wiener-Khinchin theorem, the depth-resolved information of the sample is coded into the spectrum of the interference signal via an inverse Fourier Transform. Fourier domain OCT shows significant advantages over time domain OCT in terms of acquisition speed, because Fourier domain OCT does not require a moving reference mirror which limits the acquisition speed in time domain OCT. Two types of Fourier domain OCT have been proposed, corresponding to two instrumentation approaches to obtain the spectrum of the interference signal: spectral domain OCT (SD-OCT) uses a spectrometer to record the spectrum (Figure 5), while swept source OCT (SS-OCT) uses a wavelength tunable laser source to encode the spectrum in time by

rapidly tuning the wavelength of laser light (Figure 6). SS-OCT is usually equipped with balanced photodetector, therefore has sensitivity advantages over SD-OCT. As a point detector, the balanced photodetector in an SS-OCT also provides a higher acquisition rate compared with SD-OCT using a relatively slower spectrometer. Recently, using a Fourier domain mode locked (FDML) laser, a SS-OCT with A-scan rate up to 5 MHZ has been reported [22]. Another advantage of SS-OCT is the broader bandwidth over SD-OCT, which is limited by the resolution of the spectrometer. As a result, SS-OCT is capable of providing a longer imaging range.

For ophthalmologic imaging, SD-OCT was introduced earlier than SS-OCT due to its lower cost, and to date SD-OCT has gained a dominant market share in clinical diagnostics [19]. However, with the advance of laser technology, SS-OCT starts to show advantages over SD-OCT in terms of sensitivity, imaging depth, and imaging speed.

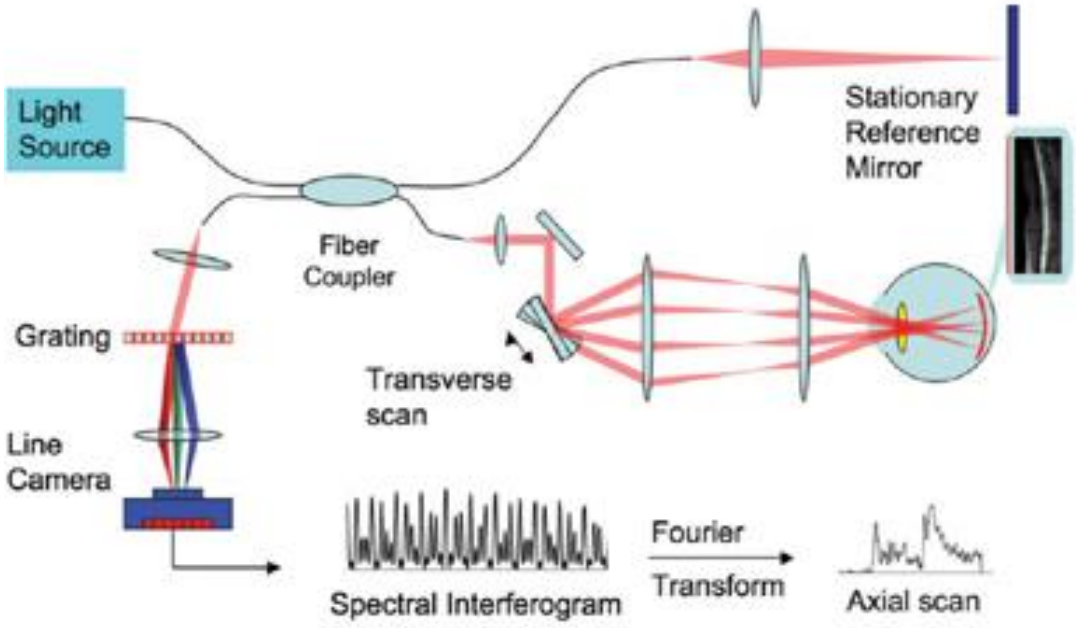

Figure 5: Schematic of a basic SD-OCT [21].

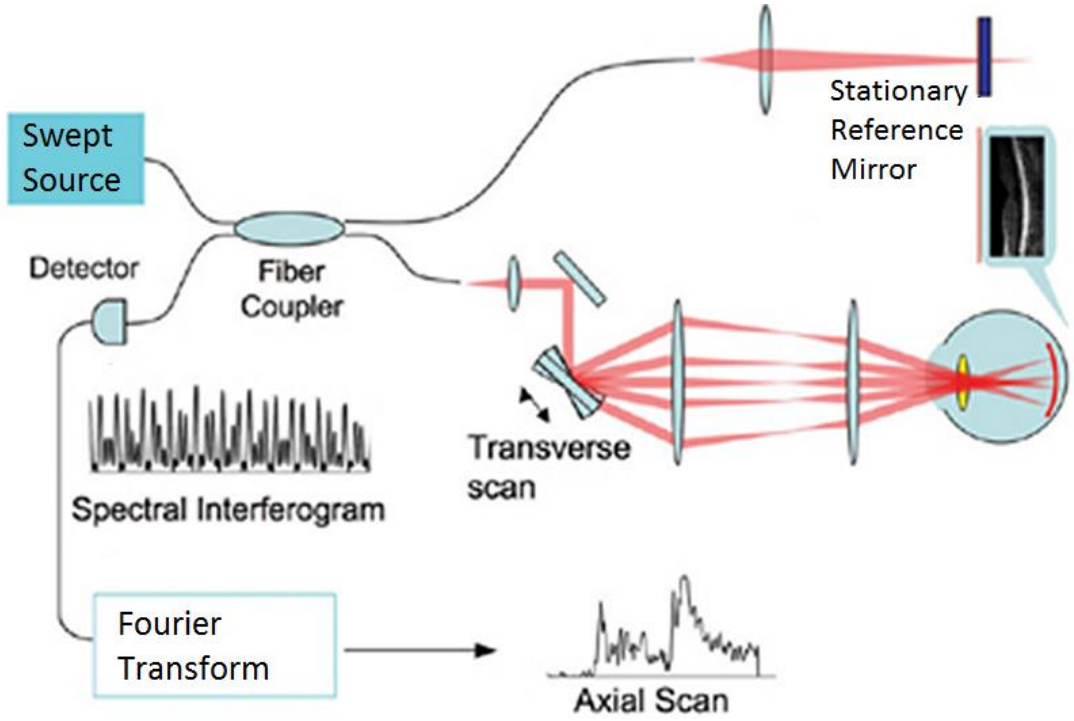

Figure 6: Schematic of a basic SS-OCT [21].

1.3.3. OCT for Ophthalmology

The most successful commercialized application of OCT in medical imaging is found in ophthalmology. OCT provides visualization of both anterior and posterior segment pathology with unrivaled resolution and depth penetration. Ophthalmologic OCT is used for diagnosis of various ocular diseases such as glaucoma, retinal detachment, retinal vascular occlusion, age-related macular degeneration, etc. Figure 7 shows an example of an OCT retinal image with ultrahigh resolution.

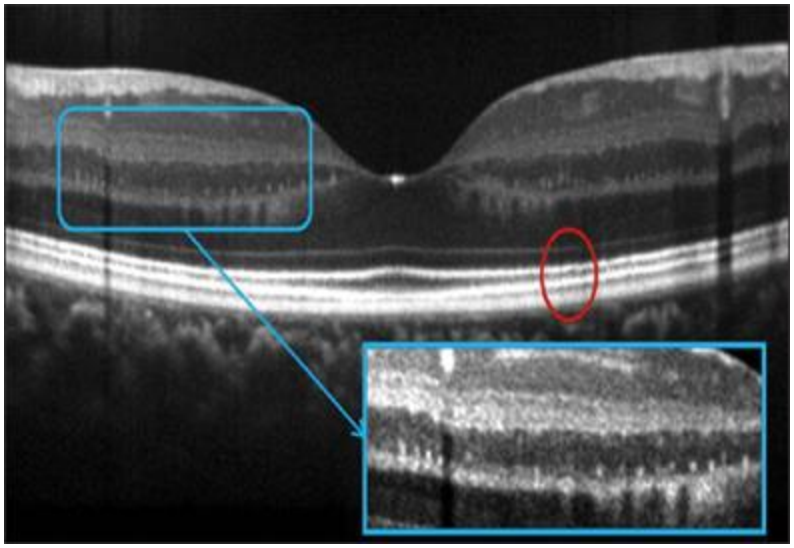

Figure 7: Normal foveal scan recorded with OCT with ultrahigh resolution (3 μm resolution) [21].

Light absorption by vitreous fluid, mostly water, determines wavelength selection for ophthalmic OCT. According to the absorption spectrum of water (Figure 8), most ophthalmic OCT systems use light sources centered at 830 nm spectral range where water absorption is minimal. However, at 830 nm light penetration into the retina is limited by high absorption and scattering by the retinal pigment epithelium (RPE) which prevents choroidal imaging. Recently, despite slightly decreased lateral resolution, OCT sources centered at 1060 nm wavelength are becoming more popular for retinal imaging for several reasons. First of all, maximum permissible exposure (MPE) at 1060 nm wavelength (3mW incident power on the cornea) is much higher than at 830 nm [23], so higher source power is allowed, providing improved signal-to-noise ratio (SNR) and better image quality. In addition, retinal scattering strength is lower at 1060 nm, so deeper choroidal penetration is possible with 1060 nm OCT systems.

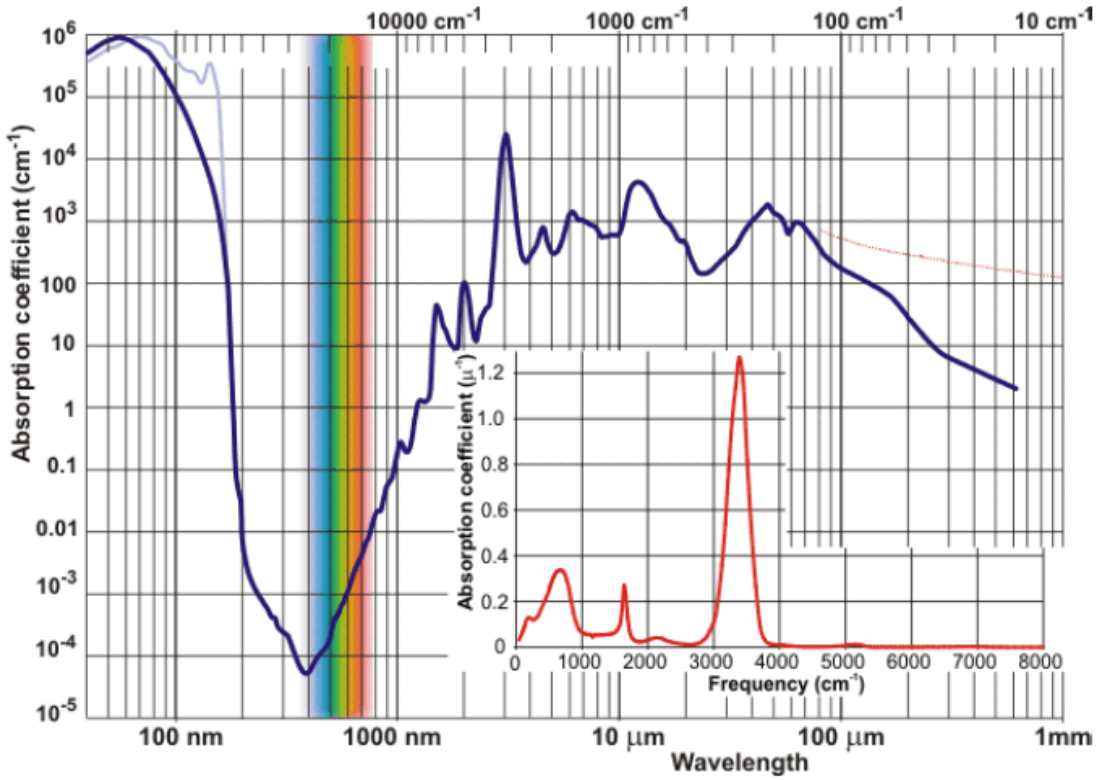

Figure 8: Water absorption spectrum.

From OCT retinal images, multiple retinal sublayers can be identified (Figure 7). Retinal sublayer segmentation, i.e. determining the boundaries of each sublayer, is the prerequisite of performing any further OCT image analysis or feature extraction, for example, calculating RNFL thickness and reflectance which are important glaucoma indicators. However, the segmentation of retinal sublayers is a challenging image processing problem because of the strong speckle noise presented in OCT retinal images. A possible solution to the retinal sublayer segmentation problem is proposed in Chapter 2.

Challenges in early glaucoma detection requires functional extension of traditional intensity OCT. Two functional OCT systems are discussed in this

dissertation: polarization-sensitive OCT (PS-OCT) and scattering-angle-diverse OCT (SAD-OCT).

PS-OCT is able to measure the birefringence of the sample. As mentioned previously, RGC axons located in RNFL are rich in microtubules, and microtubule density is expected to be a candidate indicator of retinal diseases like glaucoma. Because of the oriented cylindrical structure of RGC axons as well as the microtubules in RGC axons, RNFL is weakly birefringent [24], and its birefringence has been found to correlate with damage in glaucoma in previous clinical studies [25-27]. If PS-OCT instrumentation with sufficient polarimetric sensitivity is available, early detection of glaucoma may be possible by measuring RNFL birefringence, which is an indication of structural change in the cytoskeleton of RGC axons.

SAD-OCT is constructed to investigate the scattering properties of the sample. According to recent clinical and animal studies, the scattering properties of RNFL may change during RGC apoptosis, possibly due to the morphological changes in the mitochondrial networks in RGC axons [28, 29]. If a SAD-OCT is sufficiently sensitive, it may provide potentially valuable diagnostic information for certain retinal diseases by measuring the RNFL scattering properties.

Chapter 2: 3D Active Contour Segmentation for Retinal Sublayers from OCT Images

2.1. Introduction and Motivation

Optical coherence tomography (OCT) provides real time non-invasive cross-sectional images of tissue and is widely used in clinical ophthalmologic diagnosis. As visualized in OCT retinal images, the human retina consists of a series of stacked sublayers (Figure 9). Segmentation of retinal sublayers is a basic component in image analysis software required to analyze ophthalmologic OCT images.

Figure 9: Human retina consists of a series of stacked sublayers as visualized in OCT retinal images.

High speckle noise and the presence of artifacts in OCT images make segmentation of retinal sublayers difficult. As a result, most commercial OCT systems provide a semi-automatic program to segment one or two specific retinal sublayers, usually including the RNFL, or only provide interactive software to allow operators to manually select the boundaries of retinal sublayers. A fully automatic program which segments all retinal sublayers is not yet available on commercial OCT systems.

Various sophisticated RNFL segmentation approaches have been reported [30-35]. Mujat *et al*. used a deformable spline algorithm to determine RNFL thickness [30].

Garvin *et al*. presented a 3-D graph search approach for OCT retinal layer segmentation [31]. Paranjape *et al*. introduced a simple and fast segmentation method based on a Sobel filter for automated RNFL boundary detection [32]. Mishra *et al*. developed a two-step scheme which first identifies the approximate locations of the RNFL and then performs a local kernel-based optimization to refine segmentation results [33]. The algorithm was successfully applied on OCT scans of rodent eyes. Kajić *et al*. utilized texture and shape features of OCT images to detect RNFL boundary [34]. This approach was proven to be insensitive to noise in OCT human retinal images. Mayer *et al*. designed a segmentation approach based on the minimization of an active contour energy function consisting of gradient and local smoothing terms, and evaluated the algorithm on both normal and glaucoma eyes [35]. Among all reported studies, active contour is a particularly promising approach for its robustness to noise and capability to incorporate prior knowledge of the structural shape. Application of active contour algorithm for retinal sublayer segmentation in OCT images has been demonstrated by Fernández *et al*. [36], Mishra *et al*. [33], and Yazdanpanah *et al.* [37].

However, all the cited work was performed on two-dimensional OCT images. Since the structure of retinal sublayers is physiologically continuous and smooth in all directions, the boundaries of retinal sublayers are expected to be consistent across B-scans. The across-B-scan consistency of retinal sublayer boundaries in previous approaches is inherently neglected because they are based on isolated B-scan image analysis. In addition, due to the lack of a reasonably good initial estimate of sublayer boundary locations, some of the cited work requires user input to initialize the segmentation algorithm and these approaches are not suitable for real-time clinical use. Another challenge with the application of active contour approaches is the relatively high computational requirements which have resulted in slow processing speeds.

In this chapter, a fully automatic three-dimensional (3D) multiphase active contours segmentation algorithm implemented with GPU assisted computation is presented [38]. This is the first report that demonstrates the application of a 3D active contour algorithm operating on OCT retinal image stacks with GPU implementation to improve computational speed by orders of magnitude over CPU implementation.

2.2. ACTIVE CONTOUR MODEL

The active contour model, sometimes also called "snakes," is a framework for segmenting an object from a noisy 2D or 3D image. The basic idea of an active contour model is to define a contour from an initial estimate, for instance, a contour around the object to be segmented, and evolve the contour towards the boundary of the object, so that the contour eventually coincides with the boundary of an object in the image. Some important basic concepts in an active contour model include:

Image: A 2D or 3D matrix of values, usually 8-bit numbers ranging from 0 to 255. Each element in an image is called pixel for 2D images and voxel for 3D images.

Contour (sometimes called curve): For 2D images, a contour is a piece of a 1D curve. For 3D images, a contour is a 2D surface. As discussed later in Section 2.3.1, for an N-dimensional image, a contour is a N-1 dimensional surface, and can be represented with the level set of a N-dimensional function.

Boundary (sometimes called edge): A set of connected pixels or voxels on an 2D or 3D image, representing the physical boundary of a certain object. Usually, the pixel or voxel values inside and outside the boundary are different, and the pixel or voxel value difference enables human observers to distinguish an object.

Energy function: A function associated with a contour. The energy function evaluates how "good" a contour is, compared with the actual boundary of the object in

the image. The energy function is designed so that its value is minimized when the contour coincides with the boundary. The energy function is the key element in designing an effective active contour model.

In order to evolve a contour towards the boundary of an object in an image, the evolution of the contour is guided by the energy function. Under the influence of the energy function, the boundary curve evolves with successive iterations and finally terminates at a location with minimum energy.

2.3. FRAMEWORK

2.3.1. Level Set Representation of a Contour

How to describe a contour? The natural approach is to provide a set of key coordinates that are located on the contour, so that the contour is described by connecting the key coordinates. Another way to describe a contour is to use the level set method [39]. Mathematically, describing a contour using the level set method has certain advantages which are discussed below. The basic idea of the level set method is briefly reviewed here.

The level set of a function ϕ is a set of coordinates on which the function has a specified constant value. The function ϕ is called level set function. If the specified constant value is zero, the level set is called zero level set. If the level set function is two-dimensional $\phi(x, y)$, the zero level set of ϕ is a closed contour C by

$$\mathrm{C} = \left\{(\mathrm{x}, \mathrm{y}) \mid \phi\left(x, y\right) = 0\right\} \tag{1}$$

Figure 10 shows an example of the level set representation of a contour in 2D.

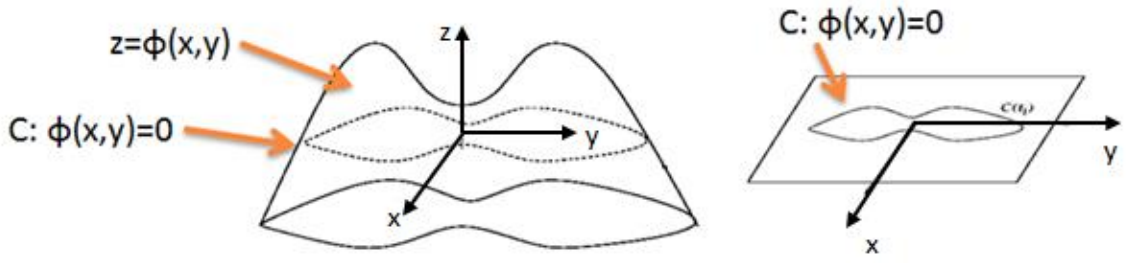

Figure 10: An example of level set representation of a contour in 2D circumstance. Left: the level set function with a zero level set. Right: The corresponding contour is determined by the zero level set.

An important concept associated with the level set representation of a contour is the signed distance function (SDF). A level set function ϕ is called a signed distance function (SDF) if ϕ has a unity gradient magnitude at all (x, y) coordinates [40]. For example, in 2D case, $\phi(x, y)$ is an SDF if

$$|\nabla\phi| = 1 \text{ for all } (x, y) \tag{2}$$

Because of the unity gradient property, SDF gives the shortest distance from any coordinate to the zero level set. In practice, the SDF is constructed from a given contour. Given any contour C, a SDF $\phi(x, y)$ is constructed by assigning negative values to the region inside of C, positive values to the region outside of C, and values of zero along the contour C itself [41]. Of course, the construction needs to satisfy the unity gradient requirement in (2). As a result, it is possible to define the coordinate region inside and outside of a contour C:

$$\begin{aligned} C &= \{(x, y) \mid \phi(x, y) = 0\} \\ in(C) &= \{(x, y) \mid \phi(x, y) > 0\} \\ out(C) &= \{(x, y) \mid \phi(x, y) < 0\} \end{aligned} \tag{3}$$

Define a Heaviside step function:

$$H(\phi)=\begin{cases}0 & if \quad \phi<0\\ 0.5 & if \quad \phi=0\\ 1 & if \quad \phi>0\end{cases} \tag{4}$$

So that

$$H\left(\phi(x,y)\right)=\begin{cases}0 & if\ (x,y)\ is\ outside\ C\\ 0.5 & if\ (x,y)\ is\ on\ C\\ 1 & if\ (x,y)\ is\ inside\ C\end{cases} \tag{5}$$

Also define a Dirac function:

$$\delta(\phi)=\begin{cases}1 & if \quad \phi=0\\ 0 & otherwise\end{cases} \tag{6}$$

So that

$$\delta\left(\phi(x,y)\right)=\begin{cases}1 & if\ (x,y)\ is\ on\ C\\ 0 & otherwise\end{cases} \tag{7}$$

As to be shown in Section 2.5, (5) and (7) are frequently used as region selector functions which select the coordinate region inside, outside or on a contour.

Similarly, the above properties of level set can be extended to 3D case. In 3D case, $\phi(x,y,z)$ is an SDF if

$$\left|\nabla\phi\right|=1 \text{ for all } (x,y,z) \tag{8}$$

The contour C associated with $\phi(x,y,z)$, and the coordinate region inside and outside of C are defined as:

$$\begin{aligned}&C=\{(x,y,z)\,|\,\phi(x,y,z)=0\}\\ &in(C)=\{(x,y,z)\,|\,\phi(x,y,z)>0\}\\ &out(C)=\{(x,y,z)\,|\,\phi(x,y,z)<0\}\end{aligned} \tag{9}$$

And the region selector functions:

$$H\left(\phi(x,y,z)\right)=\begin{cases}0 & if\ (x,y,z)\ is\ outside\ C\\ 0.5 & if\ (x,y,z)\ is\ on\ C\\ 1 & if\ (x,y,z)\ is\ inside\ C\end{cases} \tag{10}$$

$$\delta\left(\phi(x,y,z)\right)=\begin{cases}1 & if\ \left(x,y,z\right)is\ on\ C\\ 0 & otherwise\end{cases} \tag{11}$$

The level set description of a contour has several advantages over the direct approach using key coordinates. A contour defined by the zero level set of a continuous SDF ensures the contour is always continuous and closed [39]. Also, the level set method provides an easy way of describing the inside and outside regions of the contour with a Heaviside step function. This allows for simple selection of all the points outside or inside the contour for further processing. In addition, the shape, even topology of a contour can be conveniently deformed by modifying the SDF associated with the contour, making contour evolution possible (Figure 11).

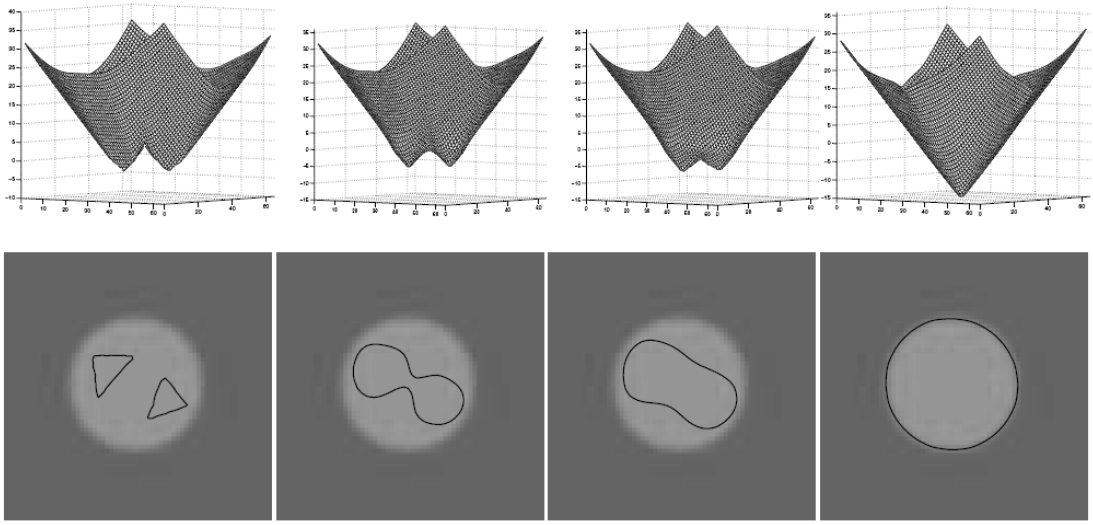

Figure 11: An example of contour evolution using the level set method [42]. The top plots depict the SDF $\phi(x,y)$ while the bottom images show the contour described as the zero level set of $\phi(x,y)$ overlaid on the segmentation target image.

2.3.2. Structural Assumption for Retinal Sublayers

For an OCT image volume acquired by either a raster scan or ring scan, the image volume is 3D matrix $I(x,y,z)$. Since the human retina is a layered structure consisting

of a number of retinal sublayers, the boundaries between retinal sublayers are considered as 2D surfaces floating in the 3D OCT image stack $I(x, y, z)$.

A total of eight boundaries between sublayers are recognized in a 3D retinal OCT image stack, dividing the image stack into nine layered regions: (1) vitreous, (2) retinal nerve fiber layer (RNFL), (3) inner plexiform layer (IPL), (4) inner nuclear layer (INL), (5) outer plexiform/nuclear layer (OPL/ONL), (6) inner/outer segment photoreceptor layer (IS/OS), (7) retinal pigment epithelium (RPE), (8) choroid, and (9) the sub-choroidal space. The *i*-th boundary is defined by a 2D boundary function $z = C_i(x, y)$, *i*=1, 2,…, 8. The sublayer segmentation problem is mathematically equivalent to finding a set of C_i that best segments the 3D image stack.

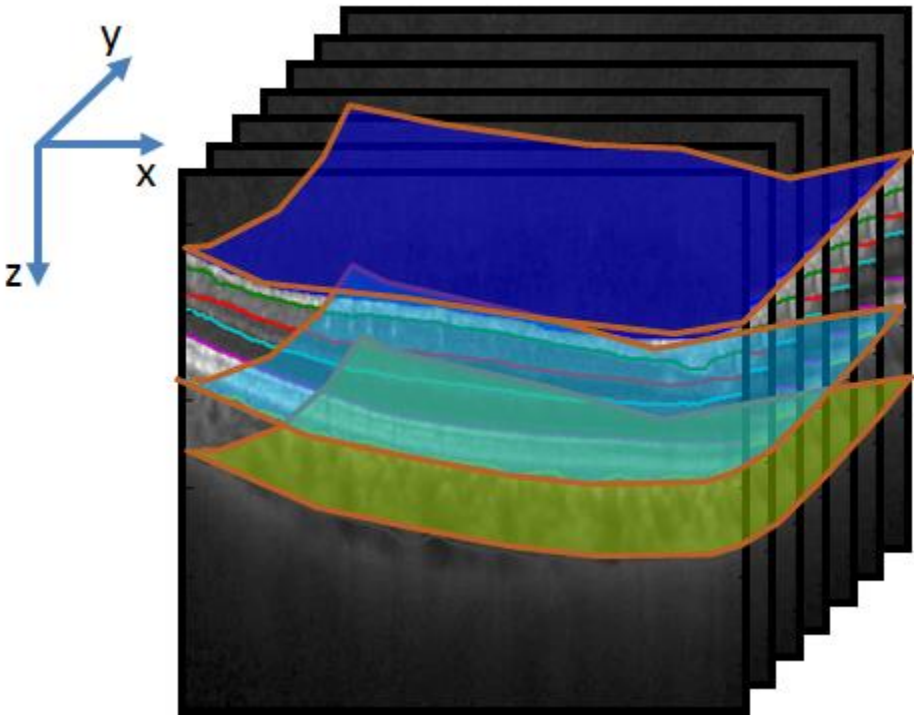

Figure 12: An example OCT image stack of the retina, visualized with three boundaries overlaid on the 3D image. The boundaries between retinal sublayers are considered as 2D surfaces floating in the 3D OCT image stack

Each contour C_i is uniquely associated with a signed distance function (SDF) $\phi_i(x, y, z)$, with the fact that C_i is the zero level set of $\phi_i(x, y, z)$. The contour C_i is deformed through the evolution of its corresponding SDF $\phi_i(x, y, z)$.

2.4. INITIAL ESTIMATES OF BOUNDARY LOCATIONS

The initial locations of each boundary C_i are automatically estimated in a preprocessing step. To mitigate the effect of speckle, the 3D image stack is downsampled and blurred with a 3D Gaussian filter. Rough RNFL and RPE initial locations are determined by selecting the two brightest layers in the blurred image stack. Initial estimates of the other six boundaries are interpolated between the RNFL and RPE, making up a total of eight boundaries.

2.5. ENERGY FUNCTIONS

Evolution of the initial contour C_i is guided by an energy function $E(C_i)$. For the contour C_i associated with an SDF $\phi_i(x, y, z)$, the energy function is expressed as:

$$\begin{aligned} E(C_i) &= E(\phi_i(x, y, z)) \\ &= w_{\text{Image}} E_{\text{Image}}(\phi_i) + w_{\text{Shape}} E_{\text{Shape}}(\phi_i) + w_{\text{Regularization}} E_{\text{Regularization}}(\phi_i) + w_{\text{SDF}} E_{\text{SDF}}(\phi_i) \end{aligned} \tag{12}$$

where w_{Image}, w_{Shape}, $w_{\text{Regularization}}$, and w_{SDF} are real-valued positive constant weighting factors. The image term E_{Image} attracts the contour towards the object boundary. The shape term E_{Shape} attracts the contour to move towards an "expected boundary location" $B_i(x, y, z, t)$, which is dynamically calculated during the evolution of contours. The regularization term $E_{\text{Regularization}}$ encourages creation of a minimal area and smooth boundary. The SDF term E_{SDF} keeps $\phi_i(x, y, z)$ to be an SDF with unity gradient. The image term E_{Image} and regularization term $E_{\text{Regularization}}$ here are similar but with slight modifications based on the work of Chan [43] and Yazdanpanah [37]. The SDF term

E_{SDF} was proposed by Li [42]. The shape term E_{Shape} is novel and originally introduced here. All energy terms are expressed in level set form and described in detail below:

2.5.1. Image Term

Image term $E_{\text{Image}}(\phi_i)$ is minimized, when the *i*-th contour C_i which is also the zero level set of ϕ_i coincides with a retinal sublayer boundary. The image term is designed to be region-based following the work of Chan and Vese [43]. The region-based image term encourages each region of segmentation (i.e. the region between $C_{i-1}:\phi_{i-1}(x,y,z)=0$ and $C_i:\phi_i(x,y,z)=0$ for *i*=2, 3, …, 8) to have an approximately constant intensity. The intensity of the *i*-th segmentation region is approximated by a constant M_i, which is the mean intensity of the image subset formed between $C_{i-1}:\phi_{i-1}(x,y,z)=0$ and $C_i:\phi_i(x,y,z)=0$:

$$M_i = \frac{\iiint I(x,y,z)H\left(\phi_{i-1}(x,y,z)\right)\left(1-H\left(\phi_i(x,y,z)\right)\right)dxdydz}{\iiint H\left(\phi_{i-1}(x,y,z)\right)\left(1-H\left(\phi_i(x,y,z)\right)\right)dxdydz} \tag{13}$$

In the above equation, the term $H\left(\phi_{i-1}(x,y,z)\right)\left(1-H\left(\phi_i(x,y,z)\right)\right)$ functions as a region selector function for the region between the (*i*-1)-th contour C_{i-1} and the *i*-th contour C_i for the following reason. $H\left(\phi_{i-1}(x,y,z)\right)$ is evaluated to be 1 outside (i.e. below) C_{i-1} and 0 inside (i.e. above) C_{i-1}, while $\left(1-H\left(\phi_i(x,y,z)\right)\right)$ is evaluated to be 0 outside (i.e. below) C_i and 1 inside (i.e. above) C_i. So the product of $H\left(\phi_{i-1}(x,y,z)\right)$ and $\left(1-H\left(\phi_i(x,y,z)\right)\right)$ provides a binary mask which returns 1 for (x,y,z) located between $C_{i-1}:\phi_{i-1}(x,y,z)=0$ and $C_i:\phi_i(x,y,z)=0$, and 0 for (x,y,z) located in anywhere else.

The mathematical form of the image term is:

$$E_{\text{Image}}(\phi_i(x,y,z)) = \lambda_1 \iiint \left(I(x,y,z) - M_i\right)^2 H\left(\phi_{i-1}(x,y,z)\right)\left(1 - H\left(\phi_i(x,y,z)\right)\right) dxdydz + \lambda_2 \iiint \left(I(x,y,z) - M_{i+1}\right)^2 H\left(\phi_i(x,y,z)\right)\left(1 - H\left(\phi_{i+1}(x,y,z)\right)\right) dxdydz \quad (14)$$

Similar as the previous discussion, the term $H\left(\phi_i(x,y,z)\right)\left(1 - H\left(\phi_{i+1}(x,y,z)\right)\right)$ functions as a region selector for the region between the *i*-th contour C_i and the (*i*+1)-th contour C_{i+1}.

The assumption behind the image term $E_{\text{Image}}(\phi_i)$ is that the intensity within each retinal sublayer is approximately constant at M_i, i.e. the OCT image is piecewise constant. If the assumption holds, then $E_{\text{Image}}(\phi_i)$ is minimized when each contour $C_i : \phi_i(x,y,z) = 0$ matches to the corresponding sublayer boundary.

Figure 13 shows an example of the effect of contour evolution using only the image term and SDF term. Under the influence of the image term, the contours correctly move toward image boundaries, but are not smooth or regularly shaped due to the lack of shape and regularization terms. Note that the mathematical details about contour evolution will be discussed in Section 2.5.5. Also, SDF term is included in Figure 13 because the SDF term is required for the active contour model to behave correctly, which will be discussed in detail in Section 2.5.4.

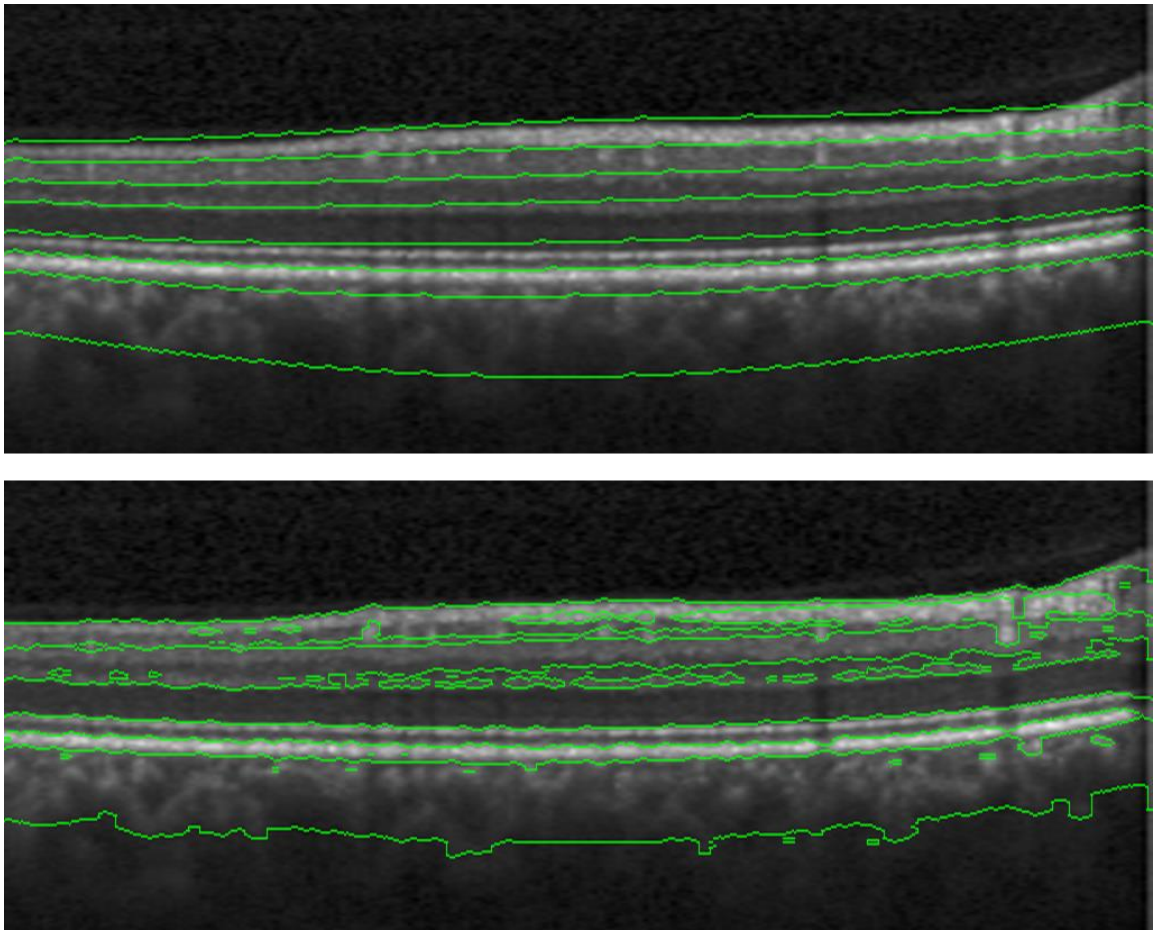

Figure 13: An example of the initial contour (top) and evolution using only the image term and SDF term (bottom) on a human retinal image. The contours move toward image boundaries but are not smooth or regularly shaped.

2.5.2. Shape Term

The assumption behind the image term $E_{\text{Image}}(\phi_i)$ that the OCT image is piecewise constant may not be always true. There may be intensity inhomogeneity within a retinal sublayer due to shadow artifacts introduced by retinal blood vessels which strongly absorb and scatter light. Another possible problem with the image term $E_{\text{Image}}(\phi_i)$ is that when the noise level is high, there may not be enough image information to correctly deform the contour. Based on prior knowledge of retinal

anatomy, a shape term is introduced to attract the contour towards an expected boundary location. The shape term is mathematically expressed as:

$$E_{\text{Shape}}(\phi_i(x,y,z)) = \iiint \left(z - B_i(x,y)\right)^2 \delta(\phi_i(x,y,z)) \,|\nabla \phi_i(x,y,z)|\, dxdydz \qquad (15)$$

where $B_i(x,y)$ is the expected boundary location for the *i*-th boundary, which is determined by the weighted sum of $C_{i-1}(x,y)$ and $C_{i+1}(x,y)$:

$$B_i(x,y) = \frac{\iint \left(C_{i+1} - C_i\right) dxdy}{\iint \left(C_{i+1} - C_{i-1}\right) dxdy} C_{i-1}(x,y) + \frac{\iint \left(C_i - C_{i-1}\right) dxdy}{\iint \left(C_{i+1} - C_{i-1}\right) dxdy} C_{i+1}(x,y) \qquad (16)$$

Based on the prior knowledge that retinal sublayers are generally parallel to each other, B_i is usually a good estimate of the expected boundary location because it uses the information of the (*i*-1)-th contour $C_{i-1}(x,y)$ and the (i+1)-th contour $C_{i+1}(x,y)$.

δ in (15) is Dirac function. $\delta(\phi_i(x,y,z))$ functions as an contour selector. $\delta(\phi_i(x,y,z))$ is evaluated to be 1 only when $\phi_i(x,y,z) = 0$, i.e. (x,y,z) is located on the zero level set of ϕ_i, in other word, when (x,y,z) is located on C_i.

The shape term $E_{\text{Shape}}(\phi_i)$ is minimized when each contour $C_i : \phi_i(x,y,z) = 0$ is close to its corresponding expected boundary location B_i. Since B_i is calculated based on the weighted sum of C_{i-1} and C_{i+1}, the final effect is to make the retinal sublayers generally parallel to each other. Figure 14 shows an example of the effect of contour evolution using only the shape term and SDF term. Under the influence of the shape term, the contours become parallel to each other as expected. Since the image term is not included in the result presented in Figure 14, image information is never used, so the contours do not move towards image boundary. Obviously, the shape term must work together with image term in order to utilize the image information.

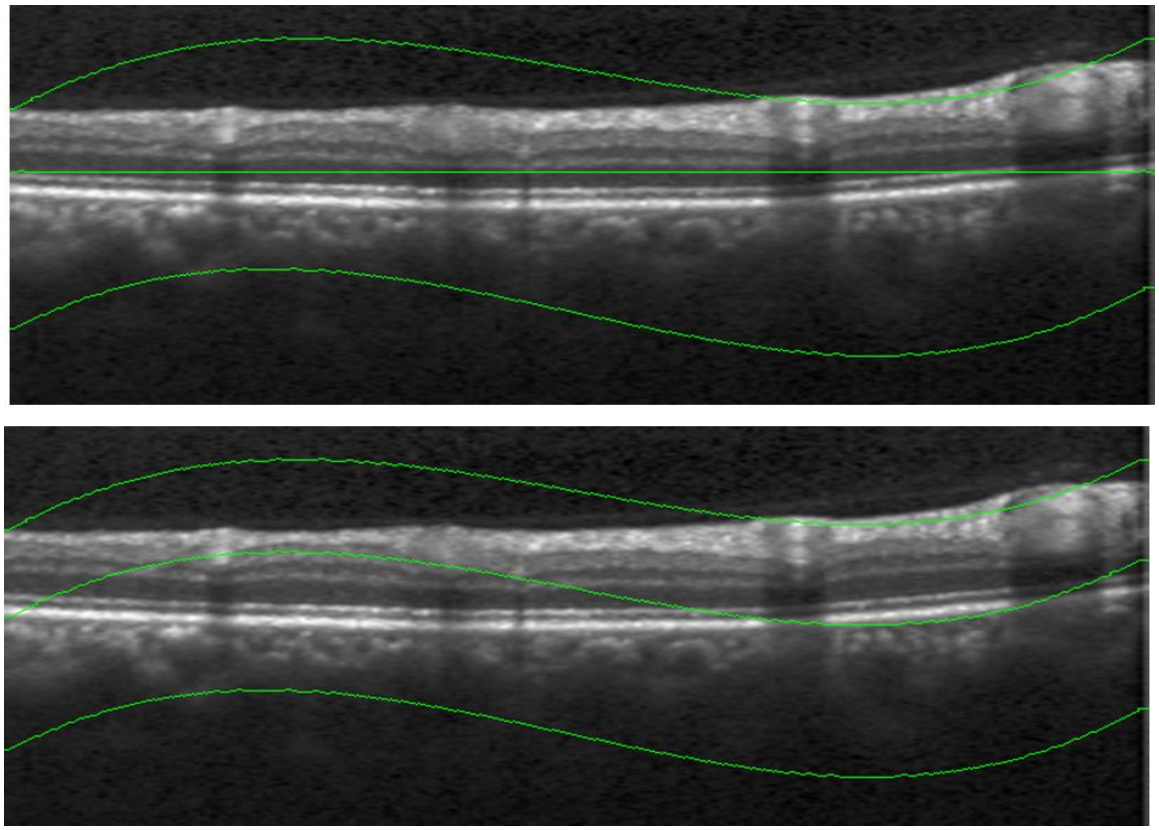

Figure 14: An example of three contours with a bad initialization (top) and upon convergence (bottom) on a human retinal image. The second contour evolves with only the shape term and SDF term. The shape term encourages retinal sublayers to be generally parallel to each other. Since image term is not included here, using just the shape term does not correctly identify the boundaries of the retinal layers.

2.5.3. Regularization Term

Regularization term is introduced to maintain the boundaries of the segmented retinal sublayer smooth. Smooth boundaries are encouraged by adding a contour length term [37, 43].

$$E_{\text{Regularization}}(\phi_i(x,y,z)) = \iiint \delta(\phi_i(x,y,z)) \,|\, \nabla\phi_i(x,y,z) \,|\, dxdydz \tag{17}$$

Figure 15 shows an example of the effect of contour evolution using only the regularization term and SDF term. The initial contours are added with noise in order to

demonstrate the effect of the regularization term. Under the influence of the regularization term, the contours become smooth. Since image information is not used in this example, the contours do not move towards image boundary.

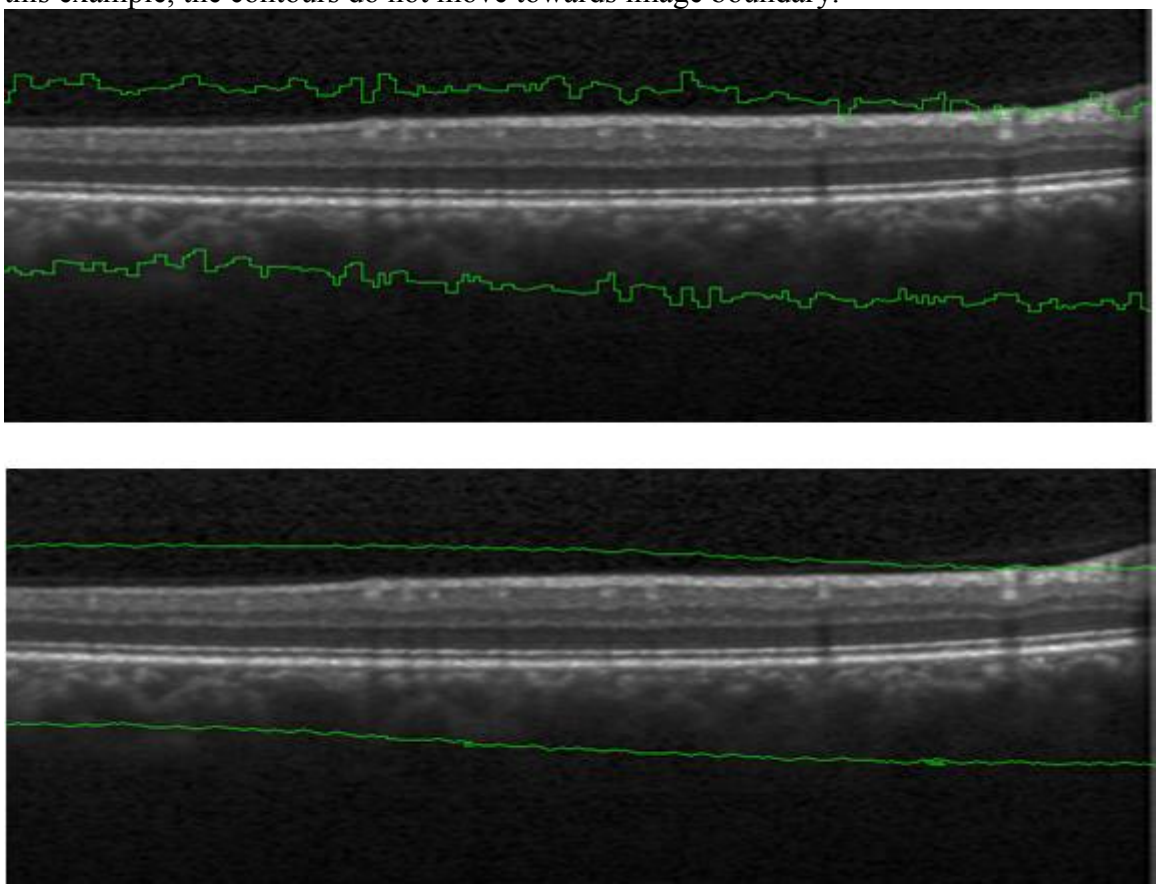

Figure 15: An example of two contours with a noisy initialization (top) and upon convergence (bottom) on a human retinal image. Both contours evolve with only the regularization term and SDF term. The regularization term keeps the contours smooth. Since image term is not included here, using just the regularization term does not correctly identify the boundaries of the retinal layers.

2.5.4. SDF Term

The shapes of the contours C_i are deformed by modifying their corresponding SDFs ϕ_i. However, after several iterations of modifying ϕ_i, as a consequence, the gradient of ϕ_i may no longer have a unity magnitude throughout the whole image. If

more iterations are allowed to proceed, ϕ_i no longer fulfills the SDF criteria which requires a unity gradient magnitude. Since unity gradient of ϕ_i is a necessary prerequisite to ensure the active contour model's correct behavior, the SDF term is introduced in the energy function to maintain ϕ_i close to a valid SDF [42].

$$E_{\text{SDF}}(\phi_i(x,y,z)) = \iiint \frac{1}{2}\left(|\nabla\phi_i(x,y,z)| - 1\right)^2 dxdydz \tag{18}$$

2.5.5. Minimization of Energy Function

Based on the combination of the above energy terms, $\phi_C(x,y)$ the total energy $E(C_i)$ or $E(\phi_i(x,y,z))$ is minimized through the evolution of $\phi_i(x,y,z)$. In order to perform the evolution, an artificial time-step parameter *t* is introduced so that ϕ_i becomes $\phi_i(x,y,z,t)$. The evolution equation is conducted by applying the Euler-Lagrange Equation:

$$\begin{aligned}\frac{\partial\phi_i(x,y,z,t)}{\partial t} &= -\frac{\partial E(\phi_i(x,y,z,t))}{\partial\phi_i} \\ &+ \frac{d}{dx}\left(\frac{\partial E(\phi_i(x,y,z,t))}{\partial\phi_{ix}}\right) + \frac{d}{dy}\left(\frac{\partial E(\phi_i(x,y,z,t))}{\partial\phi_{iy}}\right) + \frac{d}{dz}\left(\frac{\partial E(\phi_i(x,y,z,t))}{\partial\phi_{iz}}\right)\end{aligned} \tag{19}$$

After simplification, the evolution equation (15) is reduced to:

$$\begin{aligned}\frac{\partial\phi_i(x,y,z,t)}{\partial t} &= w_{\text{Image}}\delta(\phi_i)\iiint\left[\lambda_1\left(I(x,y,z)-M_i\right)^2 - \lambda_2\left(I(x,y,z)-M_{i+1}\right)^2\right]dxdydz \\ &+ w_{\text{Shape}}\delta(\phi_i)\left[2\left(z-B_i(x,y)\right)\frac{-B_{ix}(x,y)\phi_{ix} - B_{iy}(x,y)\phi_{iy} + \phi_{iz}}{|\nabla\phi_i|} + \left(z-B_i(x,y)\right)^2\kappa(\phi_i)\right] \\ &+ w_{\text{Regularization}}\delta(\phi_i)\kappa(\phi_i) + w_{\text{SDF}}\left[\Delta\phi_i - \kappa(\phi_i)\right]\end{aligned} \tag{20}$$

where $\kappa(\phi_i)$ is the curvature operator:

$$\kappa(\phi_i) \equiv div\left(\frac{\nabla\phi_i}{|\nabla\phi_i|}\right)$$
$$= \frac{\phi_{ix}{}^2\left(\phi_{iyy}+\phi_{izz}\right)+\phi_{iy}{}^2\left(\phi_{ixx}+\phi_{izz}\right)+\phi_{iz}{}^2\left(\phi_{ixx}+\phi_{iyy}\right)-2\phi_{ixy}\phi_{ix}\phi_{iy}-2\phi_{ixz}\phi_{ix}\phi_{iz}-2\phi_{iyz}\phi_{iy}\phi_{iz}}{(\phi_{ix}{}^2+\phi_{iy}{}^2+\phi_{iz}{}^2)^{3/2}} \quad (21)$$

After calculating $\partial\phi_i/\partial t$ from (14), the evolution of $\phi_i(x,y,z,t)$ is implemented by:

$$\phi_i(x,y,z,t+dt) = \phi_i(x,y,z,t) + \frac{\partial\phi_i(x,y,z,t)}{\partial t}\cdot dt \quad (22)$$

where *dt* is an artificial time step size.

The contour evolution equation (16) is expressed in continuous form. However, in actual numerical implementation, the evolution is computed with discrete approximation.

2.5.6. Adaptive Weighting Factors

The performance of the 3D active contour algorithm is greatly affected by the value selections of the weighting factors w_{Image}, w_{Shape}, $w_{\text{Regularization}}$, and w_{SDF}. How to choose the best combination of weighting factors is an open problem and is often treated empirically. Here, following the work of Yazdanpanah [37], the idea of adaptive weighting factor is introduced. The weighting factors change with iteration number, as shown in Figure 16. Intuitively, in early iterations, the influence from the image term w_{Image} should be larger so that the contours quickly evolve towards the boundary of each sublayer and the coarse structure of the sublayer is found. Later as the iteration number progresses, the shape term w_{Shape} and the regularization term $w_{\text{Regularization}}$ should become more important to refine the contour and assist the algorithm when image information is insufficient to segment the image. Since the SDF term is a necessary component to ensure the behavior of contour evolution, w_{SDF} is kept constant throughout the iteration.

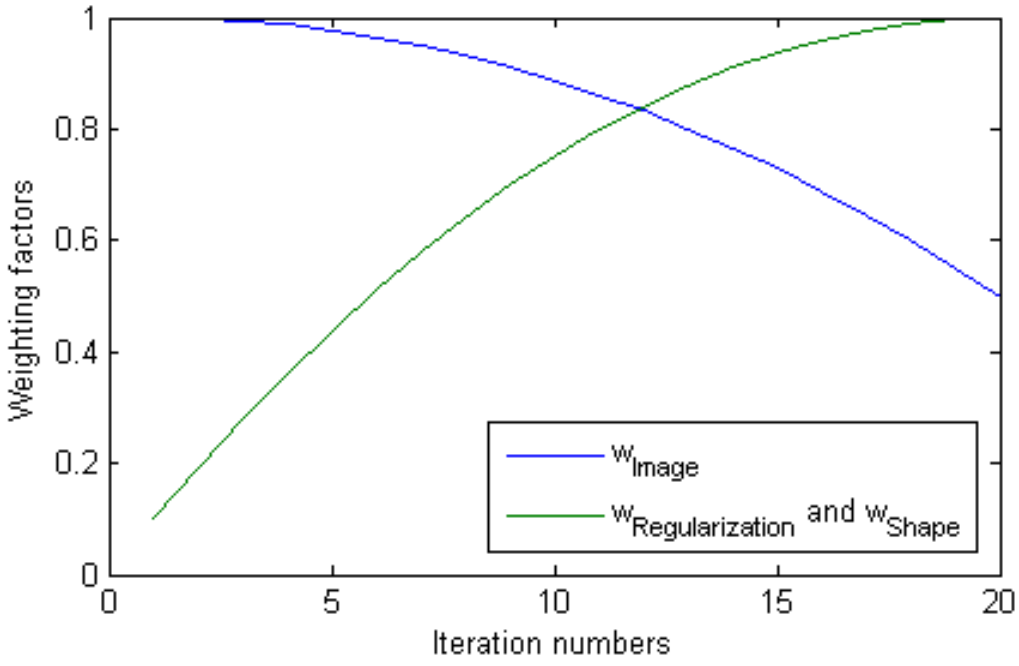

Figure 16: The weighting factors change with iteration number. In early iterations, the influence from the image term w_{Image} should be larger so that the contours quickly evolve towards the boundary of each sublayer and the coarse structure of the sublayer is found. Later as the iteration number progresses, the shape term w_{Shape} and the regularization term $w_{\text{Regularization}}$ should become more important to refine the contour and assist the algorithm when image information is insufficient to segment the image.

2.5.6. Implementation on a CPU-GPU Hybrid Computing Architecture

The contour evolution process is time consuming when segmenting a 3D image, because the contour evolution in (21) includes a curvature calculation on a 3D image. The curvature calculation is a computationally demanding operation in 3D. The curvature computation requires gradient and Laplacian operation on a 3D matrix as well as 3D matrix arithmetic operations. However, all these operations can be significantly accelerated with a graphics processing unit (GPU) implementation. To improve

computational speed, OpenCL is introduced to implement the curvature calculation on the GPU, while other steps are currently implemented on the CPU using MATLAB.

2.6. SEGMENTATION RESULTS

Retinal OCT imaging was performed on a healthy subject using a commercial ophthalmologic OCT instrument (Spectralis Spectral Domain OCT, Heidelberg Engineering). A set of 3D OCT image volume (1024×100×496 voxels) were acquired near the fovea. For faster processing speed, the image volume was downsampled to 205×100×496 before the segmentation.

The segmentation algorithm was successfully applied on the image stack. Figure 17 only shows the 3D segmentation results on a certain B-scan cross-section, while the algorithm actually detects the retinal sublayer boundaries on all the 496 B-scans.

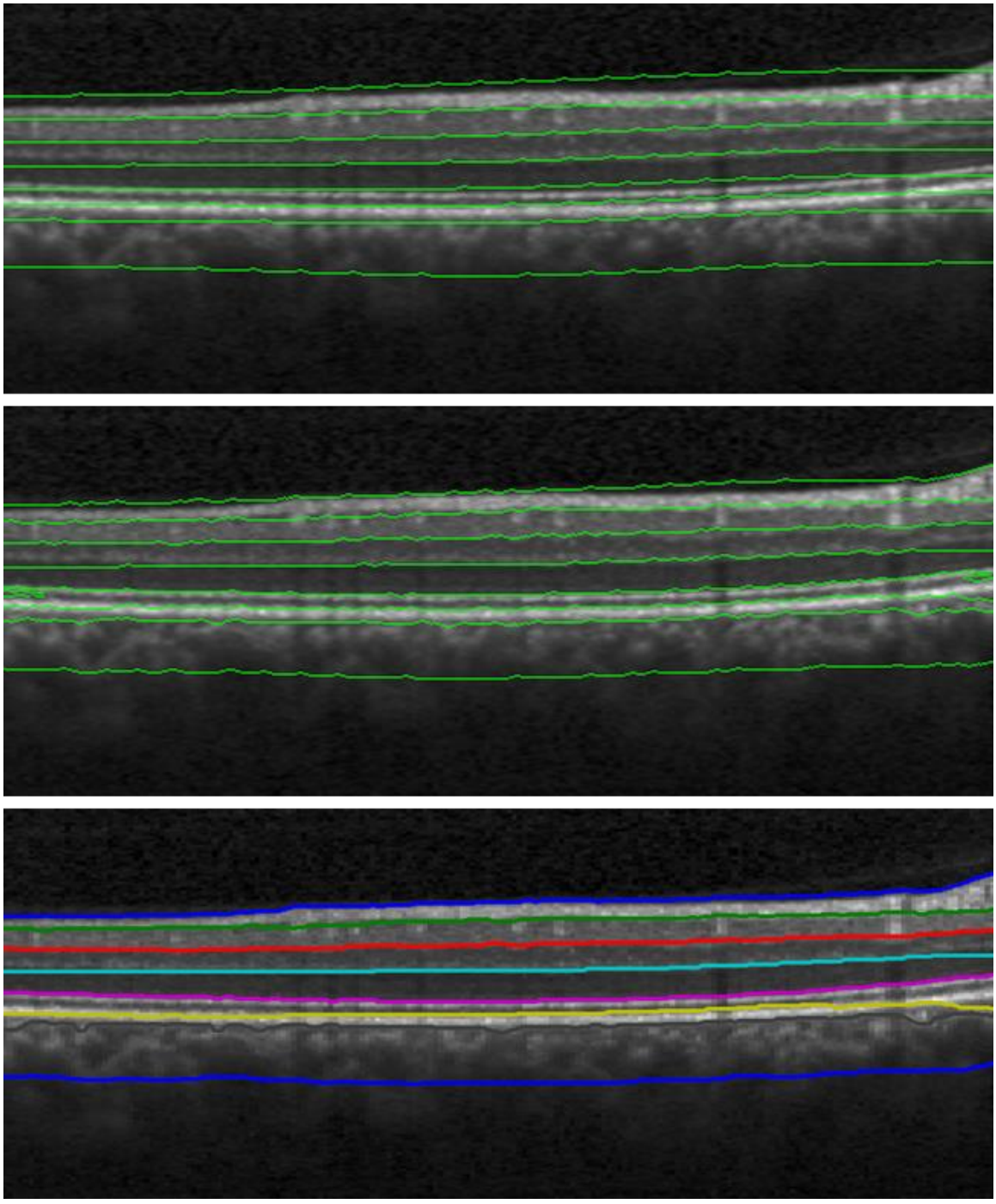

Figure 17: 3D active contour segmentation results on a B-scan cross-section. Top: The initial estimates of the 8 sublayer boundaries. Middle: Segmentation results after 2 evolution iterations. Bottom: Final segmentation results after 10 evolution iterations.

2.6.1. Accuracy Test

To study the accuracy of the 3D active contour segmentation algorithm, the segmentation results were compared with ground truth of retinal sublayer boundaries which are manually selected by an OCT expert [38]. According to the comparison, averaged error rate of the segmentation (misdetection tolerance is set to be 2 pixels) is below 5% for all retinal sublayers (Table 1). In other words, more than 95% of the retinal sublayer boundaries are correctly determined.

However, the error rates of segmentation listed in Table 1 were determined based on a small sample size (only 3 frames were manually inspected). In addition, the initial estimates of the boundary location were manually selected and fairly close to the actual retinal sublayer boundaries. Thus the error rates in Table 1 may be underestimated and a more thorough test is required to evaluate the accuracy of the algorithm.

Layer	Error Rate (%)	Standard Deviation (%)
NFL	2.42	0.97
GCL	4.14	1.49
INL	3.44	1.40
OPL	4.18	1.66
ONL	3.71	0.85
IS	1.60	1.07
OS	3.13	1.48
RPE	2.46	0.92
Average	3.14	1.23

Table 1: Mean and standard deviation of segmentation error rate for each retinal sublayer, calculated from 3 frames of an OCT image volume.

2.6.2. 3D Active Contour Model vs. 2D Active Contour Model

The proposed 3D active contour segmentation algorithm is inherently more noise resistant than 2D active contour methods. To demonstrate this, the OCT images were

added with random noise for a noise tolerance test. The whole 3D image stack was processed with the proposed 3D active contour algorithm, while a 2D frame from the stack was processed with a 2D version of the active contour algorithm. The 2D algorithm failed to detect some boundaries corrupted with high speckle noise, while the proposed 3D algorithm successfully detected all boundaries at the same noise level (Figure 18).

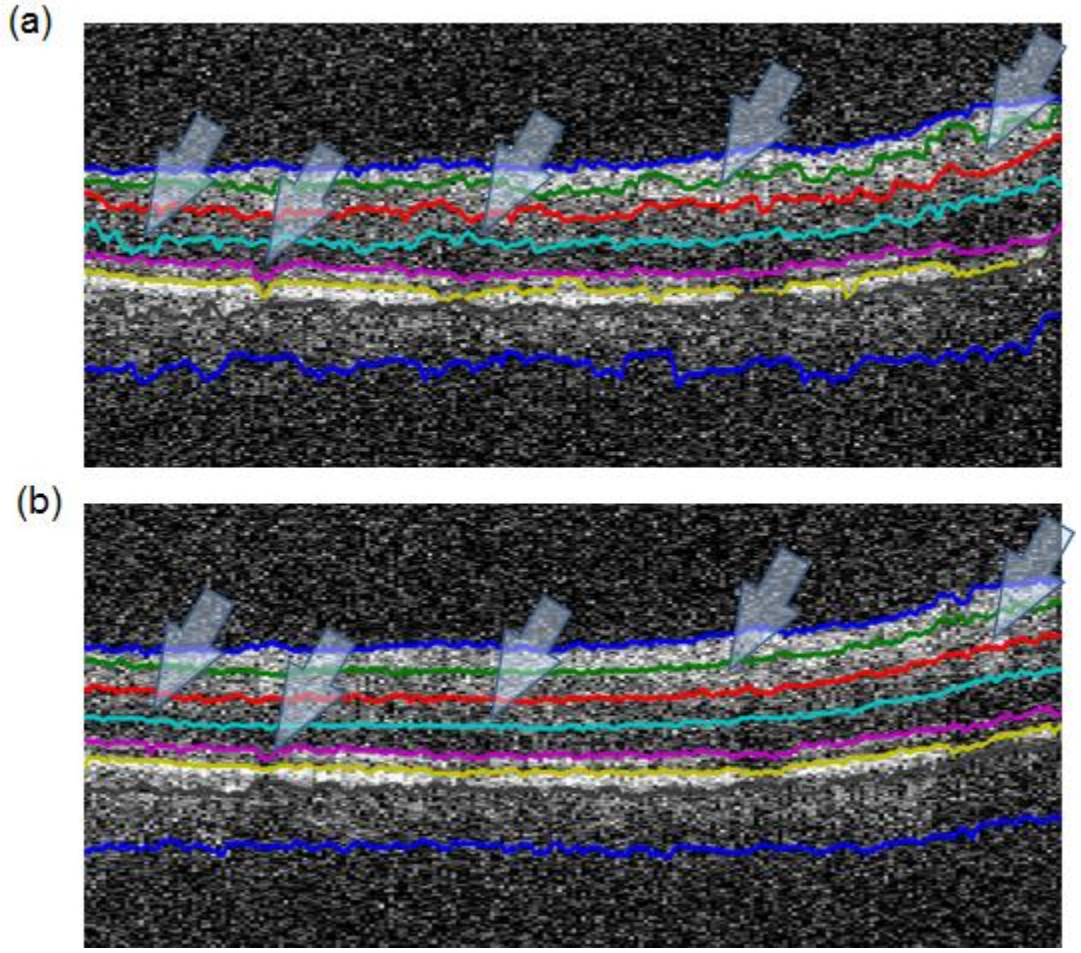

Figure 18: Segmentation results on artificial OCT images using (a) 2D active contour and (b) 3D active contour. Arrows show the boundaries misdetected in 2D algorithm while successfully detected in 3D algorithm.

2.6.3. Speed Test

According to experiments, the curvature operation in (21) takes 94% of computation time during contour evolution with simple MATLAB implementation. The algorithm can be much faster if the computation speed of curvature operation is improved.

GPU implementation significantly improves the computation speed of the curvature operation. To demonstrate this, the algorithm was deployed on a computer equipped with an Intel Core i5-2400 CPU and an ATI 7970 GPU. A benchmark test was performed to compare the computation time of the curvature calculation using (1) regular CPU implementation using MATLAB, (2) parallelized CPU implementation using OpenCL; (3) parallelized GPU implementation using OpenCL. The test data is a 205×100×496 random matrix, which has the same size as the 3D OCT volume used in previous demonstration. The GPU implementation improves the computation speed by an impressive 54× compared with a regular CPU implementation using MATLAB or 1.7× compared with a parallelized CPU implementation using OpenCLV (Table 2).

Implementation	**Processor**	**Time for one curvature operation (ms)**	**GPU improves by**
Regular CPU using MATLAB	Intel Core i5-2400 @ 3.1GHz	8806	54×
Parallelized CPU using OpenCL	Intel Core i5-2400 @ 3.1GHz	280	1.7×
Parallelized GPU using OpenCL	AMD 7970	163	--

Table 2: Computation time required to complete one curvature operation.

2.7. DISCUSSION

Although active contour has been previously demonstrated for segmenting retinal sublayers, the proposed algorithm has a number of important novelties: (1) First demonstration of a 3D active contour for OCT retinal image segmentation. (2) First demonstration of an active contour model with GPU implementation for OCT retinal image segmentation. (3) A novel shape term designed and implemented for retinal segmentation.

The algorithm is 3D and region based. The 3D approach has an inherent advantage in accuracy and noise tolerance over previous 2D methods because more image information is used. As a result, unlike 2D methods, no filtering or noise reduction is required. One potential issue with the 3D based algorithm is eye movement, which may affect the image continuity between frames. Eye movement is usually not a problem with modern high-speed OCT systems, and can be easily fixed with an extra frame-by-frame registration step.

While the segmentation algorithm performed well, improvements can be made, especially on the shape term. The shape term attracts the contour towards an expected boundary location $B_i(x, y)$. Currently, the expected boundary location $B_i(x, y)$ is estimated from the weighted sum of the previous contour C_{i-1} and the next contour C_{i+1}. This method usually makes a reasonable estimate of the expected boundary location, but may make mistakes upon bad initialization of the contours. A more reasonable estimate of the expected boundary location can be achieved from a statistical learning from a retinal image database. The database learning provides an averaged shape model of human retina which gives a better estimate of the expected boundary location.

Another possible improvement could be made with the implementation of the algorithm. Currently, the contour evolution is implemented on a CPU-GPU hybrid

computing architecture. GPU processes only the curvature calculation, which is a series of basic image operations with Laplacian, gradient calculation, while all other operations like the calculation of Heaviside step function are performed on CPU. The hybrid architecture requires additional processing time to transfer data between main memory and GPU memory. If the whole algorithm is implemented on GPU, the performance of the algorithm will be further improved.

2.8. CONCLUSION OF THIS CHAPTER

Speckle noise in OCT images makes the segmentation of retinal sublayer a challenging problem. Traditional gradient-based segmentation methods that rely on sharp image edges fail in such a high noise environment. Here, the fully-automatic segmentation algorithm based on 3D active contour model successfully detects all the 9 retinal sublayers on 3D OCT images. The algorithm includes a region-based image term to eliminate the dependency on shape image edges with high gradient, thus shows better noise tolerance than traditional gradient-based methods. With a novel shape term, segmentation results on human retinal images using the proposed algorithm show 96.8% agreement with manual segmentation during an initial accuracy test. GPU acceleration of the algorithm achieves a 54× speed-up of the curvature computation compared with regular CPU implementation. A noise tolerance test suggests the algorithm has a clear advantage over previously reported 2D active contour models. Application of the high-speed three-dimensional active contour algorithm shows promising clinical value to analyze retinal OCT images.

Chapter 3: Polarization-Sensitive Optical Coherence Tomography (PS-OCT) for Human Retinal Imaging

3.1. Introduction and Motivation

Optical coherence tomography (OCT) provides real time non-invasive cross-sectional images by measuring backscattered light [18]. As a functional extension of OCT, polarization-sensitive OCT (PS-OCT) is capable of characterizing the polarimetric properties of a birefringent sample including form-birefringence, phase retardation and optical-axis orientation, by measuring the interference fringe intensity and relative phase delay of two orthogonal polarization states [44-46].

PS-OCT systems were first implemented with bulk optics [44, 45, 47]. With the development of high speed spectral and Fourier domain OCT, fiber-based PS-OCT systems were developed later [46, 48, 49]. Fiber-based systems have advantages in compact size and easy alignment, but at the cost of polarization mode dispersion, more complicated hardware, and more difficulties in signal processing.

Fiber-based PS-OCT sytems have been built with both polarization-maintaining fiber (PMF) and single mode fiber (SMF) [50-60]. PMF acts as a birefringent waveguide and decorrelates orthogonal polarization states of light propagating in the fiber. The disadvantage of a PMF implementation of PS-OCT is that the propagation velocity of the light in the two orthogonal states is different in PMF, so additional hardware or software is required to compensate the length mismatch of sample and reference arms [50-52]. SMF randomly transforms the polarization state of transmitted light with a unitary transformation, so the SMF-based PS-OCT requires additional optical signal processing to account for the transformation in polarization states [53-60].

Multiple PS-OCT hardware and signal processing designs have been reported. Using TD-PS-OCT Saxer *et al* used a Stokes formalism to determine the rotation axis of

Stokes vectors on the Poincare sphere [46]. Roth *et al* used an algebraic method and polarization sensitive free space components in the sample arm to measure birefringence [61]. Park *et al* developed a Jones matrix approach with sequential polarization modulation to measure the four elements of the Jones matrix representing the polarimetric properties of the sample [62]. Jiao *et al* used two superposed light sources [63], and later demonstrated continuous polarization modulation [64]. Davé *et al* used polarization maintaining (PM) fiber to characterize retardance and axis orientation of a birefringent plate with a single A-scan [50]. Oh *et al* was able to measure sample birefringence with only one wavelength scan without depth limitation but using additional frequency shifters [65]. Yamanari *et al* used a modulated input polarization state, requiring only one A-scan to calculate sample retardation at the expense of a reduction in measurement depth by a factor of three [66]. Al-Qaisi *et al* was able to record an image of biological tissue free of ghost lines using PM fiber [52].

In recent years, PS-OCT has been investigated for promising applications in detecting early stage glaucoma by measuring the thickness and birefringence of the retinal nerve fiber layer (RNFL) [58, 67-70]. Compared with normal eyes, RNFL thickness and birefringence both decrease in glaucoma eyes [68, 71]. According to previous studies, RNFL is a birefringent layer, and its form birefringence is mostly contributed by the microtubules within retinal ganglion cells (RGCs) [72]. In glaucomatous retinas, RGC microtubules depolymerize and eventually degrade, because of the reduced number of microtubule associated proteins (MAPs) which promote the oriented polymerization and assembly of microtubules [73-75]. As a result, in glaucomatous retinas, degenerate RGC axons are replaced by non-birefringent glial cells, so RNFL birefringence is expected to decline earlier and at a faster rate than RNFL thickness [76].

With appropriate polarimetric models [57, 77] and carefully defined RNFL boundaries, RNFL birefringence which provides functional information of microtubule density can be recovered from PS-OCT data [58, 78], and therefore one might expect that glaucoma can be detected at an earlier stage.

In this chapter, a single-mode-fiber based swept-source polarization-sensitive OCT system was constructed for imaging human retina [58, 79]. Peri-papillary RNFL thickness, birefringence, and phase retardation maps are constructed from healthy eyes. As an example PS-OCT application, a RNFL segmentation algorithm using RNFL's polarimetric information is described at the end of this chapter.

Imaging protocols utilized to record data described hereafter have been approved by the Institutional Review Board of the University of Texas at Austin (IRB protocol # 2007040101) and are registered (NCT # 01222065).

3.2. POLARIZATION-SENSITIVE OPTICAL COHERENCE TOMOGRAPHY (PS-OCT) SYSTEM

A fiber-based swept-source PS-OCT system for human retinal imaging is constructed (schematics shown in Figure 19) [58, 79]. The PS-OCT is assembled in a mobile cart to be ready for clinical use (Figure 20). The PS-OCT system utilized a swept-source laser (HSL-1000 by Santec Corp., Komaki, Aichi, Japan) with a sweep rate of 28 kHz, 1064 nm center wavelength and a spectral scan range of 80 nm, providing an axial resolution of 12 μm in tissue.

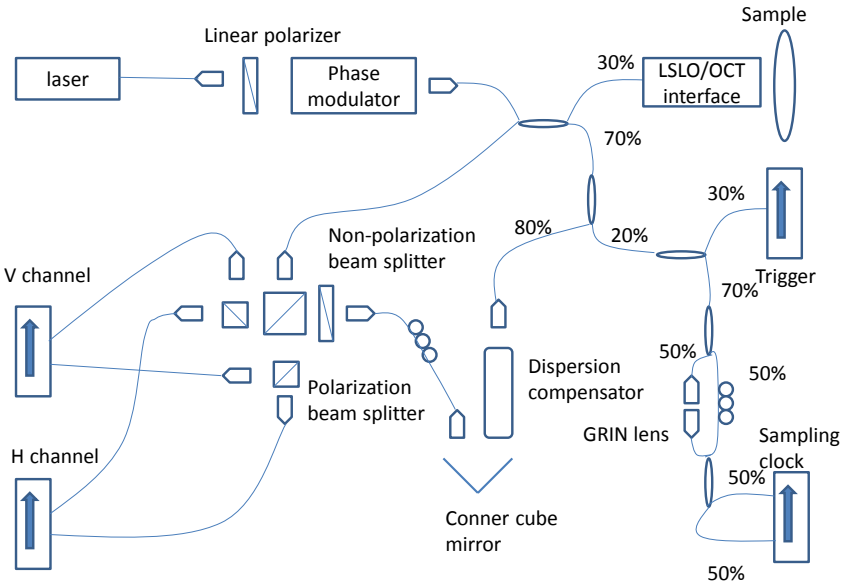

Figure 19: Schematic of fiber-based swept-source polarization-sensitive OCT system [79].

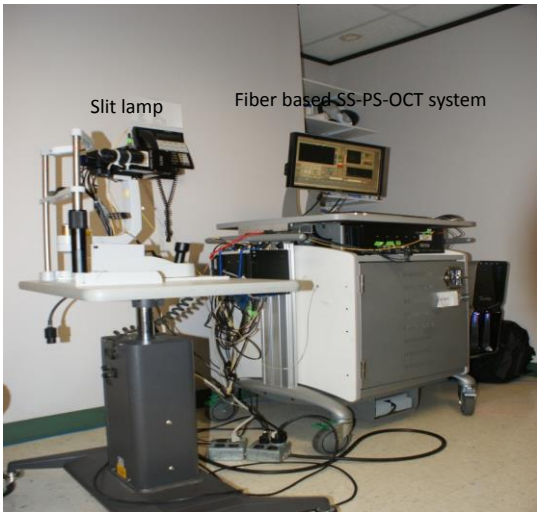

Figure 20: PS-OCT clinical system setup [79]. Slit lamp is on the left. Fiber-basd swept-source PS-OCT system is on the right.

The incident polarization state input into the PS-OCT system is adjustable with a polarization controller consisting of a linear polarizer and an electro-optic phase modulator. The phase modulator is composed of two lithium niobate crystals with equal length and oriented at 90 degrees, in order to cancel intrinsic dispersion of their native birefringence. When the phase modulator is electrically controlled with a high-voltage amplifier, the light exiting the polarization controller is polarized in three polarization states at 0 degree, 120 degrees and -120 degrees on the QV plane of the Poincaré sphere.

The PS-OCT system requires a polarization-sensitive balanced detection module with two detection channels recording interference fringe signals in orthogonal polarization directions. The detection module was firstly built with a fiber-based implementation [58], but later switched to a bulk-optics [79] because of unmatched polarization state changes in the optical fiber. In the detection module (Figure 21), a non-polarization crystal beam splitter is used for balanced detection, and two polarization beam splitters separate interference signals into balanced vertical and horizontal channels.

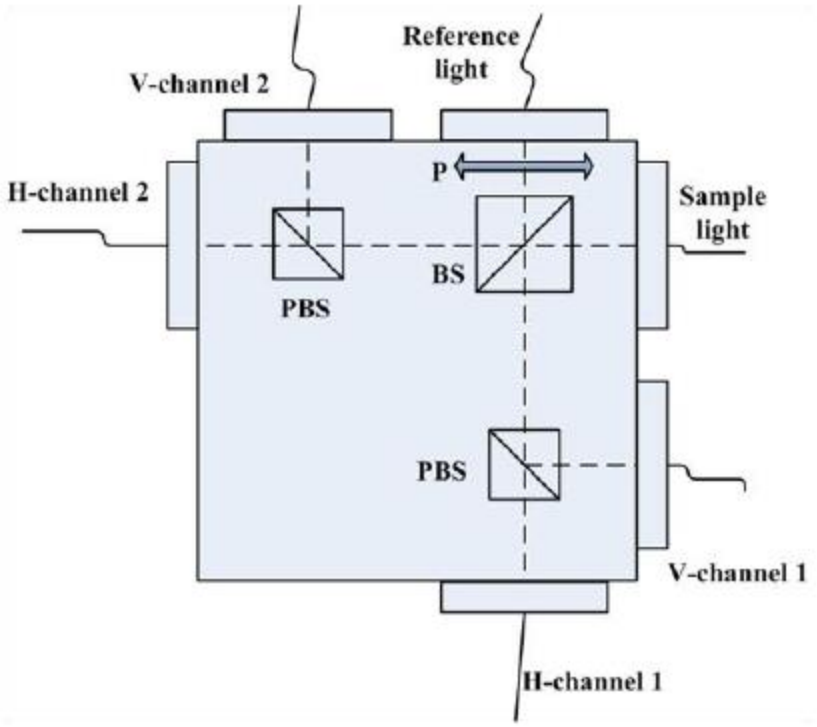

Figure 21: Schematic of Polarization-sensitive balanced detection module. BS: beam splitter. PBS: polarizing beam splitter.

The PS-OCT sample arm is composed of a patient interface which delivers the light onto the cornea as well as a line scanning laser ophthalmoscope (LSLO). A glass rod is used as the dispersion compensator in the reference arm. A Mach-Zehnder interferometer (MZI) is used as the sampling clock to ensure sampling of the signal in linear wavenumber space. The clocking MZI is connected to an external circuit board to quadruple the sampling rate.

3.3. FINDING TISSUE BIREFRINGENCE

3.3.1. Stokes Vector Based Polarimetric Analysis

The interference fringe signals collected with PS-OCT requires a polarimetric model in order to determine the sample's birefringence. The polarimetric processing

procedure was described previously [58]. Briefly, the horizontal and vertical component of interference fringe signals ($E_h(z)$, $E_v(z)$) and the relative phase retardation between the two orthogonal polarization states ($\varphi_{diff}(z)$) are first cropped to the anterior and posterior RNFL boundaries. The normalized Stokes vectors $S(z)$ which represents the polarization states at each depth-resolved pixel are then calculated from $E_h(z)$, $E_v(z)$ and $\varphi_{diff}(z)$. RNFL phase retardation, birefringence and optical-axis orientation are estimated from a multiple-state Levenberg-Marquardt nonlinear fitting algorithm. The polarimetric processing procedure is described in more details below:

In the current PS-OCT system, the complex depth-resolved electric field amplitudes for horizontal $E_H(z)$ and vertical $E_V(z)$ axes are acquired with two digitizer channels. The phase difference $\varphi_{diff}(z)$ between the two channels is computed. To analyze the change in polarization state of light as a function of depth, the normalized Stokes vector S_z, which describes the polarization state of light at a given depth, is computed at each depth from $E_H(z)$, $E_V(z)$ and $\varphi_{diff}(z)$ by:

$$S_z = \begin{pmatrix} Q_z \\ U_z \\ V_z \end{pmatrix} = \begin{pmatrix} E_V(z)^2 - E_H(z)^2 \\ 2E_V(z)E_H(z)\cos\left(\varphi_{diff}(z)\right) \\ 2E_V(z)E_H(z)\sin\left(\varphi_{diff}(z)\right) \end{pmatrix} \Big/ \left(E_V(z)^2 + E_H(z)^2\right) \tag{23}$$

If S_z is plotted in a three dimensional coordinate system of $Q-U-V$, it always falls on the surface of a unit radius sphere called the Poincaré sphere [53, 54]. RNFL is considered as a birefringent sample without biattenuation. In this case, the trajectory of depth-resolved normalized Stokes vector S_z in RNFL depth traces a circular polarization arc with depth z around the optic axis $\hat{\beta}$ on Poincaré Sphere (Figure 22). The central angle of the polarization arc corresponds to double pass phase retardation (DPPR) due to the sample birefringence.

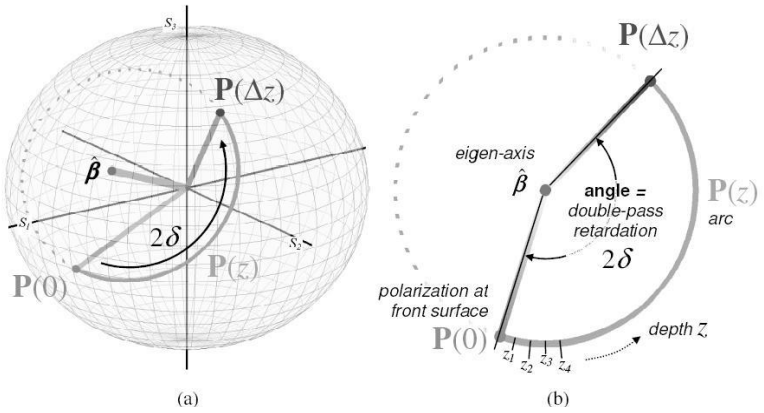

Figure 22: Depth-resolved normalized Stokes vector S_z in RNFL depth traces a polarization arc with depth z around the optic axis $\hat{\beta}$ on Poincaré sphere. The central angle of the polarization arc is determined by the double pass phase retardation (DPPR) caused by sample birefringence.

In order to better estimate RNFL birefringence from PS-OCT data, a longer polarization arc on Poincaré sphere is desired. The length of the polarization arc is dependent on the separate angle between optic axis and the initial Stokes vector. To increase the probability of having a long polarization arc, three incident polarization states (pairs separated by 120°) are used in the current PS-OCT system, as discussed above. The three polarization arcs are constrained to rotate about the same optic axis by the same phase delay.

A mathematical model describing the circular trajectory of depth-resolved Stokes vector on Poincaré Sphere is detailed discussed in previous publications [53, 54, 58]. When biattenuation is negligible, the model contains a total of 9 unknown parameters: Stokes vector of sample optical axis with azimuthal and polar angle (φ_0, θ_0), the azimuthal and polar angles for the Stokes vectors of three incident states (φ_1, θ_1), (φ_2, θ_2), (φ_3, θ_3), and double pass phase retardation per unit depth (DPPR/UD) δ. The model function describing the trajectory of arcs can be constructed based on Euler rotation

matrix and these 9 parameters. The physical description of the model is skipped here (with details in previous publications [53, 54, 58]); only its mathematical conclusion is summarized below:

First, two axis systems are defined. Lab frame is denoted as $Q-U-V$ as mentioned above, while a sample frame $Q'-U'-V'$ is transformed from the lab frame with a Euler rotation matrix:

$$\begin{pmatrix} \sin\theta_0\cos\varphi_0 & -\sin\varphi_0 & -\cos\theta_0\cos\varphi_0 \\ \sin\theta_0\sin\varphi_0 & \cos\varphi_0 & -\cos\theta_0\sin\varphi_0 \\ \cos\theta_0 & 0 & \sin\theta_0 \end{pmatrix} \tag{24}$$

Assuming the cone angle between optic axis and the 1st incident polarization state is β, then

$$\begin{aligned} \cos\beta &= \sin\theta_0\cos\varphi_0\sin\theta_1\cos\varphi_1 + \sin\theta_0\sin\varphi_0\sin\theta_1\sin\varphi_1 + \cos\theta_0\cos\theta_1 \\ \sin\beta &= \sqrt{1-\cos^2\beta} \end{aligned} \tag{25}$$

Define another angle parameter α, which is the angle between the projection of the 1st incident polarization state on $U'V'$ plane, while U' and V' axes are respectively $(-\sin\varphi_0, \cos\varphi_0, 0)$ and $(-\cos\theta_0\cos\varphi_0, -\cos\theta_0\sin\varphi_0, \sin\theta_0)$ in lab frame ($Q-U-V$ axes).

$$\alpha = \text{atan2}\frac{-\sin\theta_1\cos\varphi_1\cos\theta_0\cos\varphi_0 - \sin\theta_1\sin\varphi_1\cos\theta_0\sin\varphi_0 + \cos\theta_1\sin\theta_0}{-\sin\theta_1\cos\varphi_1\sin\varphi_0 + \sin\theta_1\sin\varphi_1\cos\varphi_0} \tag{26}$$

In the $Q'-U'-V'$ coordinate system, the Stokes vector for light backscattered from depth *z* is written as

$$\begin{aligned} Q'_z &= \cos\beta \\ U'_z &= \sin\beta\cos\left(\alpha + 2(z-1)\delta\right) \\ V'_z &= \sin\beta\sin\left(\alpha + 2(z-1)\delta\right) \end{aligned} \tag{27}$$

where δ is double pass phase retardation per unit depth (DPPR/UD) as mentioned above.

Converting the above Stokes vector from $Q'-U'-V'$ to $Q-U-V$ lab coordinate system with the Euler rotation matrix gives:

$$S_z = \begin{pmatrix} Q_z \\ U_z \\ V_z \end{pmatrix} = \begin{pmatrix} \sin\theta_0 \cos\varphi_0 & -\sin\varphi_0 & -\cos\theta_0 \cos\varphi_0 \\ \sin\theta_0 \sin\varphi_0 & \cos\varphi_0 & -\cos\theta_0 \sin\varphi_0 \\ \cos\theta_0 & 0 & \sin\theta_0 \end{pmatrix} \begin{pmatrix} Q_z' \\ U_z' \\ V_z' \end{pmatrix} \tag{28}$$

The depth-resolved normalized Stokes vector S_z is calculated from acquired OCT signal using (17). So (22) completes an equation set with 9 unknown parameters.

Based on the Stokes vector based polarimetric model, with the measured and cropped-to-RNFL $E_h(z)$, $E_v(z)$ and $\varphi_{diff}(z)$, the double pass phase retardation (DPPR) and DPPR per unit depth (DPPR/UD) δ of RNFL are estimated using a multiple-state Levenberg-Marquardt nonlinear fitting algorithm, which is a standard algorithm to estimate a set of parameters that best correlates experimentally observed data to a theoretical model in terms of least square error [80]. The asymptotic standard error, or uncertainty of birefringence, is calculated from the nonlinear fitting algorithm as an error measure for the estimated birefringence with a 95% confidence interval [80].

Figure 23 shows two sample PS-OCT data recorded from a healthy volunteer's right eye on the Poincaré sphere. The polarimetric speckle noise corrupted data appear as arcs on the Poincaré sphere and can be inversed to estimate the optic axis $\hat{\beta}$ and RNFL birefringence Δn according to the polarimetric model described above [77]. Figure 23(a) shows a 46 μm thick RNFL location with measured DPPR of 9.68°, equivalent to DPPR/UD of 21.05°/100 μm, with 0.36°/100 μm (1.71%) DPPR/UD uncertainty. Figure 23(b) shows a 158 μm thick location with measured DPPR of 54.02°, equivalent to DPPR/UD of 34.14°/100 μm, with 0.24°/100 μm (0.70%) DPPR/UD uncertainty.

The main challenge of Stokes vector based polarimetric analysis is the high computational requirement. The Levenberg-Marquardt non-linear fitting algorithm requires the inversion of a 9 × 9 matrix which is computationally intensive. The computational speed can be dramatically improved with implementation in a field

programmable gate array (FPGA) based computational system which executes parallel tasks at the hardware level. The FPGA implementation of Levenberg-Marquardt algorithm is estimated to be 300-600 fold faster than the current MATLAB implementation on a personal computer [79].

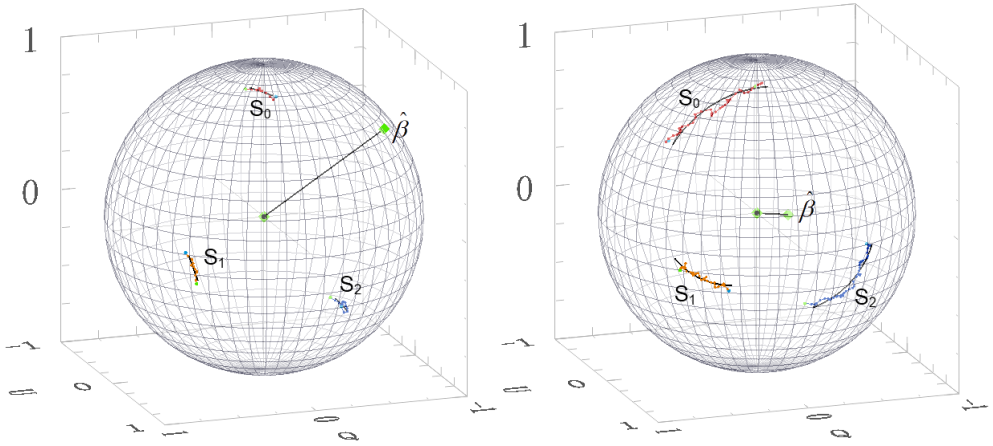

Figure 23: Polarimetric noise corrupted arcs for the three polarization states and their noise free fits about the optic axis on the Poincaré Sphere. (a) A 46 µm thick RNFL location with measured DPPR of 9.68°, equivalent to DPPR/UD of 21.05°/100 µm, with 0.36°/100 µm (1.71%) DPPR/UD uncertainty. (b) A 158 µm thick location with measured DPPR of 54.02°, equivalent to DPPR/UD of 34.14°/100 µm, with 0.24°/100 µm (0.70%) DPPR/UD uncertainty.

3.3.2. Scan Pattern Considerations for PS-OCT

3.3.2.1. Clustered Ring Scan

Polarization data acquisition is sensitive to speckle noise which is present in all interferometric imaging techniques. In order to reduce speckle noise, we designed a clustered ring scan pattern (Figure 24). The clustered ring scan pattern consists of 10 concentric rings around the optic nerve head with 2-5 mm diameters, and each ring contains 36 clusters of 100 A-lines. In each cluster the 100 A-lines are acquired by sampling a sinusoidal pattern of 5 periods. For each A-line, depth-resolved data are

recorded with three input polarization states as described above. The 100 A-lines in each cluster are assumed to be uncorrelated and sample identical polarimetric properties since they are acquired over a relatively small spatial region. Averaging N_A=100 uncorrelated A-lines increases polarization signal-to-noise ratio (PSNR) by approximately $\sqrt{N_A}$=10 times [81].

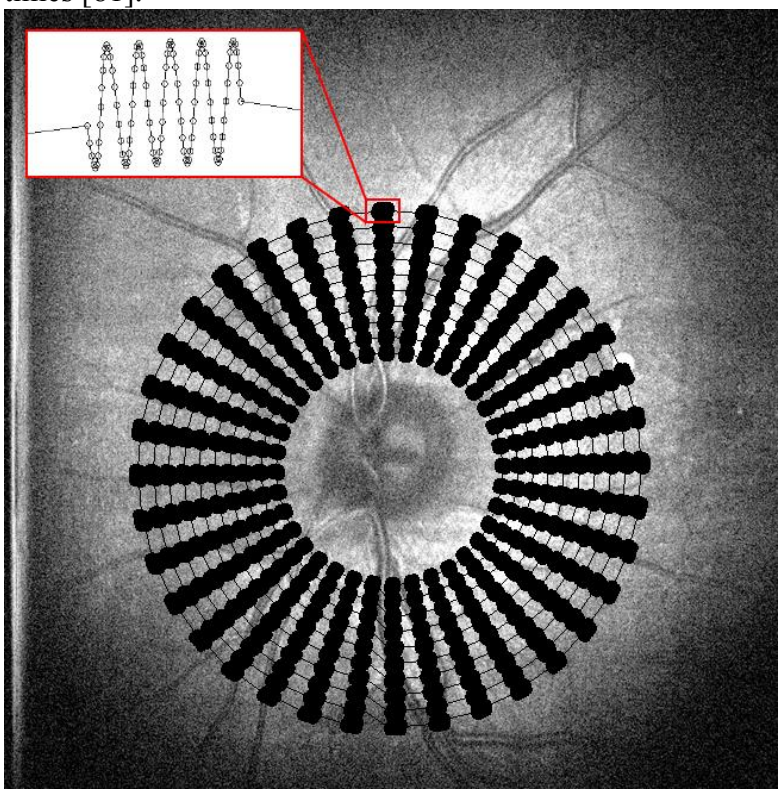

Figure 24: A line-scanning laser ophthalmoscope (LSLO) image showing clustered ring scan pattern around ONH. A clustered ring scan is composed of 10 rings. Each ring contains 36 clusters, and each cluster contains 100 A-lines.

The clustered ring scan produces clustered maps of RNFL thickness, birefringence and phase retardation. RNFL thickness map (Figure 25(a)) is obtained using a simple RNFL segmentation algorithm from OCT B-scan images. Birefringence (DPPR/UD) map (Figure 25(b)) and its uncertainty map (Figure 25(c)) are calculated from the multiple-state Levenberg-Marquardt nonlinear fitting algorithm. Phase

retardation map (Figure 25(d)) is obtained by multiplying thickness by birefringence. Blood vessels acquired from the raster scan taken immediately before acquisition of the clustered data are superimposed on the clustered RNFL thickness, birefringence, and phase retardation maps for registration.

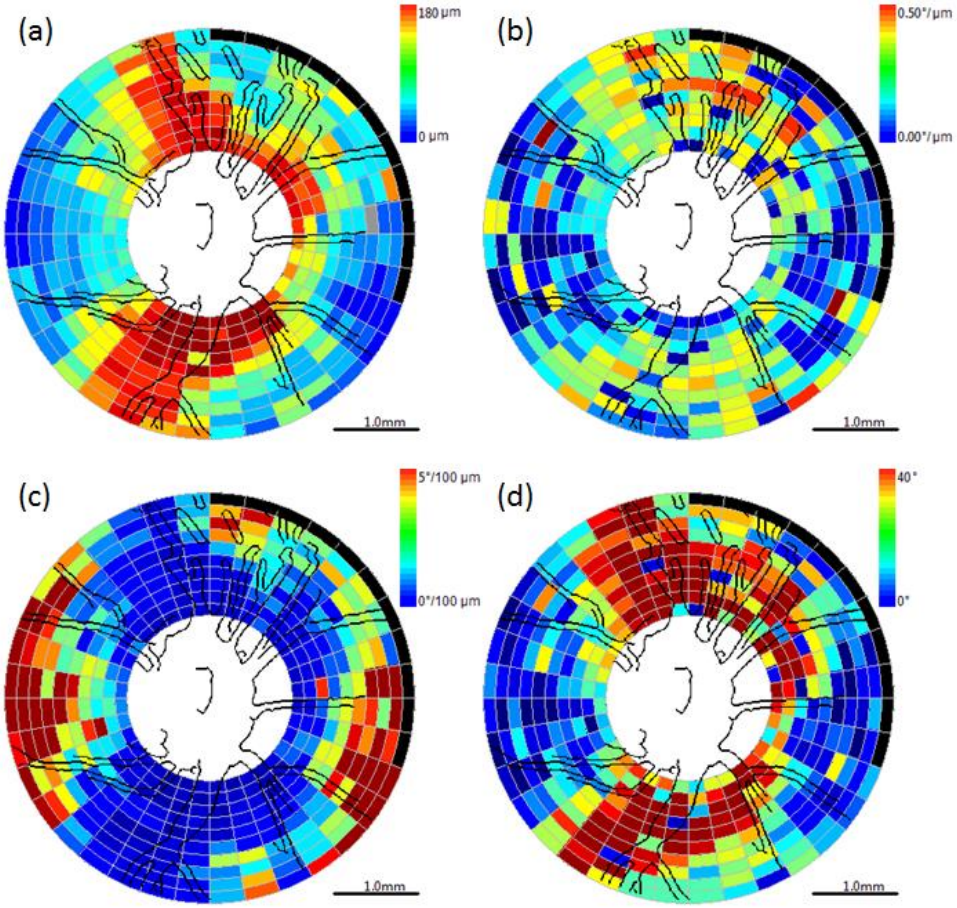

Figure 25: Clustered maps from the same clustered ring scan. Blood vessels are detected from a separate raster scan taken immediately before acquisition of the clustered data. (a) Thickness map; (b) Birefringence (DPPR/UD) map; (c) Uncertainty of birefringence map; (d) Phase retardation (PR) map.

The scan pattern of clustered ring scan exhibits some clear disadvantages. Although it is capable of reducing polarimetric speckle noise by averaging within each cluster, the number of measurement spots is significantly limited. It provides only 360

measurement spots with 108000 A-scans (3 polarization states/A-line × 100 A-lines/cluster × 36 clusters/ring × 10 rings). Comparing with conventional intensity OCT which provides continuous fundus images with similar number of A-scans, the birefringence information provided by PS-OCT with clustered ring scan is clearly undersampled.

3.3.2.2. Adaptive Cluster Forming Scan

As discussed above, the reason of using clustered ring scan is to reduce polarimetric speckle noise which corrupts the calculation of intensity-normalized Stokes vectors. By averaging N_A uncorrelated A-scans over a small lateral area, the polarimetric speckle noise is reduced by $\sqrt{N_A}$ times. However, clustered ring provides coarse and undersampled sampling locations on fundus therefore its clinical utility is limited. Although it is possible to increase the number of sampling locations in clustered ring scan by arranging more rings and/or more clusters per ring on fundus at the expense of recording more A-scans, the improvement is constrained by the limited acquisition time which must be shorter than 5 s due to patients' eye movement in practice.

The cost performance of clustered ring scan can be dramatically improved by adaptively including and reusing A-scans in multiple clusters. Based on a continuous ring scan or raster scan, a moving window is defined and scan over the sampling area. The A-scans in the moving window are considered uncorrelated thus provide a cluster for polarimetric processing. As an example, the relative size of the moving window comparing with the scan area of a continuous ring scan is shown in Figure 26. By specifying the step size of the moving window, continuous maps of RNFL birefringence and phase retardation can be generated. The continuous ring scan pattern shown in Figure 26 contains 100 rings and 360 A-scans per ring. The total number of A-scans is

108000 (3 polarization states/A-line × 360 A-lines/ring × 100 rings), same as the number of A-scans in the current clustered ring scan pattern. But the proposed strategy provides 2500 (50×50) sampling locations – almost 7 times improvement comparing with the 360 sampling locations in the current clustered scan.

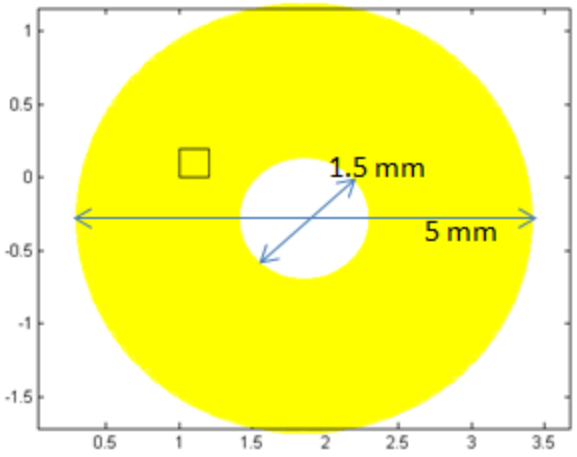

Figure 26: Relative size of the moving window comparing with the scan area of a continuous ring scan.

Example continuous maps generated from this cluster forming scan pattern are shown in Figure 27(d-f). Comparing with the discrete maps created from clustered ring scan from the same subject Figure 27(a-c), the continuous maps generated from the proposed scan pattern clearly conveys more details about RNFL birefringence and phase retardation.

An important advantage of the proposed adaptive cluster forming scan pattern is the ease of applying image processing techniques on continuous maps. RNFL birefringence and phase retardation is physiologically continuous. However, large local variation of RNFL birefringence and phase retardation presents on both discrete maps and continuous maps. The local variation is usually caused by inaccurate or even failed Levenberg-Marquardt fitting of the polarimetric model on Poincaré sphere. In clustered

ring scan, those problematic clusters make it difficult to make diagnostic decision with discrete RNFL birefringence and phase retardation maps. With the adaptive cluster forming scan pattern, the local variation can be significantly reduced with a median filter on the noisy continuous maps (Figure 27(h,i)).

As mentioned above, the performance of polarimetric speckle noise reduction is dependent on the number of A-scans included in a cluster. In continuous ring scan, the density of A-scans is higher in inner rings than in outer rings because of the identical number of A-scans per ring. As a result, clusters in inner rings have a higher number of A-scans (Figure 27(g)). The non-uniform reduction of polarimetric speckle noise is sometimes unwanted. A raster scan based adaptive cluster scan is also developed with uniform A-scan density (Figure 28).

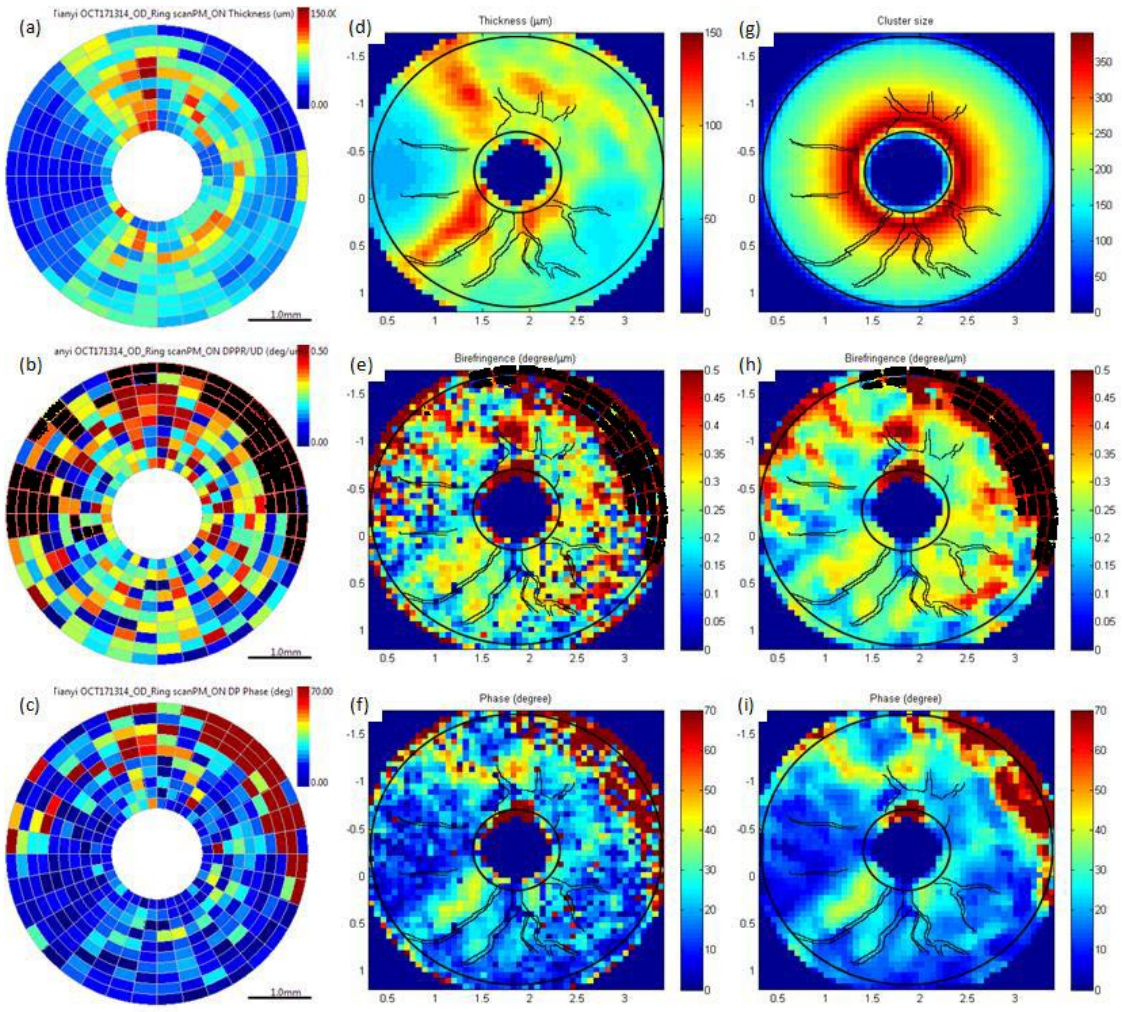

Figure 27: Comparison of discrete maps created from clustered ring scan and continuous maps created from the proposed adaptive cluster forming scan pattern. (a) Discrete RNFL thickness map; (b) Discrete RNFL birefringence map; (c) Discrete RNFL phase retardation map; (d) Continuous RNFL thickness map; (e) Continuous RNFL birefringence map; (f) Continuous RNFL phase retardation map; (g) Number of A-scans in each cluster in the adaptive cluster forming scan pattern; (h) Continuous RNFL birefringence map filtered by a median filter; (i) Continuous RNFL phase retardation map filtered by a median filter.

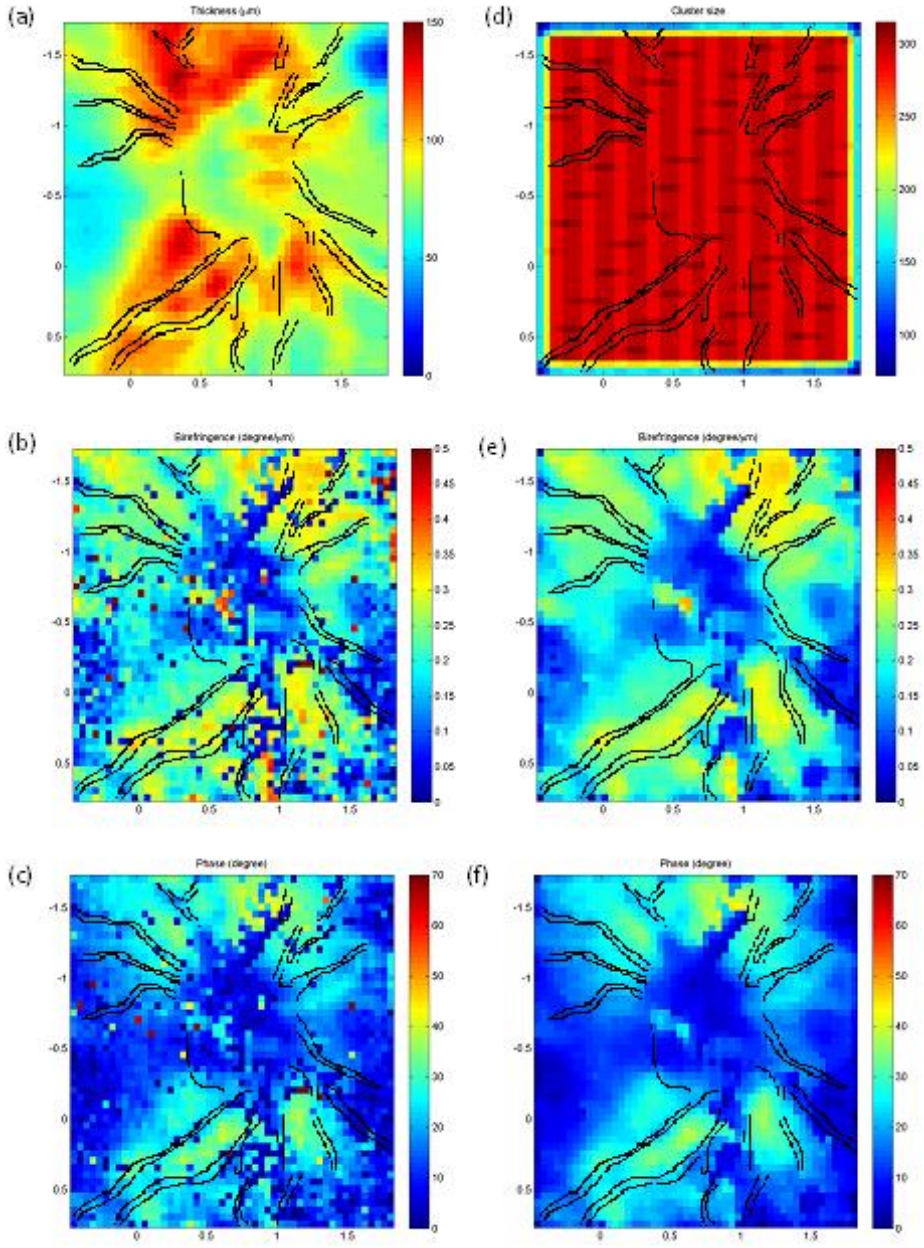

Figure 28: Continuous maps created from the raster scan using the proposed adaptive cluster forming strategy. (a) Continuous RNFL thickness map; (b) Continuous RNFL birefringence map; (c) Continuous RNFL phase retardation map; (d) Number of A-scans in each cluster in the adaptive cluster forming scan pattern; (e) Continuous RNFL birefringence map filtered by a median filter; (f) Continuous RNFL phase retardation map filtered by a median filter.

3.4. Application of PS-OCT: Optimized RNFL Boundary Detection Using Polarimetric Measurement

3.4.1. Motivation

Segmentation of the RNFL from PS-OCT images is fundamental to determine RNFL thickness and birefringence. PS-OCT polarimetric processing algorithms are sensitive to even slight misdetection of RNFL boundaries. Many RNFL segmentation methods based on image processing and boundary detection algorithms have been reported and are summarized in Chapter 2. Most of the previous RNFL segmentation algorithms provide promising RNFL segmentation results. However, none of them are optimized for estimation of RNFL birefringence using PS-OCT for several reasons. First, the previous algorithms are designed for continuous ring scan or raster scanning patterns, rather than a discrete clustered ring scanning pattern currently employed in PS-OCT systems required to minimize degrading effects of speckle noise in polarimetric signals. Second, all of the previous methods utilize only OCT intensity information of backscattered light, which is strongly corrupted by speckle noise. No reported method takes advantage of functional birefringence information provided by PS-OCT. Third, unlike the anterior RNFL boundary where change of refractive index from vitreous to the inner limiting membrane is abrupt, the posterior RNFL boundary is a transition zone from the birefringent RGC axons to their cell bodies; thus, a physiologically well-defined posterior RNFL boundary does not exist in OCT intensity images. The polarimetric measurement capability of PS-OCT provides additional information to potentially overcome the limitations of current RNFL segmentation approaches for birefringence measurement.

Utilizing both RNFL intensity and polarimetric information, a two-step RNFL segmentation method is proposed here for data recorded from swept source PS-OCT to

achieve optimized RNFL segmentation for birefringence estimation. RNFL boundaries are first estimated from the intensity images using a simple filter followed by thresholding approach. Optimized RNFL segmentation is then achieved by locally moving the estimated RNFL posterior boundary and minimizing uncertainty of estimated RNFL birefringence determined by the Levenberg-Marquadt algorithm. This method segments the RNFL with optimized RNFL birefringence estimation. Performance of the segmentation approach is evaluated using clinical data from a healthy volunteer (NCT# 01222065).

3.4.2. Methods

RNFL anterior and posterior boundaries are first estimated from the recorded OCT intensity image. Figure 29(a) shows an example of a B-scan intensity image derived from a clustered ring scan. For each cluster, the intensity profiles of 100 A-lines are averaged to suppress speckle noise and improve signal-to-noise ratio (SNR), forming a cluster-averaged intensity image as shown in Figure 29(b). Each averaged A-line of the cluster-averaged image is then processed with a smoothing filter to further reduce speckle noise. A threshold is applied to the averaged and filtered A-line to estimate locations of anterior and posterior RNFL boundaries. Finally, the RNFL segmentation is visually inspected and any misdetected boundaries are manually corrected. The results of intensity-based RNFL segmentation are shown in Figure 29(c).

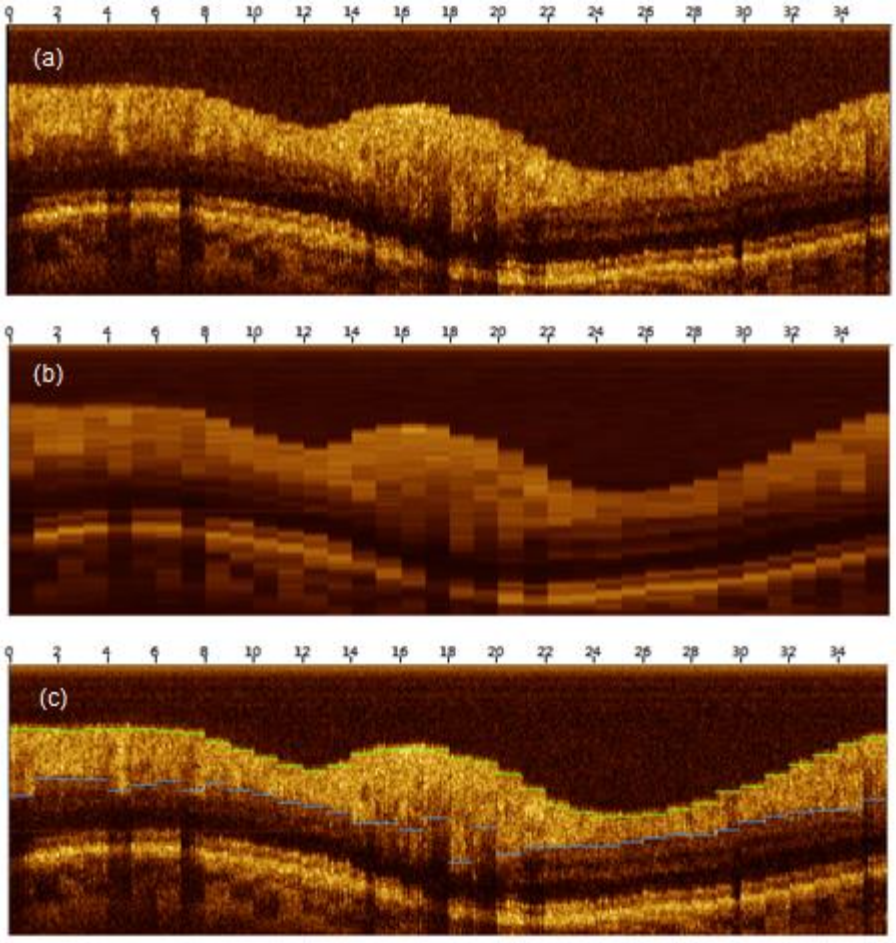

Figure 29: A clustered ring scan acquired about the optic nerve head. Acquired image diameter is 2.3 mm and consists of 36 clusters of 100 A-lines/cluster. Cluster numbers are marked at the top of the image. (a) Original B-scan intensity image from clustered ring scan. (b) Cluster-averaged intensity image provides improved SNR. (c) B-scan intensity image with intensity-based RNFL boundaries.

The anterior RNFL boundary is an interface between the vitreous and inner limiting membrane with strong intensity contrast since the refractive index gradient is large. As a result, the RNFL anterior boundary is relatively easy to detect using the intensity image, and in most cases the RNFL anterior boundary is correctly detected using intensity-based segmentation. However the intensity contrast at the RNFL

posterior boundary is relatively low because the refractive index gradient from the birefringent RGC axons to their cell bodies is small. To achieve the best estimate of RNFL birefringence, posterior RNFL boundary estimates are refined anatomically with polarimetric information by locally adjusting the RNFL posterior boundary and minimizing the uncertainty of the birefringence estimate. A flow chart of this process is shown in Figure 30.

To maintain the RNFL posterior boundary in the transition zone of RGC axons and their cell bodies, the search range of the RNFL posterior boundary is constrained to a relatively small depth. In this study, the search range was constrained to 3 pixels above and below (i.e., ±14.07 μm) the intensity-based RNFL posterior boundary, corresponding to the diameter of two RGC cell bodies (around 14 μm) [82].

Figure 31 shows an example of the effects of the RNFL posterior boundary optimization on the Poincaré Sphere. The intensity-based segmentation misdetects the RNFL posterior boundary by overestimating three pixels. As a result, the Stokes vector trajectory cropped from the misdetected boundary forms arcs with outlier points near the posterior boundaries. These outliers reduce the fitting quality and increase the uncertainty of estimated birefringence (1.09°/100 μm). The optimized RNFL boundary detection successfully removes outliers near the posterior boundary and thus provides better estimates of RNFL birefringence with much lower uncertainty (0.47°/100 μm).

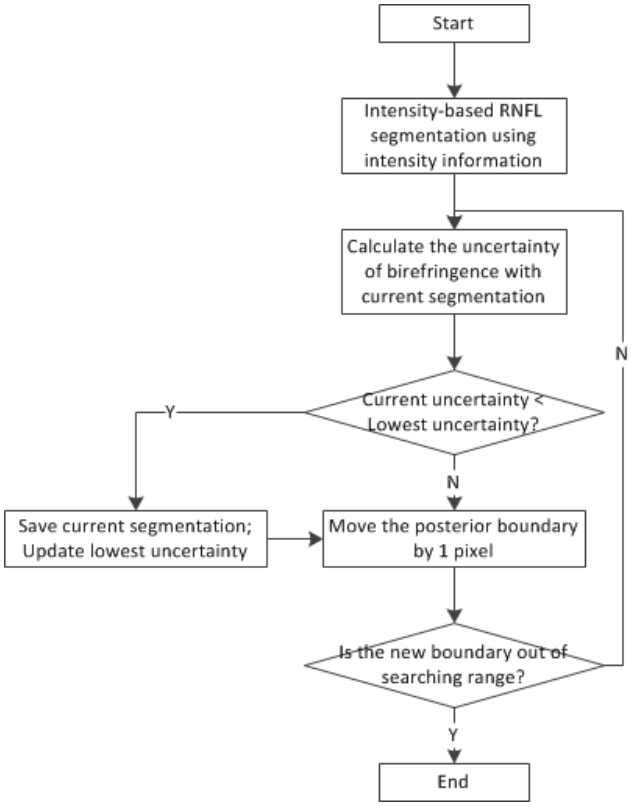

Figure 30: Flow chart of the RNFL boundary optimization algorithm.

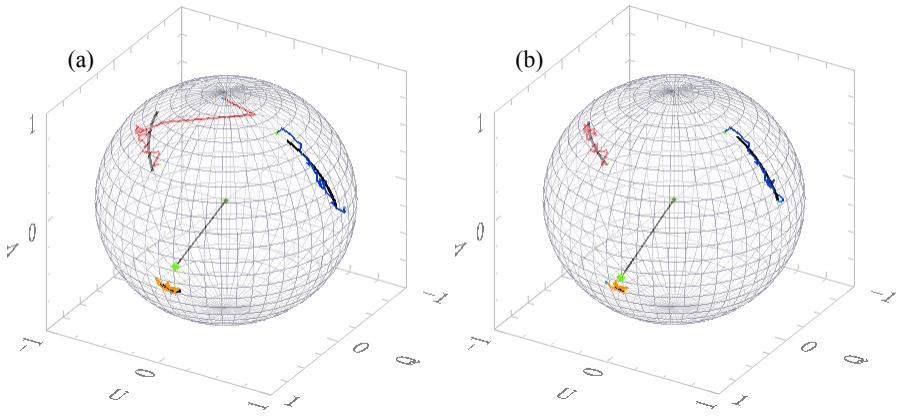

Figure 31: RNFL posterior boundary optimization on the Poincaré Sphere. (a) Intensity-based boundary: RNFL thickness = 36 pixels, uncertainty of birefringence = 1.09°/100 μm. (b) Optimized boundary: RNFL thickness = 33 pixels, uncertainty of birefringence = 0.47°/100 μm.

3.4.3. Results

Discrete clustered maps of uncertainty, thickness, birefringence (double pass phase retardation per unit depth) and phase retardation created with both intensity-based and optimized RNFL boundaries are shown in Figure 32. Blood vessel patterns segmented from a raster scan recorded immediately before acquisition of the clustered data are superimposed on the clustered maps.

As shown in Figure 32(a), the optimized boundary minimizes the uncertainty of the RNFL birefringence estimate compared with the intensity-based RNFL boundary. Although the optimized boundary is confined within a relatively small transition zone near the intensity-based boundary, RNFL thickness calculated from the intensity-based boundary (average thickness 107.60 μm) is generally greater than the optimized boundary results (average thickness 98.77 μm), as shown in Figure 32(b). This result suggests that an intensity-based RNFL boundary detection tends to overestimate RNFL thickness, possibly due to a limitation of simple thresholding.

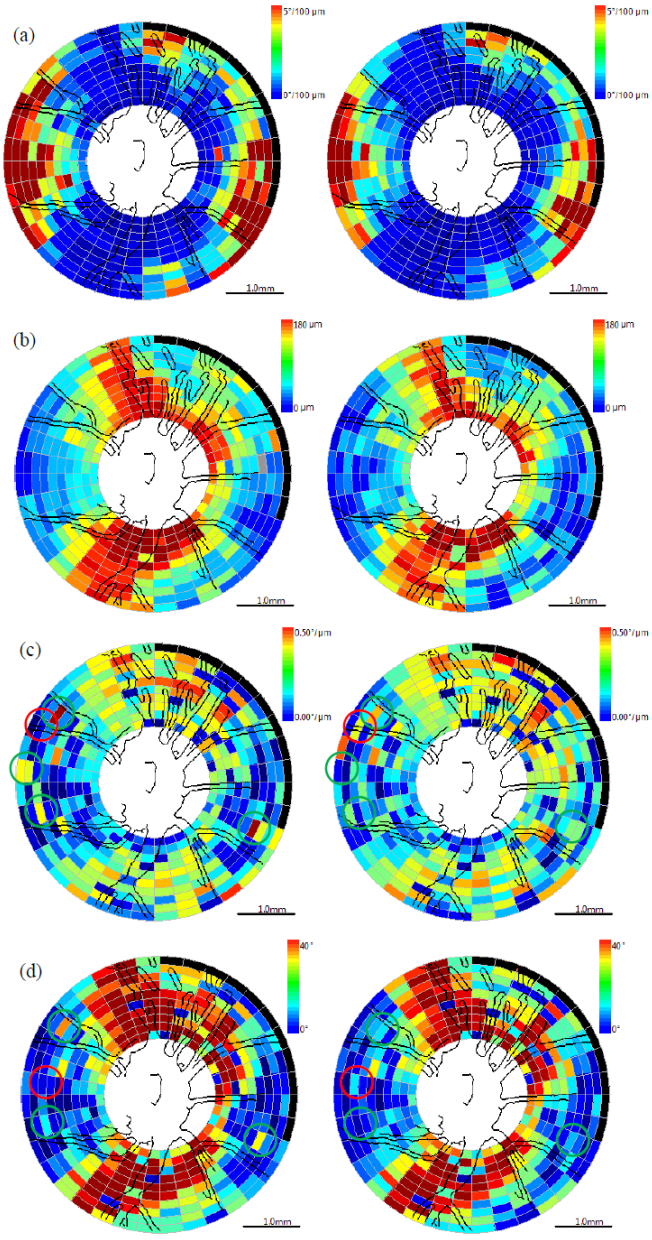

Figure 32: Clustered maps created with intensity-based (left column) and optimized RNFL (right column) boundaries. Unprocessable clusters due to inappropriate operator settings during image acquisition are marked in black. (a) Uncertainty of birefringence. (b) Thickness. (c) Birefringence (double pass phase retardation per unit depth). (d) Phase retardation. Green circles in (c) and (d) mark outlier clusters removed by RNFL boundary optimization, while red circles mark the few new outliers produced by optimized RNFL segmentation.

We evaluate the improvement of RNFL birefringence estimate with the proposed RNFL segmentation by assessing the spatial smoothness of RNFL birefringence and phase retardation. Due to the spatial continuity of RNFL physiology, change of RNFL birefringence and phase retardation on different RNFL locations are expected to be gradual and smooth. Although the sampling pattern of the clustered ring scan is discrete, the local variation in RNFL birefringence and phase retardation maps should be reasonably small. In the RNFL birefringence (Figure 32(c)) and phase retardation (Figure 32(d)) maps values of discontinuous outlier clusters (marked with green circles in Figure 32(c) and (d)) are suspected to be inaccurate. Many of these outliers show less variation after the uncertainty-based RNFL boundary optimization. Although the optimized boundary also produces a few new discontinuous clusters (marked with red circles in Figure 32(c) and (d)) in birefringence and phase retardation maps, the optimized boundary generally provides smoother RNFL birefringence and phase retardation maps.

To evaluate smoothness of RNFL birefringence and phase retardation maps quantitatively, we utilize the local standard deviation of birefringence and phase retardation as a measure for their smoothness. In RNFL birefringence and phase retardation maps, the standard deviation among each cluster and its four neighbors is calculated and plotted in the local standard deviation maps in Figure 33. For clusters in the innermost and outermost rings, the local standard deviation is calculated with respect to the cluster of interest and its three available neighbors. From Figure 33 it is clear that the local standard deviation of both RNFL birefringence and phase retardation decrease after the proposed RNFL boundary optimization. The average local standard deviations of RNFL birefringence and phase retardation calculated from intensity-based and optimized RNFL segmentation are given in Table 3. A paired t-test is computed for

pairwise comparing the local standard deviation of intensity-based and optimized segmentation results quantitatively. The null hypothesis of the paired t-test is that the mean of the paired differences in the local standard deviation calculated from intensity-based and optimized RNFL segmentation is zero. The paired t-test shows that the decrease of local standard deviation of birefringence and phase retardation are both statistically significant (p = 0.0040 for birefringence and p =3.48 × 10^{-7} for phase retardation). The results suggest that RNFL birefringence and phase retardation calculated from the optimized RNFL boundary are spatially smoother than those calculated from the intensity-based boundary. Thus, we conclude that the proposed RNFL segmentation approach provides a better estimate of RNFL birefringence and phase retardation than traditional intensity-based segmentation results.

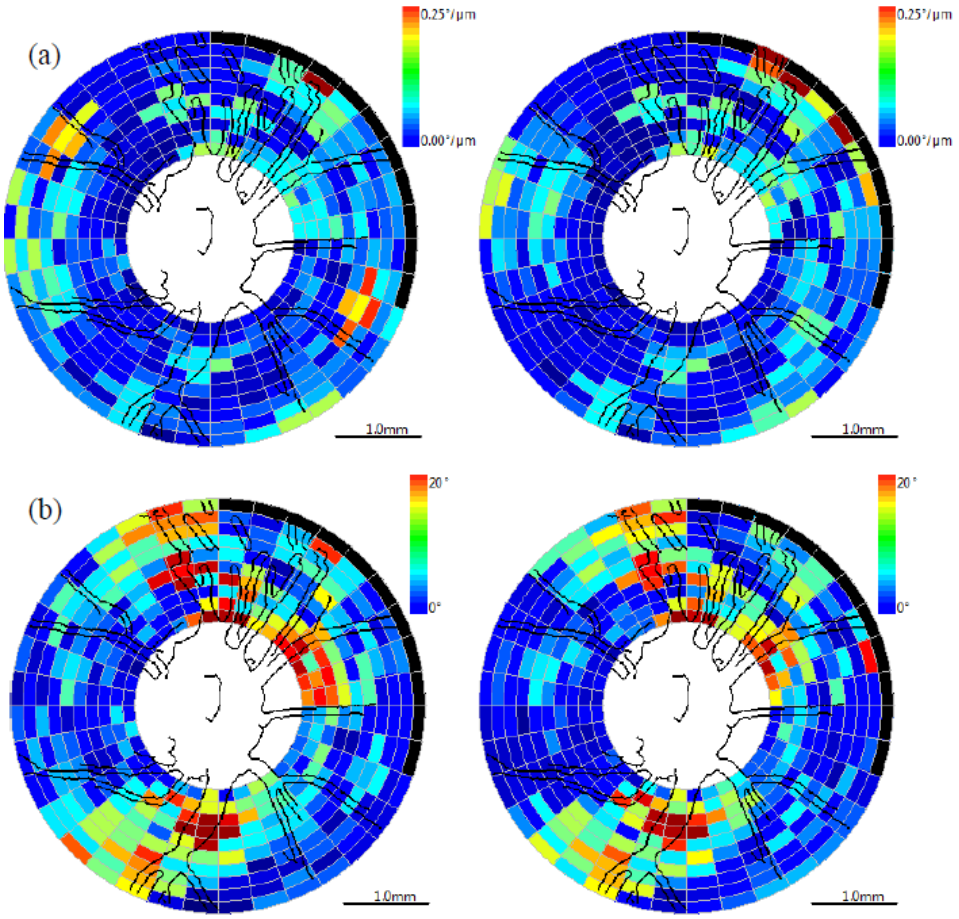

Figure 33: Local standard deviation maps created with intensity-based (left column) and optimized (right column) RNFL boundaries. Unprocessable clusters due to inappropriate operator settings during image acquisition are marked in black. (a) Birefringence. (b) Phase retardation.

	Average local standard deviation of birefringence (°/100 μm)	**Average local standard deviation of phase retardation (°)**
Intensity-based segmentation	7.54	8.37
Optimized segmentation	7.05	7.76
Paired t-test *p*-value	0.0040	3.48×10^{-7}

Table 3: Comparison of average local standard deviations of birefringence and phase retardation calculated from intensity-based and optimized RNFL segmentation.

3.4.4. Discussion

The purpose of the optimized RNFL boundary detection using polarimetric measurement is to demonstrate the usage of polarimetric information provided by PS-OCT. It is the first published study of segmenting RNFL from PS-OCT images utilizing both intensity and polarimetric information [83]. Many aspects in the current procedure can be improved to achieve better segmentation results and higher performance. For example, currently we adopt a simple approach of estimating RNFL boundary from OCT intensity images with image thresholding. Although the thresholding approach is computationally efficient, it tends to overestimate RNFL thickness as mentioned above and sometimes it misdetects RNFL boundary (especially on low quality images). The thresholding-based RNFL boundary detection algorithm should be replaced by the 3D active contour based retinal sublayer segmentation algorithm described in Chapter 2 should be introduced.

In this study, we evaluate the improvement of RNFL birefringence and phase retardation estimation by assessing their local smoothness. Although we argued this is a valid criteria with a reasonable physical assumption that RNFL birefringence and phase

retardation is spatially continuous, better approaches of assessing how the proposed algorithm improves birefringence and phase retardation estimation may be applied. For example, a low-birefringent material with known birefringence could serve as gold standard. More studies are required to further evaluate the performance of the proposed RNFL segmentation strategy.

As a conclusion, we propose a two-step RNFL segmentation method for clustered ring scan images acquired with a PS-OCT system. The RNFL segmentation method utilizes both intensity and polarimetric information to achieve optimized RNFL boundary detection for estimation of birefringence. RNFL anterior and posterior boundaries are first detected from the intensity image. RNFL birefringence is estimated from the intensity-based RNFL segmentation with a multiple-state Levenberg-Marquardt nonlinear fitting algorithm. Optimized RNFL segmentation is achieved by minimizing the Levenberg-Marquardt uncertainty of RNFL birefringence while locally adjusting the posterior RNFL boundary. The proposed RNFL segmentation approach provides an optimized RNFL segmentation with lowest achievable birefringence uncertainty, and optimizes birefringence and phase retardation measurement. Clinical results from a healthy volunteer suggest that the proposed segmentation method estimates phase retardation in the RNFL with lower uncertainty and higher continuity than traditional intensity-based approaches.

3.5. CONCLUSION OF THIS CHAPTER

In this chapter, a single-mode-fiber based swept-source polarization-sensitive OCT system for human retinal imaging is presented. A Stokes vector based polarimetric model is reviewed for estimating sample's birefringence from PS-OCT measurement. Two different scan patterns are designed for PS-OCT to overcome the effects of high

polarimetric noise. Peri-papillary RNFL thickness, birefringence, and phase retardation maps are collected from healthy eyes. Finally, as an example of PS-OCT application, a RNFL posterior boundary detection method is presented based on optimizing PS-OCT polarimetric measurements.

Chapter 4: Clinical and Animal Studies Using OCT and PS-OCT

4.1. Introduction and Motivation

Optical coherence tomography (OCT) is routinely used by ophthalmologists to record diagnostic retinal images. From OCT retinal images, a number of candidate markers for early glaucoma diagnosis have been proposed. Retinal nerve fiber layer thickness (RNFLT) has become a routine component of glaucoma screening, diagnosis and monitoring protocols as decreased RNFLT is correlated with glaucoma [84, 85]. RNFL birefringence (Δn) and phase retardation (PR) are also candidate markers for early glaucoma diagnosis, since previous studies have demonstrated the link between retinal birefringence and RNFL microtubule density [86, 87]. In addition, RNFL reflectance, which may indicate mitochondrial dysfunction [88-90] and cytoskeletal changes [91], emerges as a promising candidate marker for early-stage glaucoma diagnosis. All the above markers including RNFLT, Δn, PR, and reflectance, can be characterized using PS-OCT. A natural and important question is, what is the earliest indicator that performs best in detecting glaucoma?

To answer this question, we first introduced two parameters which represent the reflectance of RNFL: reflectance index (RI) and normalized reflectance index (NRI). Then, three linked clinical or animal studies were performed in order to compare the performance of all glaucoma indicators (Table 4). The first study was performed on non-human primates using lab-built PS-OCT [29]. The second study was performed on human at Eye Institute of Austin (EIA) and the Duke Eye Center(DEC) using both lab-built PS-OCT and commercial intensity OCT [28]. The third study was performed on human at multiple clinical centers using commercial intensity OCT as a part of Advanced Imaging for Glaucoma Study (AIGS). Multiple glaucoma indicators are recorded and compared in the three linked studies including RNFLT, Δn, PR, RI, and NRI.

	Study 1	Study 2	Study 3
Model	Non-human primates: control eyes and glaucomatous eyes	Human: normal, glaucoma-suspect, and glaucomatous groups	Human: normal and glaucoma-suspect groups
Location	University of Texas at Austin	Eye Institute of Austin (EIA) and Duke Eye Center (DEC)	Advanced Imaging for Glaucoma Study (AIGS)
Instruments used	Lab-built PS-OCT	Lab-built PS-OCT and commercial OCT	Commercial OCT
Glaucoma indicators	RNFLT, Δn, PR, and RI	RNFLT, Δn, PR, and NRI	RNFLT and NRI
Comparison made	Changes over time, and differences among groups	Differences among groups	Differences among groups

Table 4: Summary of the three studies presented in this chapter. RNFLT: retinal nerve fiber layer (RNFL) thickness. Δn: RNFL birefringence. PR: RNFL phase retardation. RI: RNFL reflectance index. NRI: RNFL normalized reflectance index.

Results of our studies involving primates and human subjects suggest that RNFL reflectance, measured by either RI or NRI, is the earliest, most sensitive and robust early diagnostic glaucoma indicator compared with RNFLT, Δn, and PR. A possible mechanism of reduced RNFL reflectance in glaucomatous retina is proposed at the end of this chapter.

4.2. RNFL REFLECTANCE MEASUREMENT

Intuitively, the term "RNFL reflectance" means the brightness or pixel intensity of RNFL that appears on an OCT retinal image. However, due to the variations in signal scaling and corneal transmission among difference OCT measurements, the brightness of RNFL must be normalized with the brightness of a common structure. Here, we propose

the average brightness of a retinal sublayer near retinal pigment epithelium (RPE) as the normalization standard.

Two retinal sublayers can be identified with either automatic or manual boundary detection techniques: RNFL, and RPEIOS, which a thin layer about the retinal pigment epithelium (RPE) and containing small volumes of the photoreceptor outer segment and superficial choroid, as shown in Figure 34. RNFL reflectance index (RI) is defined as the ratio of OCT intensities between the two detected retinal layers:

$$RI = \frac{\bar{I}_{RNFL}}{I_{RPEIOS}} \tag{29}$$

where $\bar{I}_{RNFL}$ is RNFL brightness per unit depth, and I_{RPEIOS} is the averaged brightness in the RPEIOS region.

In practice, the reference layer was taken to be 10 pixels (~75 μm) below the anterior boundary of RPE. This segmented RPE region is larger than necessary to fully capture the brightest reflecting region that is not in the RNFL in the retina. Although segmenting the anterior boundary at the Bruch's membrane is preferred, the limited axial resolution in this PS-OCT system and reliance on automated edge detection did not allow Bruch's membrane to be consistently segmented. As a compromise, a fixed thickness for the RPE region was taken.

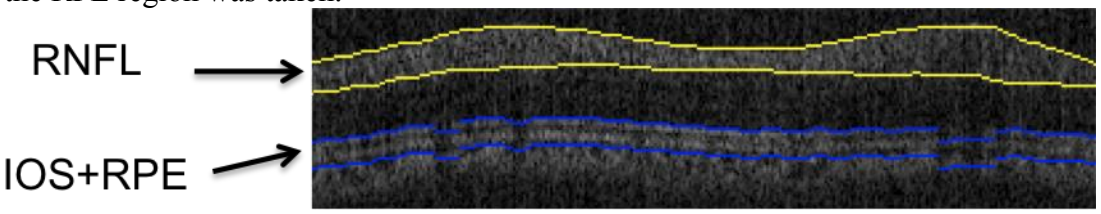

Figure 34: PS-OCT retinal B-scan image of a non-human primate retina, plotted with segmented layers to determine RI and NRI: RNFL (yellow) and RPEIOS (blue, including small volumes of inner and outer segment and superficial choroid)

Another measurement of RNFL reflectance is normalized reflectance index (NRI). NRI is defined as:

$$NRI = \frac{I_{RNFL}}{I_{RPEIOS}} \tag{30}$$

where I_{RNFL} is the total light intensity reflected from the RNFL layer, i.e. a summation of the OCT image pixel intensity in the RNFL layer.

The difference between RI and NRI is that NRI includes information from both thickness and reflectance of RNFL, while RI includes information from RNFL reflectance only. As a result, NRI can be considered as a combination feature of RNFL thickness and reflectance.

4.3. STUDY 1: NON-HUMAN PRIMATE STUDY WITH PS-OCT

Three non-human primates were included in the study. For each non-human primate subject, one eye was laser treated to increase intraocular pressure (IOP) with an established protocol [92-94], while the other eye was left untreated and served as a control. Each primate subject was followed over a period of 30 weeks and PS-OCT measurements were recorded at weekly intervals to assess RNFL changes associated with elevated IOP. Under elevated IOP, the time variation and IOP association of RNFL thickness, phase retardation, birefringence, and RI were measured and analyzed for the three non-human primates.

In the study, two scanning patterns were used during PS-OCT measurement: continuous ring scans and clustered ring scans. RNFL thickness and reflectance index (RI) are calculated from both continuous and clustered ring scans, while phase retardation and birefringence are calculated from clustered ring scans only. Figure 34 shows a typical continuous ring scan retinal image acquired by the lab-built PS-OCT.

A full presentation of the results from the non-human primate study is reported in reference [29]. Briefly, the data from three non-human primates show that RI outplays RNFL thickness, birefringence and phase retardation in detecting elevated IOP induced glaucoma. A linear mixed effects model shows that RI, calculated from both clustered and continuous ring scans, drops significantly with elevated IOP over time ($p<0.05$ for both), while the other three parameters (RNFL thickness, birefringence and phase retardation) do not exhibit significant change ($p>0.05$). An example set of retinal maps showing the values of RI in both control and treated eyes are generated for beginning (day 27), middle (day 81), and end (day 174) time points (Figure 35).

To evaluate change of RNFL parameters (thickness, phase retardation, birefringence, and RI) with respect to IOP exposure, we fit the difference between control and the treated eyes of RNFL parameters as a function of IOP damage integral using a linear mixed effects model. From the linear mixed effects model, we observed no significant trend ($p>0.05$) in the difference of RNFL thickness, phase retardation and birefringence between control and treated eyes vs. IOP damage integral. For both clustered and continuous ring scan data, difference between RI of control and treated eyes increases significantly when IOP damage integral increases ($p<0.05$ for both).

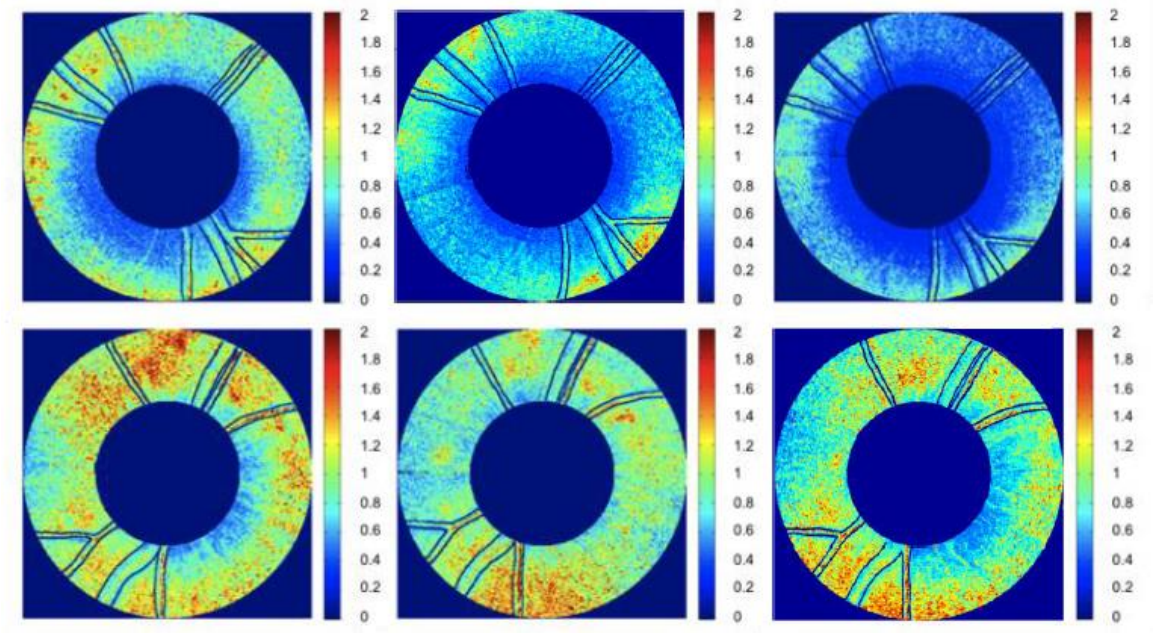

Figure 35: RNFL reflectance index (RI) maps for continuous ring scans for primate 2. Top is OD (treated eye) and bottom is OS (control eye). Time points correspond to beginning (left, day 27), middle (center, day 81), and end (right, day 174) of the study. Blood vessels indicated by black lines.

As a conclusion, with elevated IOP, a significant decrease in RNFL reflectance was observed in eyes of each of the three primate eyes induced with glaucoma, while no significant change was observed in RNFL thickness, phase retardation, or birefringence in any of the three primates. The results from the non-human primate study suggest that decreased RNFL reflectance is the earliest correlate with glaucomatous damage. RNFL thickness changes at a later time in glaucoma progression compared to RNFL reflectance. This finding is consistent with previous studies that observed a decreased RNFL thickness in glaucoma eyes [84, 95].

4.4. STUDY 2: HUMAN STUDY WITH PS-OCT AND OCT

In addition to the above study on non-human primate, a clinical study has also been performed at Eye Institute of Austin (EIA) and Duke Eye Center (DEC) to identify

the best indicator to detect early glaucoma for human. 71 human subjects presenting 75 eyes comprised of 33 controls, 24 glaucomatous, and 18 glaucoma-suspects were included in the clinical study. The definition of each group is listed in Table 5. Three glaucoma diagnosis devices are employed in the study including RTVue OCT (Optovue, CA), and two PS-OCT systems developed in our lab, respectively denoted as PS-OCT-EIA and PS-OCT-DEC. RNFL thickness (RNFLT) and normalized reflectance index (NRI) maps were measured using both PS-OCT and RTVue OCT (Optovue, CA). PR and Δn were measured using PS-OCT.

Control	**Glaucoma-Suspect**	**Glaucoma**
Has an intraocular pressure (IOP) <21mm Hg with no history of elevated IOP, normal visual fields [mean deviation and pattern SD (PSD) within 95% confidence limits and Glaucoma Hemifield Test (GHT) within normal limits], and no optic disc abnormalities judged by a glaucoma specialist (H.G.R. at Eye Institute of Austin and S.J.M. at Duke Eye Center)	Ocular hypertension: has an IOP>21mm Hg but <30mm Hg measured in at least 3 separate office visits and have normal optic nerve head appearance. Preperimetric glaucoma: has an asymmetric cup-to-disc ratio and show early glaucomatous optic disc abnormality, including thinning of the neuroretinal rim and notching	Has history of elevated IOP, 2 consecutive abnormal visual fields (PSD outside the 95% confidence limits, abnormal GHT, or any typical visual field defect), and an abnormal optic disc

Table 5: Definitions of control, glaucoma-suspect, and glaucoma groups in Study 2.

For each glaucoma indicator, average values in 7 RNFL locations (all rings, inner rings, outer rings, superior, inferior, nasal, and temporal) were calculated for further statistical comparisons (Figure 36).

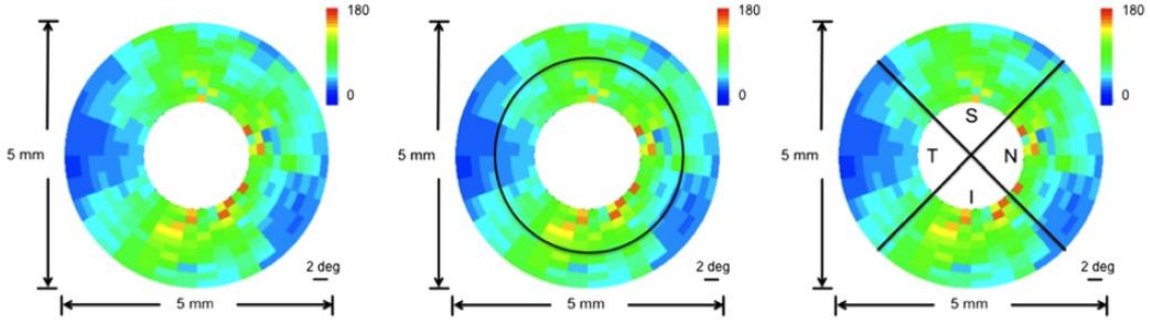

Figure 36: Definitions of analyzed retinal nerve fiber layer (RNFL) locations of Eye Institute of Austin and Duke Eye Center optical coherence tomography data sets illustrated on a clustered RNFL thickness map of a human eye (OD). Average computed across all-rings (left panel). Averages computed over 5 inner-rings (inner) and 5 outer-rings (outer) (middle panel). Averages computed over the temporal (T), superior (S), nasal (N), and inferior (I) quadrants (right panel).

The area under the Receiver Operating Characteristic (ROC) curve (AUC) was used to compare the performance of RNFLT, PR, Δn, and NRI, measured in seven retinal locations, in distinguishing between control, glaucomatous, and glaucoma-suspect eyes (Figure 37 and Figure 38). The complete statistical results have been published [28]. Briefly, for all the three devices included in the study (PS-OCT-EIA, PS-OCT-DEC, and RTVue OCT), NRI provides a larger ROC-AUC than any other glaucoma indicators, either statistically significant or not (Table 6). According to PS-OCT data, NRI works significantly better than PR and Δn to distinguish between glaucomatous and control eyes, and between glaucoma-suspect and control eyes. For RTVue OCT data, NRI performs significantly better than RNFLT to distinguish between glaucoma-suspect and control eyes. However, the performances of NRI and RNFLT for classifying glaucomatous vs. control eyes were statistically indistinguishable for all the three devices, possibly due to the limited sample size.

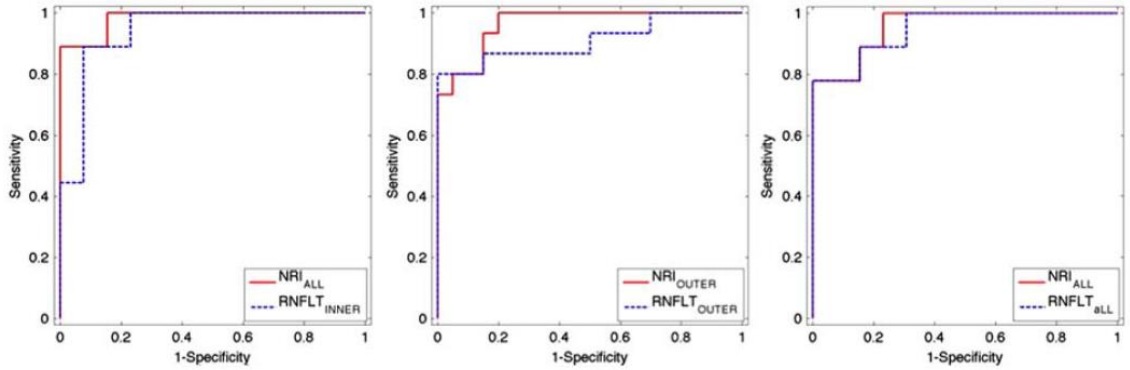

Figure 37: Receiver operating characteristics (ROC) curves suggest NRI outperforms RNFLT for distinguishing glaucomatous versus control eyes for all the three devices included in the study.
Left: ROC of all-rings average of NRI (NRI_{ALL}) and inner-rings average of RNFLT ($RNFLT_{INNER}$) for PS-OCT-EIA data set.
Middle: ROC of NRI_{OUTER} and $RNFLT_{OUTER}$ for PS-OCT-DEC data set.
Right: ROC curves of NRI_{ALL} and $RNFLT_{ALL}$ for RTVue OCT data set.

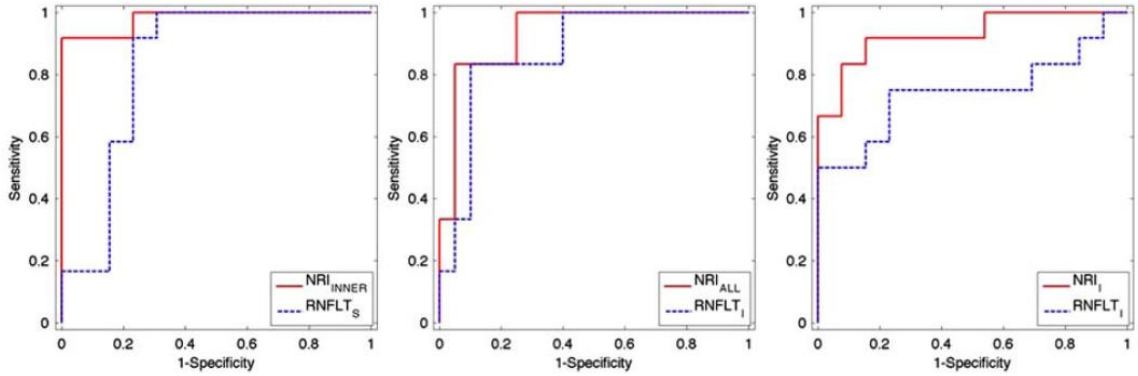

Figure 38: Receiver operating characteristics (ROC) curves suggest NRI outperforms RNFLT for distinguishing glaucoma-suspect versus control eyes for all the three devices included in the study.
Left: ROC of NRI_{INNER} and $RNFLT_s$ for PS-OCT-EIA data set.
Middle: ROC of NRI_{ALL} and $RNFLT_I$ for PS-OCT-DEC data set.
Right: ROC curves of NRI_I and $RNFLT_I$ for RTVue OCT data set.

Glaucoma Indicators	Instruments	Distinguishing between glaucomatous and control eyes	Distinguishing between glaucoma-suspect and control eyes
NRI vs. PR	PS-OCT-EIA and PS-OCT-DEC	NRI has higher AUC than PR, statistically significant	NRI has higher AUC than PR, statistically significant
NRI vs. Δn	PS-OCT-EIA and PS-OCT-DEC	NRI has higher AUC than Δn, statistically significant	NRI has higher AUC than Δn, statistically significant
NRI vs. RNFLT	PS-OCT-EIA and PS-OCT-DEC	NRI has higher AUC than RNFLT, statistically insignificant	NRI has higher AUC than RNFLT, statistically insignificant
NRI vs. RNFLT	RTVue OCT	NRI has higher AUC than RNFLT, statistically insignificant	NRI has higher AUC than RNFLT, statistically significant

Table 6: Performance comparison of glaucoma indicators in Study 2. Performance is measured by receiver operating characteristics (ROC) area under curve (AUC). NRI: normalized reflectance index. PR: phase retardation. Δn: birefringence. RNFLT: retinal nerve fiber layer thickness.

As a conclusion, RNFL reflectance, measured by NRI, may outperform RNFL thickness, phase retardation, and birefringence for distinguishing between glaucoma-suspect vs. control eyes. Although more clinical data are required to draw a conclusion, results of this pilot clinical study suggest that RNFL reflectance is a promising new quantitative measure to detect glaucoma.

4.5. STUDY 3: HUMAN STUDY WITH COMMERCIAL OCT

4.5.1. Background and Motivation

RNFL reflectance was found as a useful glaucoma indicator from both non-human primate and human studies. An attractive characteristic of RNFL reflectance measurement is that its computation is purely done on OCT images without any requirement of modifying OCT hardware. As a result, RNFL reflectance can be

computed on previously collected clinical data even before the introduction of RNFL reflectance. As a retrospective confirmation of using RNFL reflectance to detect glaucoma-suspects, another clinical study was performed as part of Advanced Imaging for Glaucoma Study (AIGS).

Advanced Imaging for Glaucoma (AIG) is a multi-center bioengineering partnership sponsored by the National Eye Institute. Current AIG clinical centers include University of Southern California, University of Miami, and University of Pittsburgh Medical Center, and Oregon Health & Science University. Advanced Imaging for Glaucoma Study (AIGS) performed in the above clinical centers utilized standardized instruments and procedures across all clinical centers. AIGS was conducted in accordance with the Declaration of Helsinki. Informed consent was obtained from all participants after discussing the goals of the study and consequences of participation. Each institutional review board approved the research protocol. Data was handled in compliance with the US Health Insurance Portability and Accountability Act (HIPAA).

4.5.2. Methods

According to AIGS protocol, paticipants are categorized into three groups: a) normal group, b) perimetric glaucoma (PG) group, and c) glaucoma suspect and pre-perimetric glaucoma (GSPPG) group. The definitions of each group are listed in Table 7. In this study, we only included data from normal and GSPPG groups. PG eyes are not included in this study.

Normal Group	All of the following inclusion criteria must be satisfied completely with both eyes for normal subjects: No history or evidence of retinal pathology or glaucoma. No history of keratorefractive surgery. Normal Humphrey SITA 24-2 visual field: a mean deviation (MD) and corrected pattern standard deviation (CPSD) within 95% confidential limits of normal reference, and glaucoma hemifield test (GHT) within normal limits (97%). Intraocular pressure (IOP) < 21 mm Hg. Central corneal pachymetry > 500 μm. No chronic ocular or systemic corticosteroid use. Open anterior chamber angle: gonioscopy must show 75% or more of the angle to be Grade 2 or wider by Shaffer's grading system. Normal-appearing optic nerve head (ONH) and nerve fiber layer (NFL): intact neuroretinal rim without splinter hemorrhages, notches, localized pallor or NFL defect. Symmetric ONH between left and right eyes: CDR difference < 0.2 in both vertical and horizontal dimensions.
Perimetric Glaucoma (PG) Group	**Inclusion Criteria:** At least one eye must fulfill the following criteria for perimetric glaucoma (PG) subjects: Glaucomatous (abnormal) visual field (VF) loss defined as a CPSD ($p < 0.05$), or GHT ($p < 1\%$) outside normal limits, in a consistent pattern on both qualifying Humphrey SITA 24-2 VF, and ONH or NFL defect visible on slit-lamp biomicroscopy or stereo color fundus photography defined as one of following: diffuse or localized thinning of the rim disc (splinter) hemorrhage notch in the rim vertical cup/disc ratio greater than the fellow eye by > 0.2 **Mixed Enrollment:** If the subject has only one eye that fulfills the eligibility criteria, that eye will be followed in the PG group and the other eye will be followed in the GSPPG group.
Glaucoma Suspect and Pre-Perimetric Glaucoma (GSPPG) Group	**Inclusion Criteria:** Glaucoma-suspect eyes must have one or more of the following risk factors or abnormalities in both eyes: Ocular hypertension is defined as any eye that has pre-treamtment IOP >22 OR has a baseline average IOP >= 22 May record pre-medication IOP. ONH or NFL defect visible on slit-lamp biomicroscopy or stereo color fundus photography as defined for the PG group. The fellow eye meeting the eligibility criteria for the PG group **Exclusion Criteria:** Glaucomatous (abnormal) VF loss as defined for the PG group.

Table 7: Definitions of normal, perimetric glaucoma (PG), and glaucoma suspect and pre-perimetric glaucoma (GSPPG) groups in Study 3.

RTVue SD-OCT (Optovue, CA) with 840 nm wavelength was used as the standard OCT instrument in AIGS. In this study, RTVue OCT images of 35 normal and 34 GSPPG eyes were randomly selected from AIGS database. For each eye, three OCT ring scans centered about the optic nerve head were collected from the left eye, but only one ring scan with highest signal strength index (SSI, which is an image quality measurement provided by RTVue OCT) is used in the statistical study. Each OCT ring scan contains 10 rings with outer diameter of 4.9 mm and inner diameter of 2.2 mm.

RNFL and RPEIOS boundaries were manually determined by four OCT experts as shown in Figure 39. Based on RNFL and RPEIOS segmentation, two glaucoma indicators – normalized reflectance index (NRI) and RNFL thickness (RNFLT) – were calculated for each patient from seven RNFL locations (all rings, inner rings, outer rings, superior, inferior, nasal, and temporal) for statistical comparison. The definitions of the seven RNFL locations are similar as those in Study 2 (Figure 36).

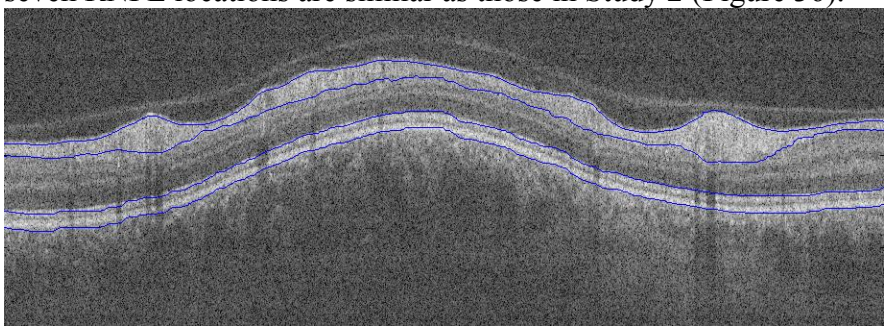

Figure 39: RTVue OCT retinal ring scan image from a normal subject. RNFL and RPEIOS layers are segmented and plotted on the OCT image.

4.5.3. Results and Discussion

4.5.3.1 Detecting Glaucoma using Single Parameter

The statistical analysis approach was similar with Study 2. First, the average and standard deviation of NRI and RNFLT in the seven RNFL locations of normal and

GSPPG groups are computed and shown in Table 8 and Table 9. Both RNFL and NRI of the normal group are significantly larger than those of the GSPPG in most RNFL locations. This result is consistent with our previous observation in Study 2 [28].

RNFL location	Average NRI of normal group	Average NRI of GSPPG group	P-value
All-rings	38.830±6.471	34.765±6.851	0.0136*
Inner-rings	45.674±8.439	39.899±7.623	0.004*
Outer-rings	31.995±5.477	29.621±6.608	0.1085
Superior	47.765±9.780	41.483±10.681	0.0131*
Inferior	50.772±11.450	44.056±11.187	0.0163*
Nasal	30.281±7.220	30.191±7.436	0.9594
Temporal	26.308±5.346	22.952±7.383	0.0337*

Table 8: The average and standard deviation of NRI in seven RNFL locations of normal and GSPPG groups. *p<0.05

RNFL location	Average RNFLT of normal group	Average RNFLT of GSPPG group	P-value
All-rings	32.653±3.2	28.911±3.863	4.16×10^{-5}*
Inner-rings	39.431±4.666	34.232±4.362	1.01×10^{-5}*
Outer-rings	25.874±3.035	23.589±3.993	0.0092*
Superior	39.917±5.347	34.664±6.295	0.0004*
Inferior	41.662±5.614	34.923±5.788	6.18×10^{-6}*
Nasal	24.448±3.744	24.463±4.976	0.9889
Temporal	24.482±3.827	21.536±5.070	0.0081*

Table 9: The average and standard deviation of RNFLT in seven RNFL locations of normal and GSPPG groups. *p<0.05

The receiver operating characteristic (ROC) curves were processed using pROC package in R statistical programming language (v2.15.10, R Foundation for Statistical Computing, Vienna, Austria) and R Studio (v0.94, RStudio Inc.) with 2000 resamples using bootstrap sampling. The area under the ROC curve (AUC) was used to pairwise compare the performance of RNFLT and NRI, measured in seven retinal locations, in

distinguishing between normal and GSPPG eyes (Figure 40). For the RTVue OCT data included in this retrospective study, the ROC-AUC provided by RNFLT and NRI are statistically indistinguishable in most RNFL locations (Table 10).

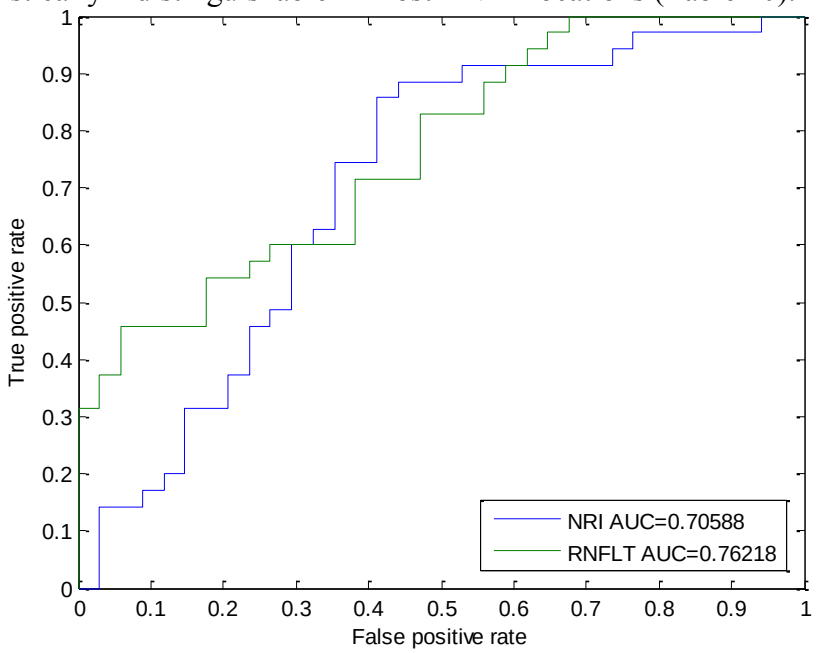

Figure 40: Receiver operating characteristics (ROC) curves of NRI and RNFLT calculated from all rings.

RNFL location	RNFLT ROC AUC	NRI ROC AUC	P-value
All-rings	0.7622 (0.6403-0.8605)	0.7059 (0.579-0.8252)	0.4054
Inner-rings	0.8193 (0.7168-0.9126)	0.7202 (0.5932-0.837)	0.1189
Outer-rings	0.6319 (0.4908-0.7538)	0.6613 (0.5227-0.7857)	0.685
Superior	0.7336 (0.6058-0.8353)	0.6933 (0.5596-0.8135)	0.343
Inferior	0.7899 (0.6773-0.8832)	0.6639 (0.5261-0.7908)	0.01632
Nasal	0.5126 (0.368-0.6513)	0.5277 (0.379-0.6613)	0.8445
Temporal	0.6664 (0.5361-0.7958)	0.6655 (0.5252-0.795)	0.9857

Table 10: Performance comparison of NRI and RNFLT in Study 3. Performance is measured by receiver operating characteristics (ROC) area under curve (AUC). The 95% confidence intervals of the AUC are listed in the parenthesis. RNFLT: retinal nerve fiber layer thickness. NRI: normalized reflectance index.

The results of this retrospective study are not fully consistent with the findings in Study 2 that NRI outperforms RNFLT. There are several possible reasons. First, the sample sizes in Study 2 and Study 3 are both small, which make it difficult to draw any conclusions from the studies. Second, the definitions of glaucoma-suspect in Study 2 and GSPPG group in Study 3 are slightly different (Table 5 and Table 7), which may introduce inconsistency in the study results. Another possible reason is that the RTVue OCT images included in Study 2 had a much lower resolution than those in Study 3 which may reduce the performance of RNFLT.

4.5.3.1 Detecting Glaucoma using Two Parameters

Although the results from this retrospective study does not confirm that RNFL reflectance performs better than RNFL thickness or not, RNFL reflectance clearly contains additional information independent from RNFL thickness. RNFL thickness and NRI are not totally correlated (correlation coefficient is 0.62). As a result, it is possible to construct a new classifier using both RNFLT and NRI and performing better than either RNFLT or NRI alone. To demonstrate this, a new classifier was trained from the AIGS data using the following logistic regression model:

$$\begin{aligned} &h_\theta(RNFLT_{ALL}, NRI_{ALL}) \\ &= g(\theta_0 + \theta_1 RNFLT_{ALL} + \theta_2 NRI_{ALL} + \theta_3 RNFLT_{ALL}^{\ 2} + \theta_4 NRI_{ALL}^{\ 2} + \theta_5 RNFLT_{ALL} \cdot NRI_{ALL}) \end{aligned} \tag{31}$$

where g is the logistic function:

$$g(z) = \frac{1}{1+e^{-z}} \tag{32}$$

The logistic classifier uses two parameters: $RNFLT_{All}$ and NRI_{All}. Comparing with the corresponding single-parameter classifiers using either $RNFLT_{All}$ or NRI_{All}, the ROC AUC is much improved (Figure 41 and Table 11).

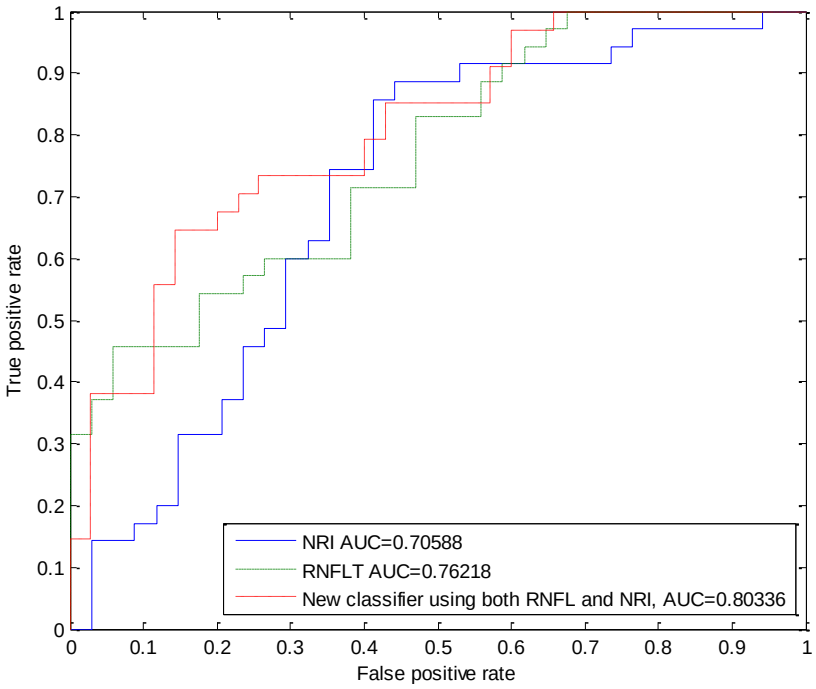

Figure 41: Receiver operating characteristics (ROC) curves of NRI_{ALL}, $RNFLT_{ALL}$, and the new classifier $h_\theta(RNFLT_{ALL}, NRI_{ALL})$ calculated from all rings.

$RNFLT_{All}$ ROC AUC	**NRI_{All} ROC AUC**	$h_\theta(RNFLT_{ALL}, NRI_{ALL})$ **ROC AUC**
0.7622 (0.6403-0.8605)	0.7059 (0.579-0.8252)	0.8034 (0.6975-0.8975)

Table 11: Performance comparison of NRI, RNFLT, and the new classifier $h_\theta(RNFLT_{ALL}, NRI_{ALL})$ in Study 3. Performance is measured by receiver operating characteristics (ROC) area under curve (AUC). The 95% confidence intervals of the AUC are listed in the parenthesis. $RNFLT_{All}$: retinal nerve fiber layer thickness calculated from all rings. NRI_{All}: normalized reflectance index calculated from all rings.

4.5.4. Summary

As a conclusion, RNFL reflectance, measured by NRI, did not show statistically significant advantage over RNFL thickness for distinguishing between glaucoma-suspect vs. normal eyes, according to the data included in this study. However, RNFL

reflectance measured by NRI contains additional information besides RNFL thickness for detecting glaucoma-suspects. The results of this pilot clinical study suggest that RNFL reflectance is a useful quantitative measure which introduces additional diagnostic power for detecting glaucoma.

4.6. POSSIBLE MECHANISM OF REDUCED NRI IN GLAUCOMATOUS EYES

The previous clinical and animal studies suggest that RNFL reflectance decreases during the early stage glaucoma progression. Although additional investigation is necessary to test candidate mechanisms for RNFL reflectance decrease, changes in the mitochondrial networks and axonal cytoskeleton changes are hypothetical mechanisms.

Previous studies have demonstrated that changes in mitochondrial membrane permeability in response to elevated IOP precede retinal ganglion cell loss in glaucomatous eyes [90, 96]. Mitochondrial dysfunction is recognized as an important component in the etiology of many neurodegenerative pathologies including amyotrophic lateral sclerosis, Alzheimer's, and Parkinson's disease. Mitochondria are recognized as dynamic organelles that constantly undergo fusion and fission processes that are required to maintain normal function of the host cell. Fusion of mitochondria to form interconnected intracellular networks is believed to be a necessary component to maintain a mitochondrial population with a full complement of gene products that can mitigate age-related degeneration. In fact, autosomal dominant optic atrophy, the leading cause of childhood blindness, is caused by a mutation in the mitochondrial fusion gene OPA1 [97]. Recently, Ju et al. demonstrated that mitochondria fission in differentiated retinal ganglion cell cultures is induced in response to elevated hydrostatic pressures [98].

Inasmuch as mitochondrial changes are an important component of neurodegenerative diseases, their potential contribution to RNFL reflectance changes is

of interest. Mitochondria have long been recognized as an important structural component impacting the light scattering properties of tissues and cells [99, 100]. Tissue scattering is greatest in structures with cells containing dense mitochondrial populations [101]. Because of the disruption of the mitochondrial fusion/fission cycle, cells undergoing apoptosis triggers changes in optical scattering properties. A number of recent studies have observed optical scattering changes in cells undergoing apoptosis that originate at least in part to the mitochondria. Pasternack et al. used a Fourier microscopy approach to demonstrate that early cell apoptosis is accompanied by mitochondrial fission and fragmentation that results in more isotropic or large-angle light scattering [102]. Chalut et al. utilized angle-resolved optical coherence tomography (OCT) to document similar scattering changes that the authors suggested may involve mitochondrial fission [103]. A number of investigators have recently applied OCT to document light scattering changes in cells undergoing apoptosis or necrosis [104, 105].

As mentioned in Section 1.2.1, RNFL is composed of RGC axons, which are rich in mitochondrial population. In normal RGC axons, mitochondria form networks in a fusion state to maintain their functionality (Figure 42(a)). In RGC axons undergoing apoptosis, mitochondria cannot maintain mitochondrial network and breaks apart into the fission state (Figure 42(b)). Due to the change of mitochondrial network morphology, RNFL backscatters incident OCT light at a wider backscattering angle in glaucomatous RNFL. As a result, less light is collected within the OCT collecting aperture, and glaucomatous RNFL appears less bright in OCT images.

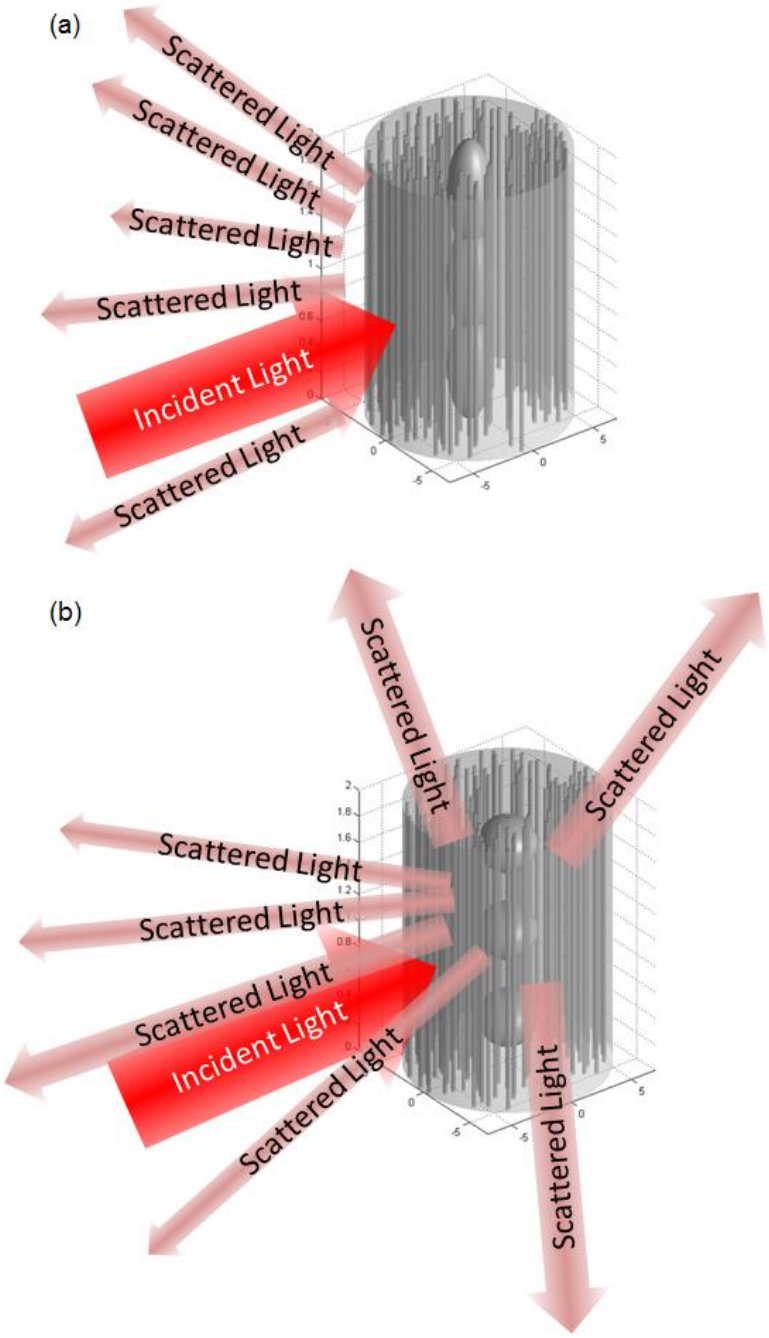

Figure 42: RGC axons containing mitochondria (ellipsoids) and microtubules (small cylinders) interact with incident light with different scattering properties. (a) In normal RGC axons, mitochondria stay in fusion state and scatter light in a narrow backscattering angle. (b) In RGC axons undergoing apoptosis, mitochondria switch to fission state and scatter light in a wider backscattering angle.

Although the decrease in reflectance in glaucomatous primate eyes reported here is consistent with reduced collected backscatter due to intensified mitochondrial fission resulting in increased large angle scattering, other mechanisms such as changes in the axonal membrane or microtubules may also contribute to the observed decrease in RNFL reflectance. Additional studies are required to isolate and better characterize the various candidate cellular processes that may contribute to decreased RNFL reflectance observed in animal and human studies.

4.7. CONCLUSION OF THIS CHAPTER

In this chapter, the results of three linked clinical and animal studies are briefly overviewed. The purpose of the three studies is to search for the earliest, most sensitive and robust glaucoma indicator, among a group of candidate glaucoma indicators including RNFL thickness, birefringence, phase retardation, and reflectance. In the first study involving non-human primates, decreased RNFL reflectance was found the earliest change associated with elevated intraocular pressure (IOP) in glaucomatous eyes. In the second study with human eyes, the performances of multiple glaucoma diagnostic indicators were compared and RNFL reflectance was identified as the best indicator to distinguish between control and glaucoma eyes, and control and glaucoma-suspect eyes. The observation that RNFL reflectance is the best glaucoma indicator is further supported in the third study with human eyes.

As a conclusion, RNFL reflectance, measured by either RI or NRI, performs better than RNFLT, Δn, and PR in terms of detecting early-stage glaucoma. The fission-fusion change of mitochondrial network morphology in RGC axons is considered as a hypothesis mechanism of RNFL reflectance change in associate with glaucomatous damage.

Although the birefringence and phase retardation information provided by PS-OCT turns out to be less effective than RNFL reflectance in glaucoma detection, PS-OCT still provide useful diagnostic values. A recent PS-OCT study utilized the degradation in the degree of polarization (DOP) of light backscattered from human RNFL with increasing depth, and showed that DOP degradation measured by PS-OCT may be another useful diagnostic tool for various eye diseases including glaucoma [106]. Additional investigates are needed on how to make the best use of PS-OCT in retinal diagnosis.

Chapter 5: Pathlength-Multiplexed Scattering-Angle-Diverse Optical Coherence Tomography (PM-SAD-OCT)

5.1. Introduction and Motivation

The clinical and animal studies in Chapter 4 have discovered the decreased RNFL reflectance to be a sensitive, robust and early diagnostic for glaucoma. The decreased RNFL reflectance prior to decreased thickness in glaucomatous retinas have been independently observed by another group as well [107]. The decreased RNFL reflectance in glaucomatous eyes suggests that certain changes of RNFL optical scattering properties happen during glaucoma progression.

As mentioned in Section 4.6, changes of optical scattering properties in cells undergoing apoptosis, largely due to intensified mitochondrial fission, have been observed in a number of studies [98, 102, 103]. The observed structural changes in mitochondrial networks associated with some neurological diseases suggest that angular scattering properties of RNFL may provide diagnostic information for retinal diseases like glaucoma.

Pyhtila and Wax first reported the application of an angle-resolved spectral domain OCT system to characterize the size of Mie scattering centers [108, 109]. Iftimia, Bouma and Tearney reported a time-domain OCT system using pathlength-encoded angular compounding for speckle reduction [110]. Later, various angle-resolved OCT designs have been reported for speckle reduction [111-113], light-scattering spectroscopy [114], focus extension [115], and measurement of absolute flow velocities [116-119]. Especially, Klein et al. acquired angle-resolved OCT images from human retina for speckle reduction purpose and mentioned the possibility of using angle-resolved OCT to achieve tissue discrimination [113]. However, there is no previous report of using an angle-diverse OCT system to measure RNFL angular scattering properties.

In this Chapter, a low resolution pathlength-multiplexed scattering-angle-diverse OCT (PM-SAD-OCT) is constructed to investigate the scattering properties of retinal nerve fiber layer (RNFL). Three types of PM-SAD-OCT studies are performed to demonstrate the application of PM-SAD-OCT (Table 12). In the first study, PM-SAD-OCT retinal images are acquired from healthy human subjects, showing the variation of RNFL scattering properties at retinal locations around the optic nerve head. In the second study, PM-SAD-OCT images are collected from an ex-vivo rat retina model, showing the longitudinal variation of RNFL scattering properties during the death of rat retina.

The third study goes beyond the scope of retinal imaging. Since the purpose of PM-SAD-OCT is to detect cell apoptosis, its application extends beyond glaucoma diagnosis. The optical scattering information provided by PM-SAD-OCT is expected to help in the early detection of any neurodegenerative diseases. In order to explore the application of PM-SAD-OCT in general neurodegenerative diseases, in the third study, PM-SAD-OCT images were collected from the nerve cord of earthworms during neuronal apoptosis.

	Study 1	**Study 2**	**Study 3**
Model	*In vivo* healthy human retina	*Ex vivo* rat retina	*In vitro* earthworm nerve cord
Instruments used	Lab-built 1060 nm PM-SAD-OCT	Lab-built 1300 nm PM-SAD-OCT	Lab-built 1300 nm PM-SAD-OCT
Comparison made	Spatial variation	Changes over time	Changes over time

Table 12: Summary of the three studies presented in this chapter.

5.2. INSTRUMENTATION

The PM-SAD-OCT imaging system is based on the swept-source ophthalmologic PS-OCT imaging system described in Chapter 3 [58]. However, for the studies in this chapter, the polarization controller is removed from the previous PS-OCT in order to reduce power loss, so that the OCT system is no longer polarization-sensitive. Figure 43 shows the schematics of PM-SAD-OCT.

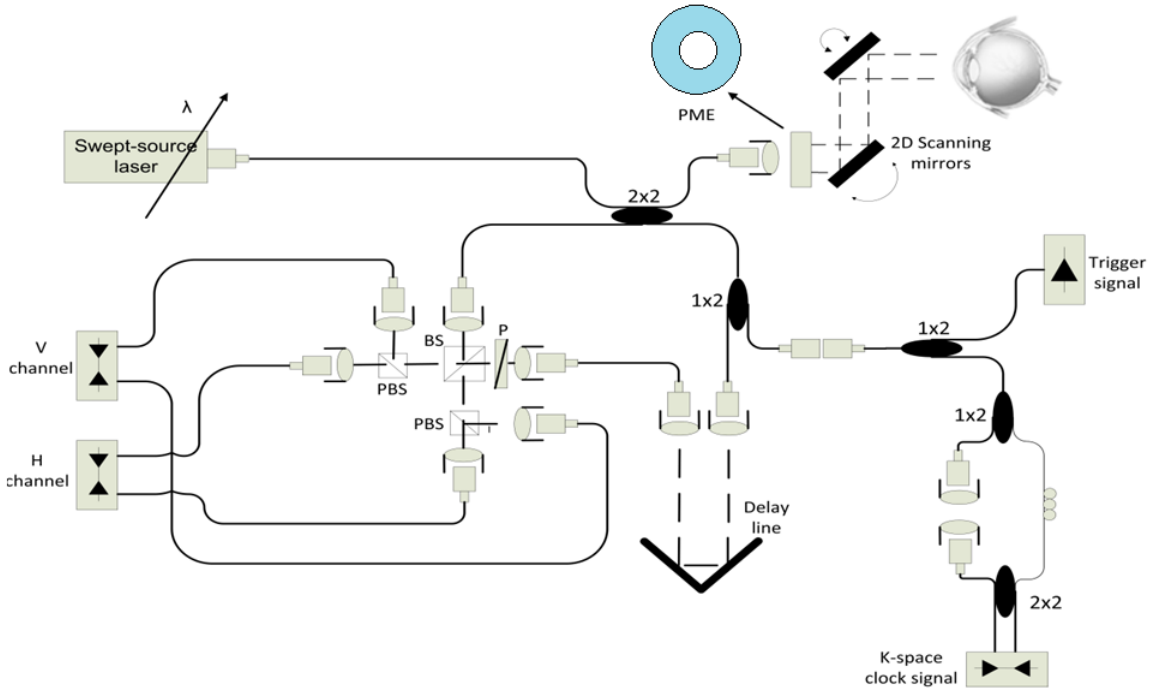

Figure 43: PM-SAD-OCT instrumentation.

PM-SAD-OCT uses pathlength multiplexing to separate incident and backscattered light from the retina into discrete angular ranges by placing a pathlength multiplexing element (PME) in the sample path of the interferometer between collimating lens and scanning mirrors close to the conjugate position of the patient's pupil. The PME is constructed of a t = 3.0mm thick BK7 glass window with a 2.0mm diameter clear aperture in the center (Figure 44). Light propagating through the central region of the

PME (Region-1) has a short path with an optical thickness, $n_{air}t$ = 3.0mm, where n_{air} = 1 is the refractive index of air. Light propagating through the outer region (Region-2) has a long path and consists of a BK7 glass annular aperture with optical thickness, $n_{glass}t$ = 4.52mm, where n_{glass} = 1.50669 is the refractive index of BK7 glass at λ = 1060nm.

The composite optical pathlength of detected light returned from the RNFL is dependent on position of incoming or returning light in the patient's pupil and is associated with angle of light incident to or backscattered from the RNFL. Diameter of the central clear aperture (2.0mm) is smaller than the $1/e^2$ diameter (6.0mm) of the sample beam. Optical pathlengths of four incident-backscattered light paths through the PME are recognized (Figure 45): 1) *short-short* – light incident on the patient's pupil propagates through Region-1 (low angle), backscatters from the RNFL at a low angle and returns through Region-1 with a relative composite pathlength of $2n_{air}t$; 2) *short-long* – light propagates through Region-1 (low angle), backscatters at a high angle from the RNFL and returns through Region-2 with a relative composite pathlength of $n_{air}t + n_{glass}t$; 3) *long-short* –light propagates through Region-2 (high angle), backscatters at a low angle from the RNFL and returns through Region-1 with a relative composite pathlength of $n_{glass}t + n_{air}t$; 4) *long-long* – light propagates through Region-2 (high angle), backscatters from the RNFL and returns through Region-2 with a relative composite pathlength of $2n_{glass}t$. Optical pathlengths of *short-long* and *long-short* paths are degenerate. As a result, PM-SAD-OCT data consists of *three* retinal subimages (Figure 46, Table 13) separated by $(n_{glass} - n_{air})t$ = 1.52007mm.

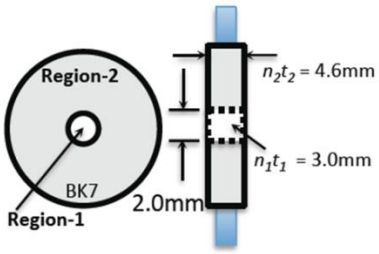

Figure 44: PME constructed of 3.0mm thick BK7 glass window. Region-1 is inner 2.0mm diameter aperture; Region-2 is outer annulus. Left: end-on view; Right: side view.

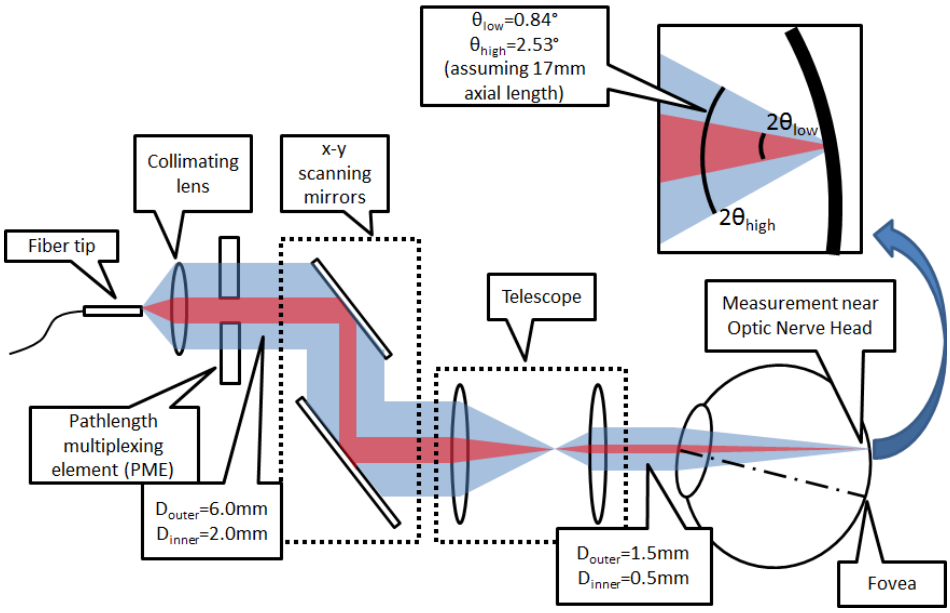

Figure 45: PME is positioned at a plane conjugate to the patient's pupil. Low-angle (short-short, red) and high-angle (long-long, blue) backscattered RNFL light paths.

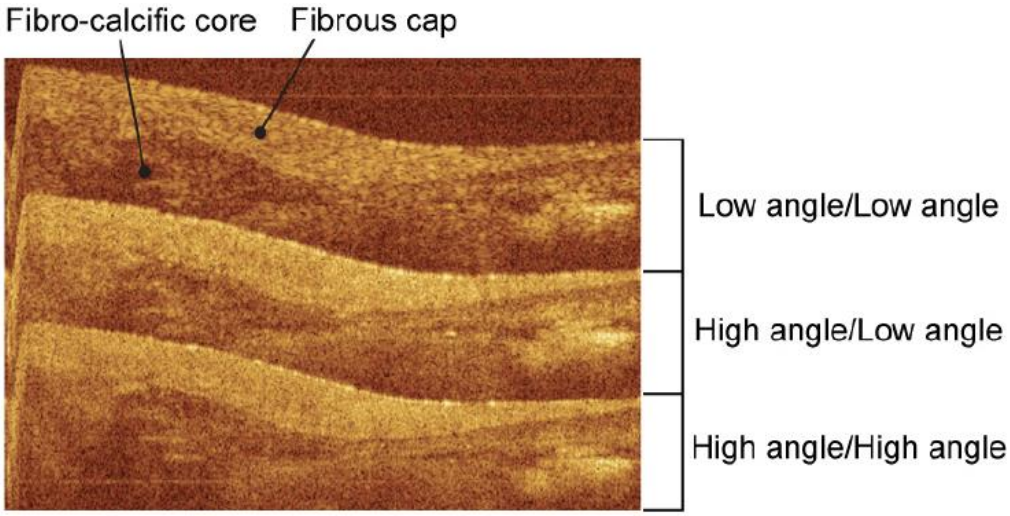

Figure 46: PM-SAD-OCT image of a coronary artery sample. Three subimages correspond to low-angle (upper), high/low angle (middle) and high angle (lower) images.

	Incident-collected path	**Relative composite pathlength**	**Incident-scattered angle**	**Possible scattering angle range**	**Averaged scattering angle**
Upper subimage	Short-short	$2n_{air}t$	Low-low	$[0, 2\theta_{low}]$	Low
Middle subimage	Short-long or Long-short	$n_{air}t + n_{glass}t$	Low-high or High-low	$[0, \theta_{low}+\theta_{high}]$	Higher
Lower subimage	Long-long	$2n_{glass}t$	High-high	$[0, 2\theta_{high}]$	Highest

Table 13: Properties of three PM-SAD-OCT subimages

The amplitude of PM-SAD-OCT signal, or pixel brightness in PM-SAD-OCT subimages, is proportional to the square root of scattered light intensity collected from the sample ($\sqrt{I_s}$). However, pixel brightness in PM-SAD-OCT images is also affected by decay of the swept-source coherence function $\Gamma(n_g c\tau)$ with increasing scan depth ($n_g c\tau$) where n_g is the group refractive index of the retina, c is the speed of light in vacuum and τ is the round-trip time delay between light in sample and reference paths. As a result, the

PM-SAD-OCT subimage with longer optical pathlength has a decreased brightness since the amplitude of OCT point spread function decreases with increasing depth. To determine the relative angular distribution of RNFL backscattered light in PM-SAD-OCT subimages, PM-SAD-OCT subimages are normalized by the experimentally measured depth-dependent amplitude of the OCT autocorrelation function.

Based on PM-SAD-OCT images, a new parameter, low-to-high angle backscattering anisotropy, is defined to examine sample's scattering properties:

$$\text{low-to-high angle backscattering anisotropy} \equiv I_{Low} / I_{High} \tag{33}$$

where I_{Low} and I_{High} are respectively the average brightness (i.e. pixel intensity) of the sample in the low-angle and high-angle subimages, For simplicity, low-to-high angle backscattering anisotropy is written as I_{Low}/I_{High}. I_{Low}/I_{High} measures the intensity ratio of low-angle and high-angle backscattering at a particular voxel location and hence gives some information about the relative backscattering properties of the sample at that location.

I_{Low}/I_{High} measurement is found to be dependent on the relative angle between incident light and sample surface normal. In order to study the effect of sample tilt angle on I_{Low}/I_{High} value, a RNFL phantom was positioned under the PM-SAD-OCT beam and tilted by an angle θ under the PM-SAD-OCT beam from a nearly normal orientation to 23 degrees. The RNFL phantom is chosen as a 70μm thick polymer covering a commercial infrared viewing card. It has been proven to be an excellent RNFL phantom because it has similar thickness, scattering properties, and birefringence to the RNFL [58, 81]. A point measurement of light returning from the phantom without scanning was recorded and I_{Low}/I_{High} was calculated at each tilt angle (Figure 47(a)).

The results suggest that the I_{Low}/I_{High} ratio varies differently in three distinct angular ranges (Figure 47(b)). In a first angular range (0-3 degrees) the I_{Low}/I_{High} ratio

decreases. In a second angular range (3-9 degrees) the I_{Low}/I_{High} ratio increases to a maximum. Finally in a third angular range (greater than 9 degrees) the I_{Low}/I_{High} ratio decreases monotonically. A possible explanation on sample tilt dependency of I_{Low}/I_{High} is that the specular reflection from the phantom dominates over the backscattering component in the first and second angular range, while backscattering is the only component in the third angular range. In the first angular range, the I_{Low}/I_{High} ratio decreases as the specular reflection component of low angle incident light is coupled into the high angle path. In the second angular range, the ratio I_{Low}/I_{High} starts increasing as the specular reflection component from high angle incident light starts being decoupled from the high angle path. In the third angular range, the ratio I_{Low}/I_{High} decreases monotonically since all collected light is backscattered rather than specularly reflected. The results suggest that the I_{Low}/I_{High} ratio is impacted in the first and second angular regions by specular reflection, and then decrease monotonically with tilt angle in the third angular region. To avoid the impact from specular reflection, sample should be sufficiently tilted so that the working angular range of PM-SAD-OCT is within the third angular range.

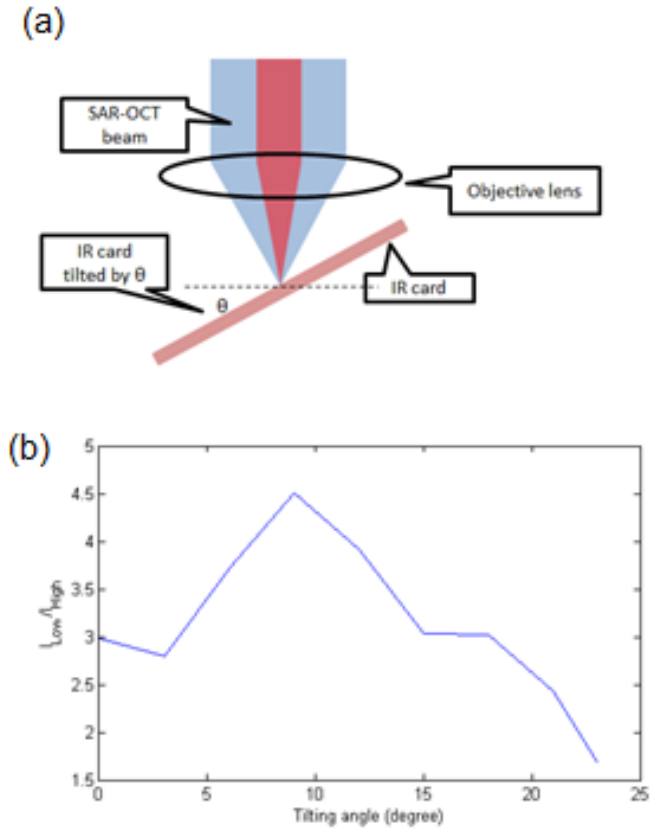

Figure 47: RNFL phantom study to investigate the effect of sample tilt.
(a) The RNFL phantom is tilted under the PM-SAD-OCT beam.
(b) I_{Low}/I_{High} vs. tilt angle.

5.3. STUDY 1: *IN VIVO* PM-SAD-OCT MEASUREMENT ON HEALTHY HUMAN RETINA

5.3.1. Methods and Results

To demonstrate feasibility of PM-SAD-OCT to measure spatial variation of the RNFL backscattering properties, retinal ring scans were collected in a dimly-lit room from five healthy subjects' right eyes (age between 24-30) without pharmacological dilation. Three PM-SAD-OCT retinal subimages are observed as expected (Figure 48).

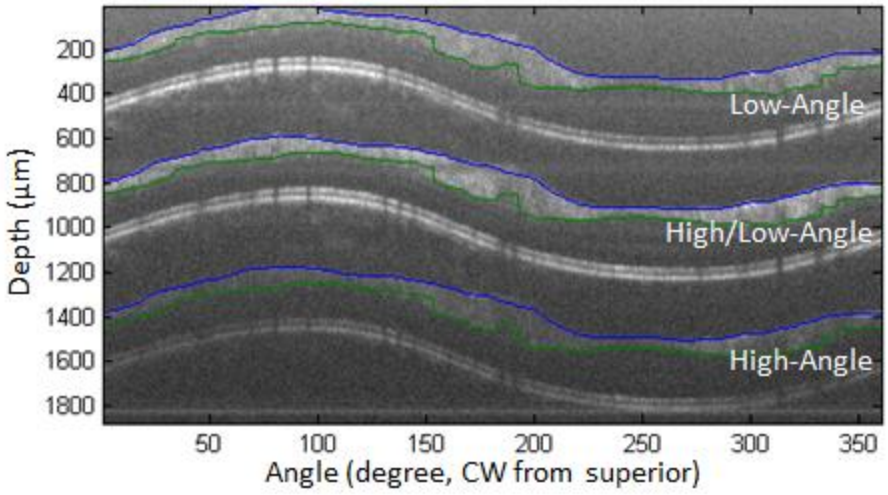

Figure 48: PM-SAD-OCT retinal subimages of a healthy human subject correspond to low-angle (upper), high/low angle (middle) and high angle (lower) images collected from to a 4.4 mm diameter ring scan. Segmentation of RNFL in each subimage is indicated by blue and green lines.

To study the peri-papillary variation of RNFL scattering properties, a retinal scan with ten peri-papillary ring-scans centered on the optic nerve head (ONH) with diameters ranging between 1.25–4.44 mm was performed. After correcting for the depth-dependent OCT autocorrelation function and segmenting RNFL from each subimage, I_{Low}/I_{High} was computed in the RNFL for each of the ten peri-papillary ring scans and plotted over the retinal area imaged (Figure 49).

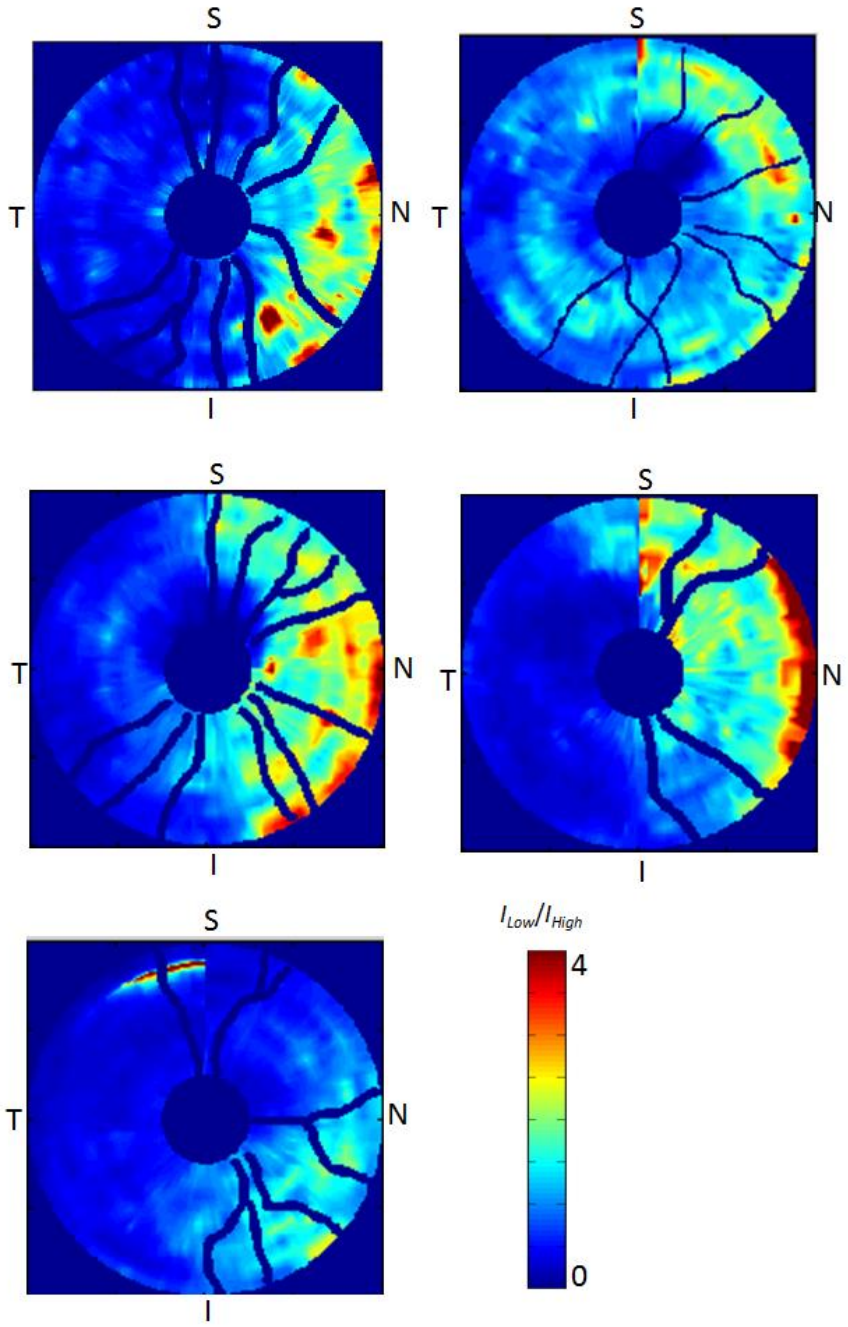

Figure 49: Retinal maps of low-to-high angle RNFL backscattering anisotropy (I_{Low}/I_{High}) from five healthy subjects by recording ten peri-papillary ring-scans centered on the ONH with diameters ranging between 1.25–4.44 mm. Blood vessels are shown with dark blue lines.

I_{Low}/I_{High} was averaged over the ten ring scans to give the peri-papillary variation around ONH (Figure 50). For all 5 subjects, I_{Low}/I_{High} is smallest (largest) in the temporal (nasal) quadrant. PM-SAD-OCT results suggest that for all the 5 healthy human subjects, RGC axonal scattering structures (e.g., microtubules, cell membranes and mitochondria networks) in the temporal (nasal) quadrant backscatter incident light at relatively larger (smaller) angles compared to those structures in the superior and inferior quadrants.

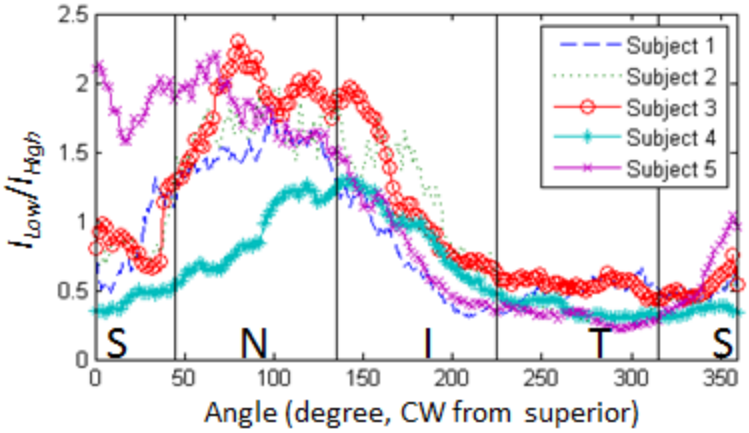

Figure 50: Peri-papillary variation of averaged I_{Low}/I_{High} of five healthy subjects.

RGC axons in normal human subjects are known to have smallest diameter in the temporal quadrant [120], so that angle of RNFL backscattered light in this region is expected to be larger and is consistent with I_{Low}/I_{High} determined from PM-SAD-OCT. Moreover, I_{Low}/I_{High} shows a similar trend with relative axoplasmic area, defined as the difference between axon area and the total organelle area for each RGC axon, around ONH measured from primate eyes [121] (Figure 51).

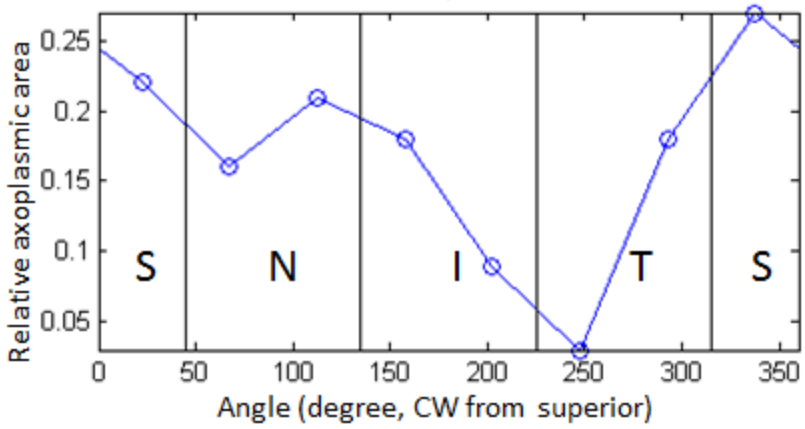

Figure 51: Peri-papillary variation of averaged relative axoplasmic mode around ONH measured from a non-human primate's eye.

5.3.2. Discussion and Summary

Since the ring scan around ONH is an off-axis measurement (as shown in Figure 45), for the largest radius (2.22 mm) retinal scan about the ONH, the angle between incident light and RNFL normal varies from about 7° (temporal quadrant) to 22° (nasal quadrant). Considering that the numerical aperture angle of the OCT beam incident on the RNFL is less than 2.53°, the angle between incident light and RNFL normal in the above measurement is more than 3× greater than the numerical aperture angle at all retinal positions. According to results from the RNFL phantom study, variation of the angle between incident light and RNFL normal is expected to increase the value of I_{Low}/I_{High} in the temporal quadrant and decrease I_{Low}/I_{High} in the nasal quadrant. However, the measured I_{Low}/I_{High} was lowest in the temporal and highest in the nasal quadrant. Therefore we think the observed variation in the ratio I_{Low}/I_{High} is due at least in part to structural variation of the RNFL. If the angular scattering properties of the RNFL phantom are substantially different from those of the nerve fibers, then the angle of the nerve fiber layer with respect to the incident light could impact the measurements.

I_{Low}/I_{High} is calculated based on OCT image intensity, which is affected by speckle noise. Thicker RNFL provides more image pixels to average and calculate I_{Low} and I_{High}, and as a result gives a more accurate calculation of I_{Low}/I_{High} in terms of signal-to-noise-ratio. To minimize the accuracy problems from speckle noise, we averaged 40 B-scans at the same location at each of the 10 rings around ONH. By performing sufficient averaging, the noise level is fairly low so that RNFL thickness does not affect accuracy of I_{Low}/I_{High}. On the other hand, thicker RNFL introduces more scattering events and can broaden backscattering angular distribution, potentially making the calculation of I_{Low}/I_{High} less reliable in terms of representing tissue scattering properties.

In summary, low resolution PM-SAD-OCT images from healthy human retinas suggest that for the recorded scans, RGC axonal structures in the temporal (nasal) quadrant backscatter light at larger (smaller) angles compared to superior and inferior quadrants. The results are consistent with known RGC neural anatomy and principles of light scattering. The results suggest that PM-SAD-OCT approaches can provide additional information on the scattering properties of the RNFL and may be useful for detection of cellular level morphology.

5.4. STUDY 2: *EX VIVO* PM-SAD-OCT MEASUREMENT ON RAT RETINA DURING RETINAL DEGENERATION

5.4.1. Introduction

A longitudinal study on ex vivo rat retina using PM-SAD-OCT is presented in this section. The purpose of this study is to demonstrate the application of scattering measurement using PM-SAD-OCT during the apoptosis of retina. In this study, rat retina were dissected and imaged using PM-SAD-OCT over a 150-minute time period. During the measurement period, the retina is considered undergoing retinal degeneration due to

the lack of oxygen and blood supply. From PM-SAD-OCT images, RNFL normalized reflectance index (NRI) as well as low-to-high angle backscattering anisotropy (I_{Low}/I_{High}) were computed at each time point.

5.4.2. Methods

15 rat eyes are included in this study. Rat eyes were dissected immediately after the sacrifice of rats. The dissection of rat eye is explained in Figure 52 and Figure 53. Basically, the optic nerve, cornea, iris and lens were removed in the first step. Then, two different protocols were developed for further dissection, respectively named Sandstone Protocol and Coverslip Protocol. Eleven rat eyes were dissected following Sandstone Protocol (Figure 52): the remaining choroid with retina was placed in a sample holder made with sandstone and immersed in saline, so that the sample inside the sandstone holder remained hydrated throughout the 150-minute measurement period. Four rat eyes were dissected following Coverslip Protocol (Figure 53): four incisions were made on the remaining choroid with retina, so that the choroid could be laid flat in a plastic Petri dish. Then, the sample was covered with a coverslip and immersed in saline throughout the measurement. The Coverslip Protocol was developed first. The Coverslip Protocol keeps the retina hydrated much longer than Sandstone Protocol, but it requires additional incisions which may cause retinal detachment, plus the weight of the coverslip may affect the physiology of the retina. Due to the potential problems with the Coverslip Protocol, we switched to the Sandstone Protocol for most rat experiments.

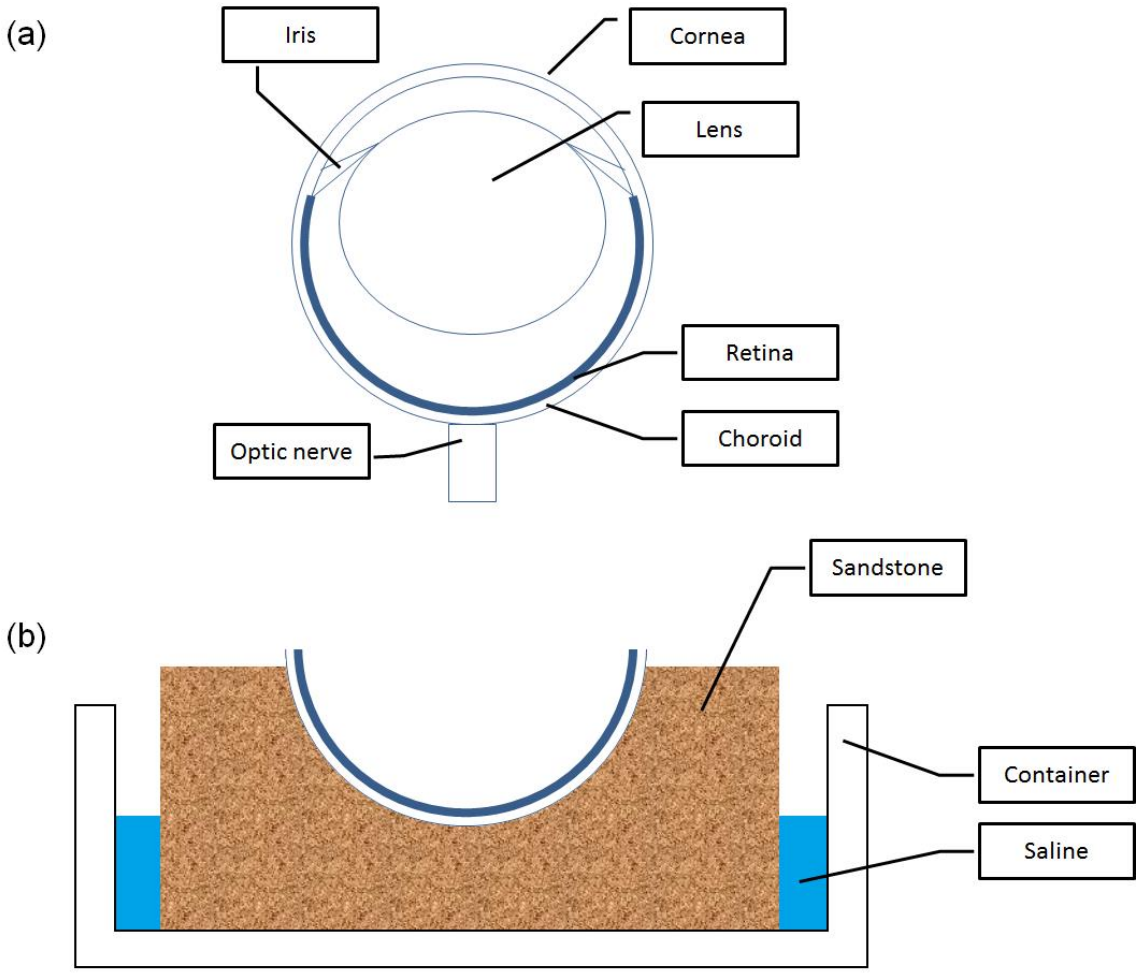

Figure 52: Dissection of a rat eye with Sandstone Protocol. (a) The structure of rat eye before dissection. (b) After dissection, optic nerve, cornea, iris and lens are removed, and the remaining choroid with retina is placed in a sandstone holder. The sandstone is immersed in saline to keep the sample hydrated.

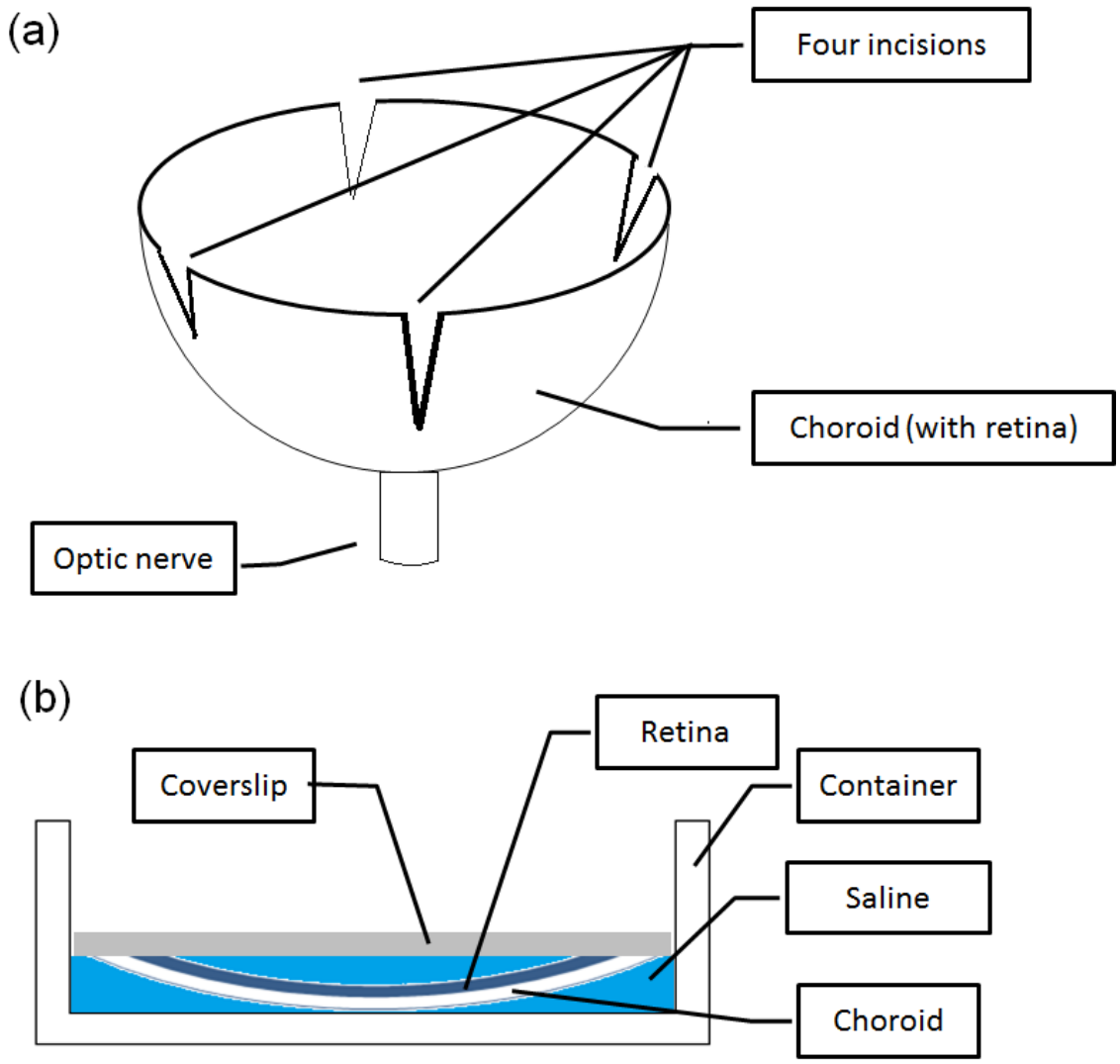

Figure 53: Dissection of a rat eye with Coverslip Protocol. (a) After removing cornea, iris, and lens, four incisions are made on the choroid so that the choroid may be laid flat. (b) The remaining choroid with retina is placed in a plastic Petri dish and covered with a coverslip. The sample is immersed in saline to keep hydrated.

PM-SAD-OCT images are acquired from the 15 rat eyes for 150 minutes after dissection, using a 1300 nm PM-SAD-OCT system. Figure 54 shows a PM-SAD-OCT B-scan image of a rat eye. Boundaries of RNFL and RPEIOS are manually determined. Three subimages are identified from PM-SAD-OCT images. As discussed in Section 5.2,

the three subimages correspond to different scattering angle ranges. As a result, the en-face images reconstructed from the three subimages show dramatic difference in terms of resolutions (Figure 55).

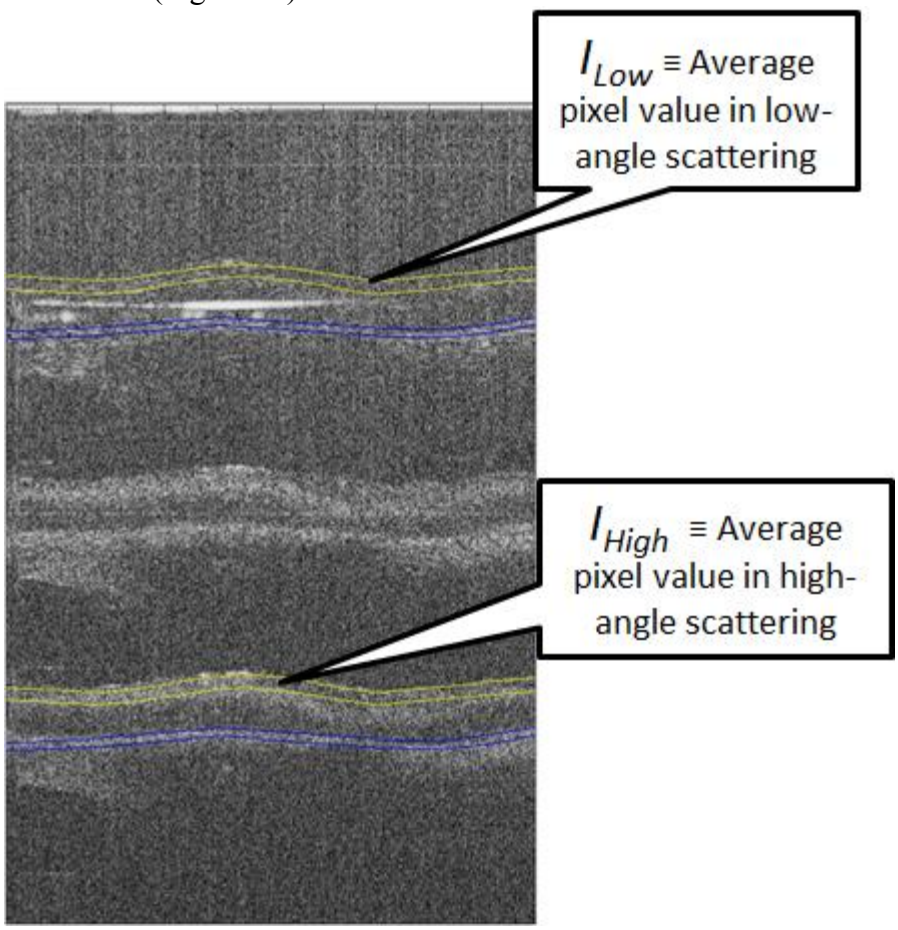

Figure 54: PM-SAD-OCT B-scan image of a rat eye. The boundaries of RNFL and RPEIOS are plotted. RNFL in the upper and lower subimages are the regions of interest.

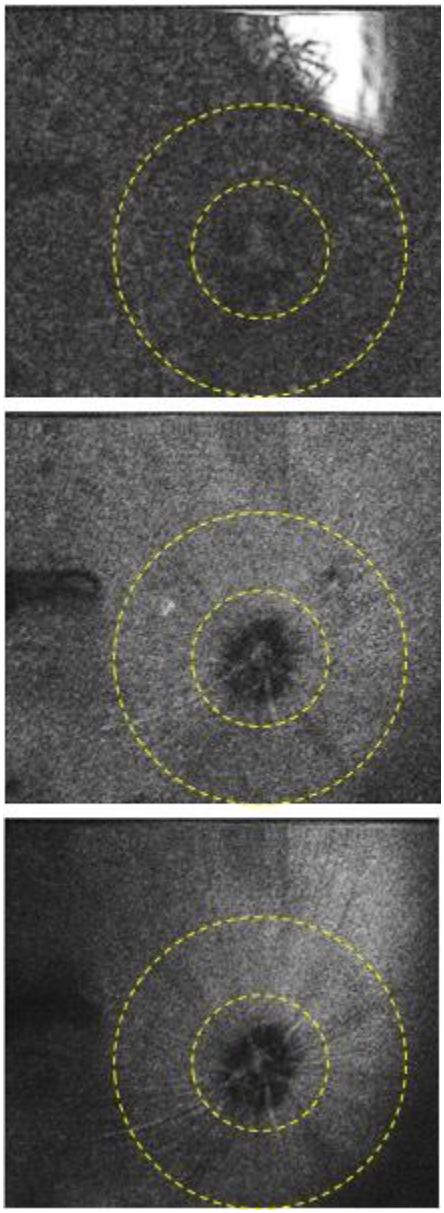

Figure 55: Three en-face images reconstructed from the same PM-SAD-OCT measurement. Upper: PM-SAD-OCT upper subimage corresponding to low-angle scattering. Middle: PM-SAD-OCT middle subimage corresponding to middle-angle scattering. Lower: PM-SAD-OCT lower subimage corresponding to high-angle scattering. The region of interest is a ring region around optic nerve head, and plotted on the en-face images.

5.4.3. Results

5.4.3.1 Time Variation of I_{Low}/I_{High} and NRI during Retinal Degeneration

For each rat eye, I_{Low}/I_{High} was calculated from a region of interest. The region of interest was defined as the RNFL layer around optic nerve head (Figure 55). Both I_{Low}/I_{High} and normalized reflectance index (NRI) were computed from the PM-SAD-OCT images and plotted versus time (Figure 56 and Figure 57). Since two dissection protocols were used in this study, the results are presented separately according to dissection protocols.

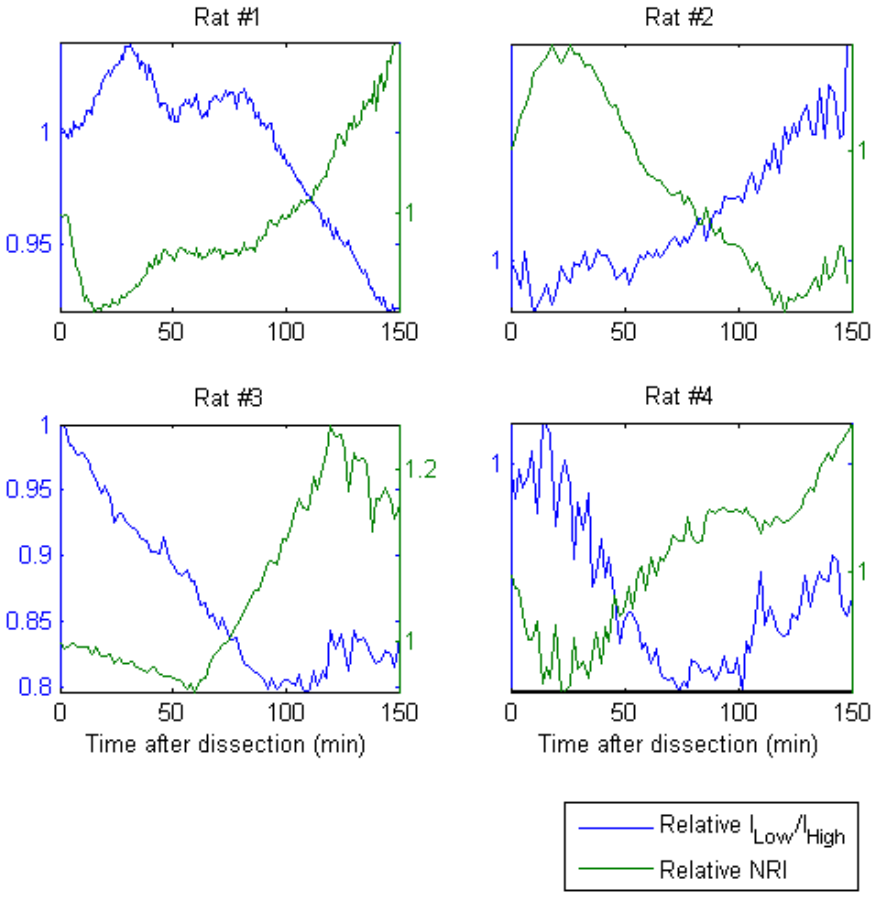

Figure 56: I_{Low}/I_{High} and NRI vs. time after dissection from four rat eyes using Coverslip Protocol.

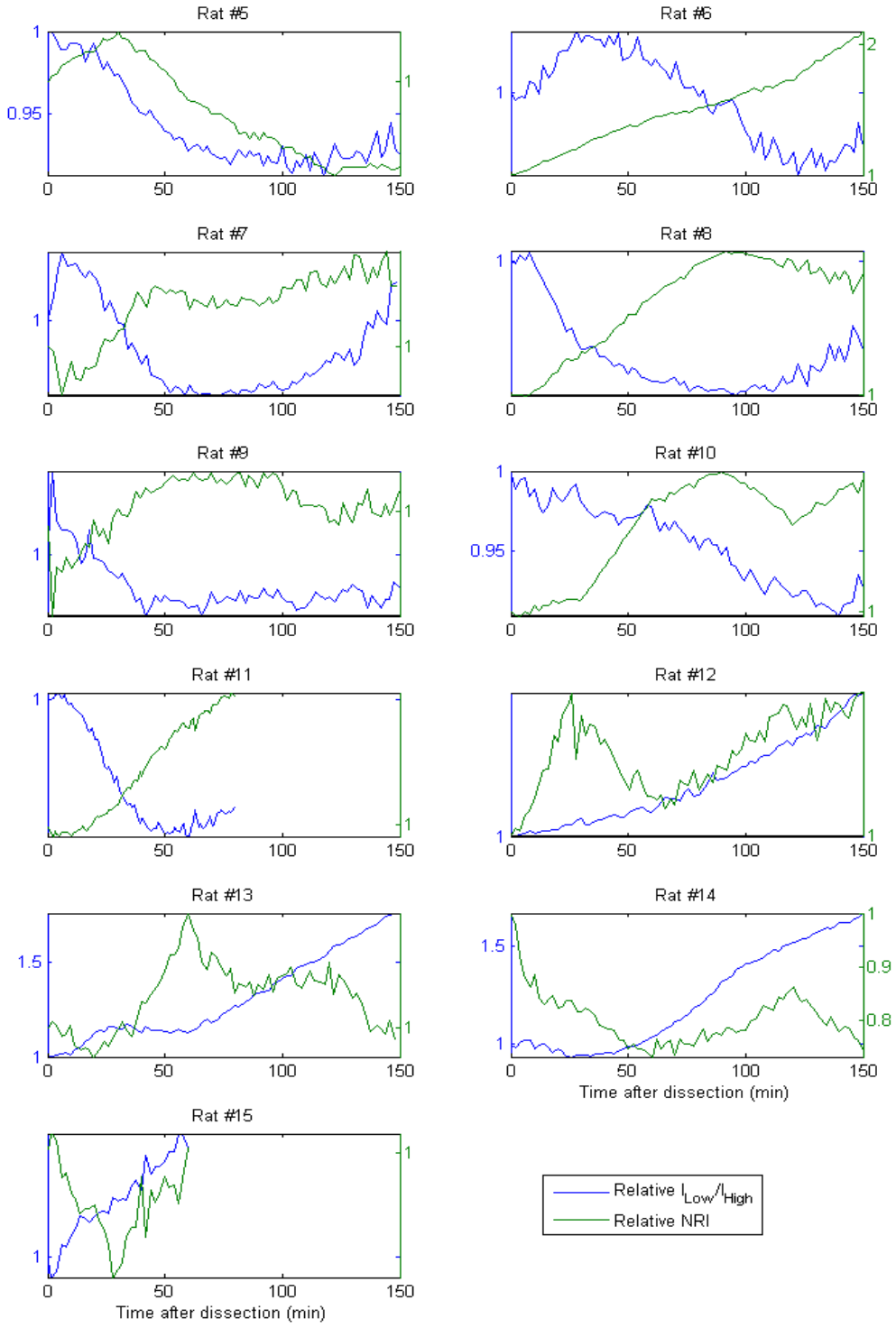

Figure 57: I_{Low}/I_{High} and NRI vs. time after dissection from eleven rat eyes using Sandstone Protocol.

From the measured I_{Low}/I_{High} and NRI, a number of statistical analyses were performed and summarized in Table 14. To quantitatively study the time variation of I_{Low}/I_{High} and NRI, I_{Low}/I_{High} and NRI were fitted with a linear regression model:

$$P_{i,t} = a_{1,i} + a_{2,i} \cdot t + e_{i,t} \tag{34}$$

where $P_{i,t}$ is the value of parameter P (either I_{Low}/I_{High} or NRI) of the i-th rat eye on time point t, and $e_{i,t}$ is a random error component. The model assumes that for the i-th rat eye, I_{Low}/I_{High} and NRI changes over time linearly with intercept $a_{1,i}$ and slope $a_{2,i}$, and the intercept and slope are independent among each rat. From the linear regression model, a p-value associated with the slope was calculated with the following null hypothesis: the slope is equal to zero. The slopes and associated p-values for I_{Low}/I_{High} and NRI are listed in Table 14. According to the sign of the slopes and p-values, the time variations of I_{Low}/I_{High} and NRI were classified into three categories: increase (positive slope, $p<0.05$), decrease (negative slope, $p<0.05$), and no significant change ($p>0.05$). The observation from the time variation of I_{Low}/I_{High} and NRI are summarized below:

In majority of rat eyes, I_{Low}/I_{High} generally decreases after dissection (sign test p=0.3018). Among the four rat eyes dissected using Coverslip Protocol (Rat #1-4 in Figure 56 and Table 14), three of them decreased and one increased in the value of I_{Low}/I_{High}. Among the eleven rat eyes dissected using Sandstone Protocol (Rat #5-15 in Figure 57 and Table 14), seven of them decreased and four increased in the value of I_{Low}/I_{High}.

In majority of rat eyes, NRI generally increases after dissection (sign test p=0.0225). Among the four rat eyes dissected using Coverslip Protocol (Rat #1-4 in Figure 56 and Table 14), three of them increased and one decreased in the value of NRI. Among the eleven rat eyes dissected using Sandstone Protocol (Rat #5-15 in Figure 57

and Table 14), eight of them increased and two decreased in the value of NRI, while one did not show significant change in NRI.

Rat #	Prep	I_{Low}/I_{High} vs. time		NRI vs. time		Correlation between I_{Low}/I_{High} and NRI	
		Slope (%/min)	p	Slope (%/min)	p	Correlation coefficient	p
1	Coverslip	-0.063978	6.73E-41	0.074275	1.09E-46	-0.96168	4.60E-85
2		0.10506	5.01E-33	-0.18659	1.99E-32	-0.87198	2.41E-24
3		-0.11996	3.95E-26	0.19054	4.45E-23	-0.66609	5.16E-11
4		-0.040791	1.20E-07	0.27418	8.92E-29	-0.60974	5.03E-09
5	Sandstone	-0.048897	7.66E-20	-0.30039	2.64E-36	0.77964	1.07E-16
6		-0.06112	4.41E-19	0.65129	3.64E-67	-0.76991	4.36E-16
7		-0.025916	0.001045	0.038919	8.88E-22	-0.65119	2.52E-10
8		-0.079663	4.10E-08	0.45283	1.30E-22	-0.87095	1.33E-23
9		-0.022426	1.39E-08	0.045757	0.00026	-0.86039	9.08E-23
10		-0.057541	4.46E-43	0.18453	1.69E-18	-0.71017	9.69E-13
11		-0.16473	4.48E-25	0.39654	3.53E-61	-0.85059	3.39E-23
12		0.2613	2.02E-48	0.055994	4.96E-09	0.65133	3.31E-10
13		0.49432	2.58E-41	0.037616	0.009016	0.055792	0.63919
14		0.54477	4.50E-38	-0.04094	0.00185	-0.10041	0.39797
15		0.3952	1.54E-20	-0.031313	0.50615	-0.207	0.26385

Table 14: Statistical analysis of Study 2 results.

5.4.3.2 Correlation between I_{Low}/I_{High} and NRI during Retinal Degeneration

According to the observations with time variation of I_{Low}/I_{High} and NRI, it is highly possible that I_{Low}/I_{High} and NRI are correlated during retinal degeneration. The correlation between I_{Low}/I_{High} and NRI was characterized with a correlation coefficient.

The correlation coefficient is a value between -1 and 1 calculated from two variables. When correlation coefficient is close to 1, the two variables are strongly positively correlated; when correlation coefficient is close to -1, the two variables are

strongly negatively correlated; and when correlation coefficient is close to 0, the correlation between the two variables is weak.

The correlation coefficient between I_{Low}/I_{High} and NRI was computed for each rat eye. A *p*-value was also calculated for each rat eye, with the null hypothesis: the correlation coefficient is equal to zero. The correlation coefficients and *p*-values are listed in Table 14. According to the sign of the correlation coefficients and *p*-values, the correlation relationship between I_{Low}/I_{High} and NRI were classified into three categories: positively correlated (positive correlation coefficient, $p<0.05$), negatively correlated (negative correlation coefficient, $p<0.05$), and no significant correlation ($p>0.05$). The observation from the correlation of I_{Low}/I_{High} and NRI are summarized below:

In majority of rat eyes, I_{Low}/I_{High} and NRI are negatively correlated (sign test p=0.0386). Among the four rat eyes dissected using Coverslip Protocol (Rat #1-4 in Figure 56 and Table 14), all of them showed negative correlation between I_{Low}/I_{High} and NRI. Among the eleven rat eyes dissected using Sandstone Protocol (Rat #5-15 in Figure 57 and Table 14), six of them showed negative correlation, two showed positive correlation, and three did not show significant correlation between I_{Low}/I_{High} and NRI.

5.4.4. Discussion and Summary

Due to the limited number of rat eyes included in this study, it is difficult to draw any further conclusions from this animal study. However, it is clear that PM-SAD-OCT is capable of characterizing scattering changes of rat retinas. The inconsistency in I_{Low}/I_{High} and NRI measurements across rats suggest that there may be multiple mechanisms affecting the scattering properties of RNFL during retinal degeneration. Further studies are required to draw a stronger connection between the scattering property and functionality of the retina.

I_{Low}/I_{High} and NRI has strong correlation. Since NRI has been proven useful in detecting glaucoma, I_{Low}/I_{High} determined from PM-SAD-OCT is strongly expected to become a powerful glaucoma indicator.

As a summary, in this preliminary study, retinas from 15 rats were dissected and imaged using PM-SAD-OCT for 150 minutes during retinal degeneration. Time variations of I_{Low}/I_{High} as well as normalized reflectance index (NRI) have been observed. In majority cases, I_{Low}/I_{High} tends to decrease while NRI tends to increase during retinal degeneration. The mechanism behind the change of scattering properties of rat retina remains unclear and further studies are required to verify the observations in this study.

5.5. STUDY 3: *IN VITRO* PM-SAD-OCT MEASUREMENT ON EARTHWORM NERVE CORD DURING NEURODEGENERATION

5.5.1. Introduction

Neurodegenerative disease is a class of conditions which primarily affect the neurons in the brain and spinal cord. Common neurodegenerative diseases include Alzheimer's disease, Huntington's disease, and Parkinson's disease. Glaucoma is sometimes considered as a type of neurodegenerative disease as well. Most of the neurodegenerative diseases are irreversible and can be life-threatening. Although most neurodegenerative diseases have no cures, medications or surgeries are usually available to control the progression and symptoms, especially at early stages of the diseases. So, early detection of neuronal apoptosis is crucial for the treatment of neurodegenerative diseases.

If PM-SAD-OCT is sensitive enough to detect the scattering change induced by intensified mitochondrial fission during cell apoptosis, its application is not limited in glaucoma diagnosis. Neurodegenerative diseases include the apoptosis of neuron bodies

or nerve fibers, which is expected to be accompanied by changes in optical scattering properties. Measurement of neuronal scattering changes associated with apoptosis may provide insight into neuronal cytophysiology associated with pathogenesis. The purpose of this study is to demonstrate the application PM-SAD-OCT imaging during the degeneration of nerve fibers.

Earthworm (Lumbricus terrestris) is a common type of animal model in neuroscience, toxicology and microsurgical training because of its simple structure, large size and low cost [122, 123]. In this study, earthworm nerve cords were dissected and imaged using PM-SAD-OCT over a 150-minute time period. Time variation of intensity ratios of low-angle and high-angle backscattering from nerve cords during neuronal apoptosis was recorded. PM-SAD-OCT data indicate that in nerve cords undergoing neuronal apoptosis ratio of high to low-angle backscatter changes with time.

5.5.2. Methods

The earthworm is anesthetized with 15% alcohol for 2.5 minutes before dissection. The dissection of earthworm is explained in Figure 58. A cut of ~5 mm long is made from dorsal side. Dorsal blood vessel and intestine are removed, so that the ventral nerve cord of the earthworm becomes accessible. The earthworm usually stays alive for ~30 minutes after the dissection, and dies from bleeding later.

Spontaneous action potentials of the nerve cord are recorded with a pair of electrodes and an amplifier in order to understand the time frame that the nerve cord maintains functional integrity (Figure 58). The spontaneous action potentials are successfully recorded from 3 earthworms (Figure 59). The firing rate of spontaneous action potential is calculated over time. The results from the recorded action potentials

show that the firing rate of nerve cord drops down to baseline noise at ~150 minutes after the dissection, so the nerve cord is considered degenerated after 150 minutes.

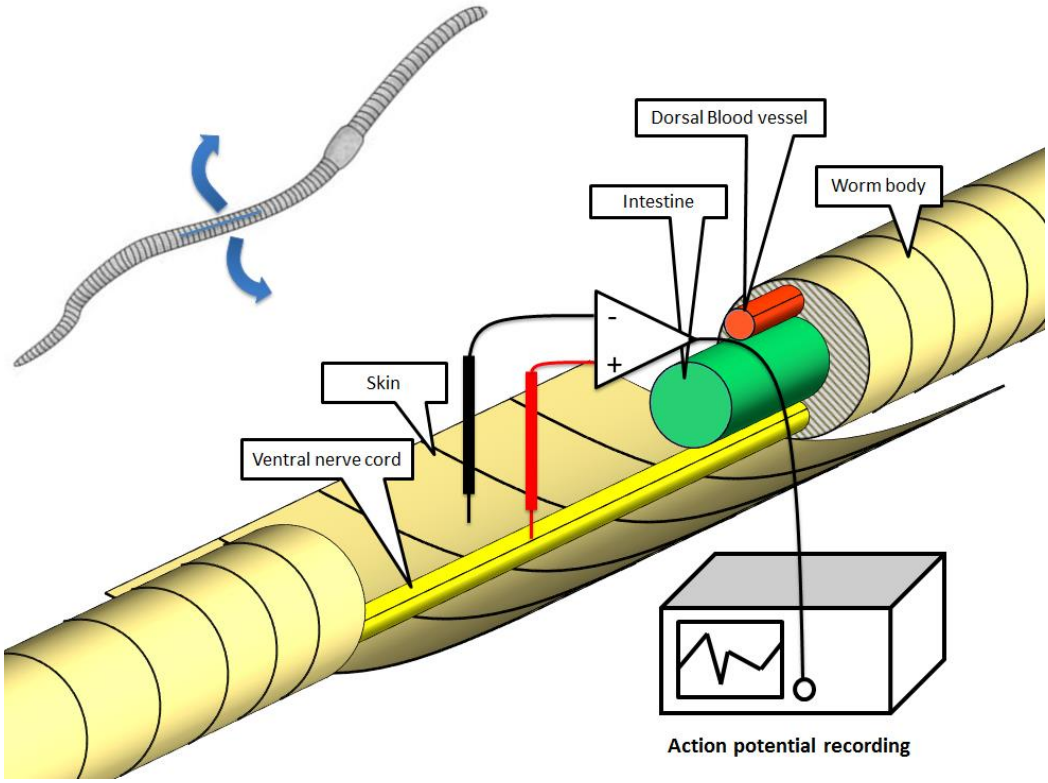

Figure 58: Dissection of earthworm to expose nerve cord. Action potential is recorded from earthworm nerve cord.

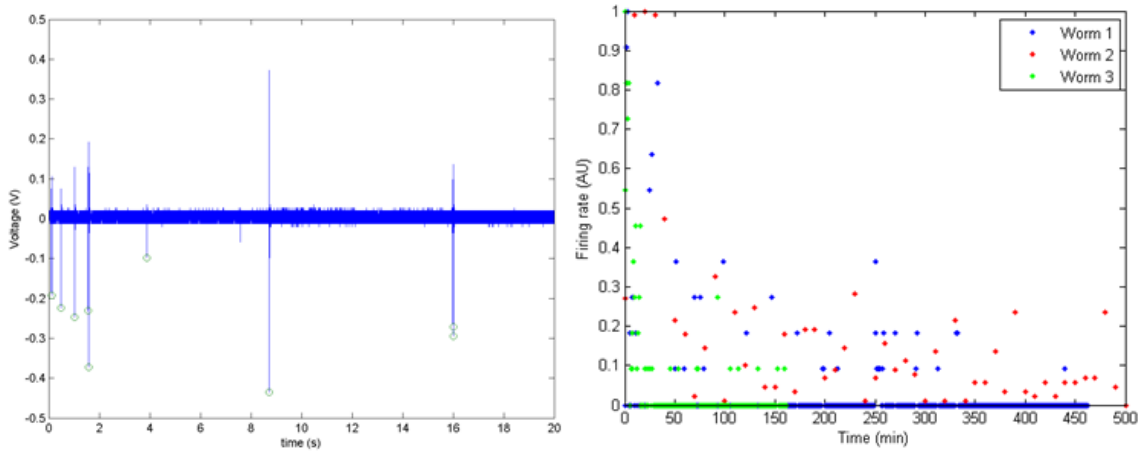

Figure 59: Left: Recorded action potential from earthworm nerve cord. Right: Firing rate of action potential decreases over time.

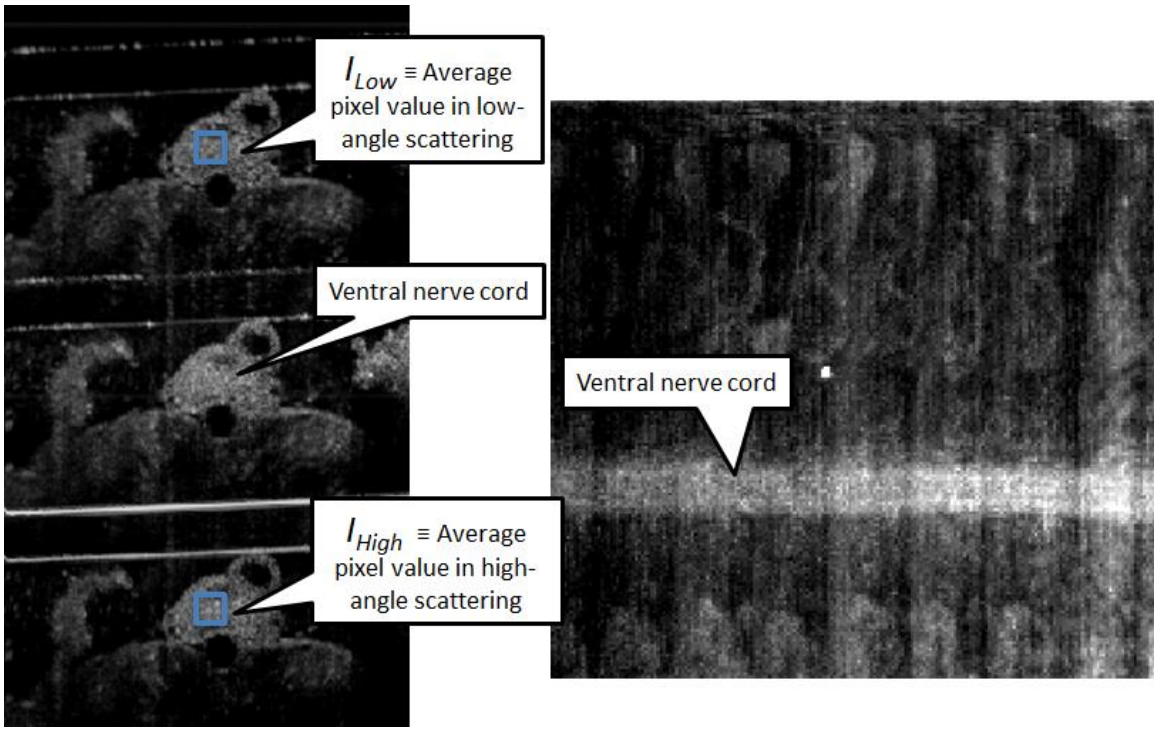

Figure 60: Left: PM-SAD-OCT B-scan image of earthworm nerve cord. The region of interest is plotted on the upper and lower subimages. Right: PM-SAD-OCT enface image of earthworm nerve cord.

Then, PM-SAD-OCT images are acquired from 9 earthworm nerve cords for 150 minutes after dissection using a 1300 nm PM-SAD-OCT system (Figure 60). The nerve cord provides good contrast under PM-SAD-OCT. For each earthworm, I_{Low}/I_{High} is calculated from a region of interest, which is manually selected at the center of nerve cord, and plotted versus time (Figure 61).

5.5.3. Results

Unexpectedly, although I_{Low}/I_{High} acquired from the 9 earthworm nerve cords exhibits certain changes over time, the changes are not consistent among the 9

earthworms. The results suggest that either there is no consistent scattering change in earthworm nerve cord, or current PM-SAD-OCT instrument is not sufficiently sensitive to detect the scattering changes associated with the death of nerve cord. In addition, multiple possible problems about the earthworm model are identified.

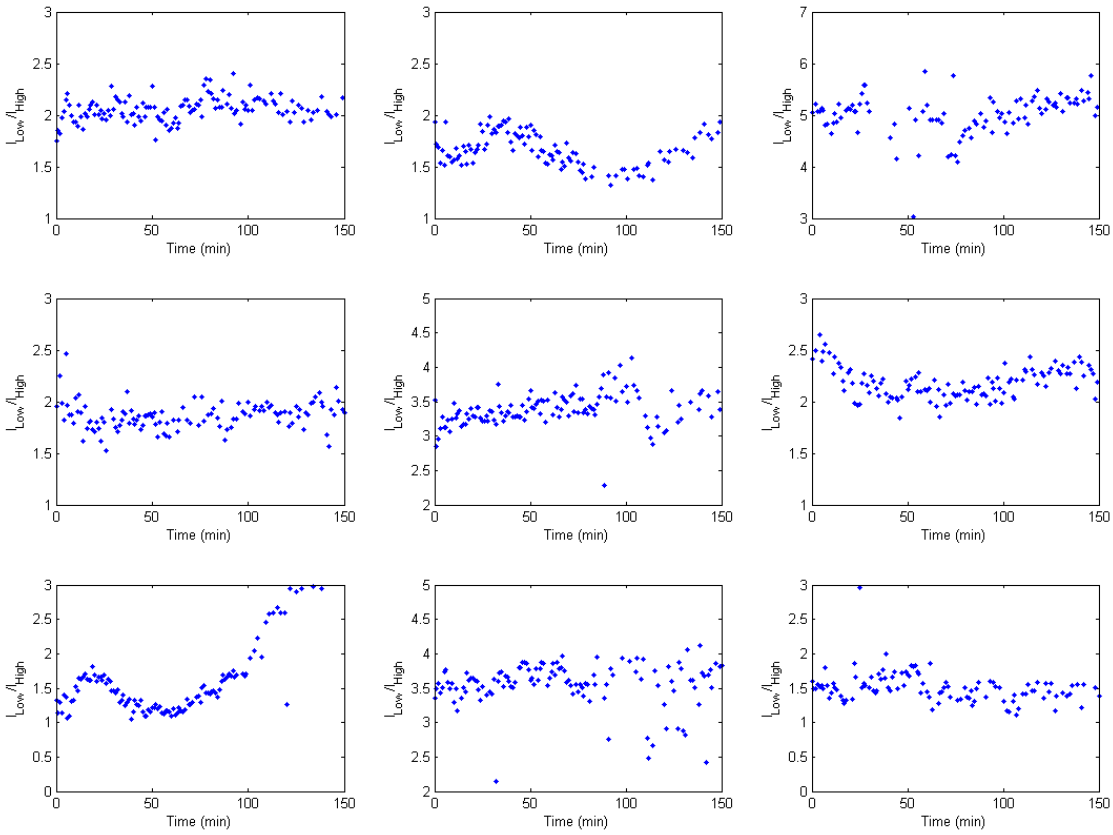

Figure 61: I_{Low}/I_{High} vs. time after dissection from 9 earthworms.

5.5.4. Discussion and Summary

First, the nerve cord of earthworm is composed of three giant fibers with heavy myelin-like sheath, and many small-diameter unmyelinated fibers. The myelinated giant fibers cover the small-diameter unmyelinated fibers, and may introduce more scattering events and broaden backscattering angular distribution, finally making the calculation of I_{Low}/I_{High} less reliable in terms of representing tissue scattering properties.

Second, it is not clear if axons in earthworm nerve cord contain mitochondrial network. If the mitochondria in earthworm nerve cord axons do not require forming network to maintain functionality and always stay in the fission state, then the apoptosis of nerve cord will not be associated with optical scattering change. According to the microscope image of earthworm nerve cord (Figure 62), no mitochondrial network has been identified. However, higher resolution microscope images are required to confirm the conclusion that earthworm nerve cord do not contain mitochondrial network.

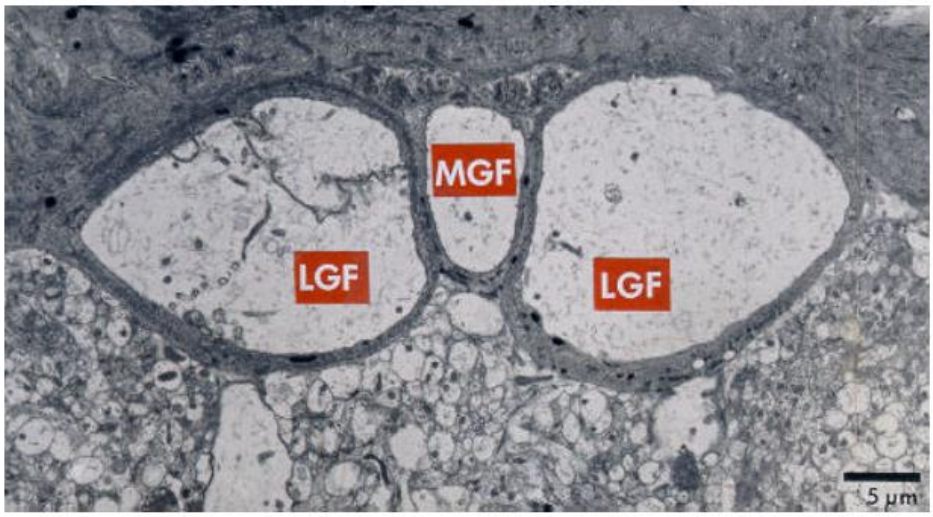

Figure 62: Cross-sectional view of earthworm nerve cord (dorsal portion of posterior ventral nerve cord). MGF, medial giant fiber; LGF lateral giant fiber. The giant fibers are surrounded by heavy myelin-like sheath, while the small-diameter fibers in the neuropil region below the giant nerve fibers are unmyelinated [124]. Mitochondria density appears to be low in the giant fibers.

Third, as the earthworm dies from bleeding, the underlying neurodegeneration mechanism in the nerve cord may not be exactly same as that in neurodegenerative diseases. It is possible that the neuronal apoptosis process in this study is not a good model for neurodegenerative disease.

As a summary, in this study, 9 earthworm nerve cords were dissected and imaged in vitro using PM-SAD-OCT for 150 minutes. Consistent time variation of I_{Low}/I_{High} is not yet observed from the 9 earthworm nerve cords undergoing apoptosis. Several possible problems regarding the earthworm model are identified and further studies are required to draw any additional conclusion.

5.6. NEXT GENERATION PM-SAD-OCT

While the PM-SAD-OCT reported here is promising for characterizing retinal scattering properties which may be relevant for early-stage glaucoma diagnosis, a number of limitations are recognized. First, the incident light is not constrained to a single incident direction which has the effect of blurring angle resolved data. As a result, the middle subimage is degenerate which does not provide useful information, and the angular ranges have certain overlay between the upper and lower subimages (Table 13). To constrain the incident light in a single incident direction, a new design of PM-SAD-OCT is proposed in Figure 63. The main change is the insertion of a reflective mirror with an aperture in the center. The incident light uses a small diameter collimator to fire a narrow beam which travels through the aperture of the mirror, so that light incident on the sample with low incident angle only. However, the scattered light is divided into two paths by the mirror: the low scattered angle path is able to pass the aperture of the mirror and is coupled by the same collimator for incident light, forming a low-incident low-scattered path; the high scattered angle path is reflective by the mirror, and is coupled into a separate collimator, forming a low-incident high-scattered path. A PME can be inserted into the high scattered angle path to further divide the high scattered angle into different smaller angular subgroups.

Another problem with the current configuration of PM-SAD-OCT reported here is the limited angular resolution with only three discrete subimages. Higher angular resolution may enhance some applications. A simple solution is to replace the current PME with a step-shaped one. With the step-shaped PME, the number of PM-SAD-OCT subimages can be infinitely increased, at the cost of reduced signal strength in each subimage and the requirement for a light source with increased coherence length.

In addition, the angular range (2.53°, Fig. 2) in the current configuration is fairly small compared to previous non-ophthalmological studies [108, 109, 111, 112, 114]. The small angular range limits the utility of the instrument in terms of detecting scattering changes in a sample. A larger angular range is expected to improve system sensitivity to detect variations in sample scattering properties. This problem is not easily fixed with the current design, but with the new design in Figure 63, the angular range can be increased by simply using a larger mirror with aperture in the incident path. If the high scattered angle beam is too big to couple into the collimator, a telescope may be placed in the high scattered angle path to reduce the beam size before the scattered light is coupled into the collimator.

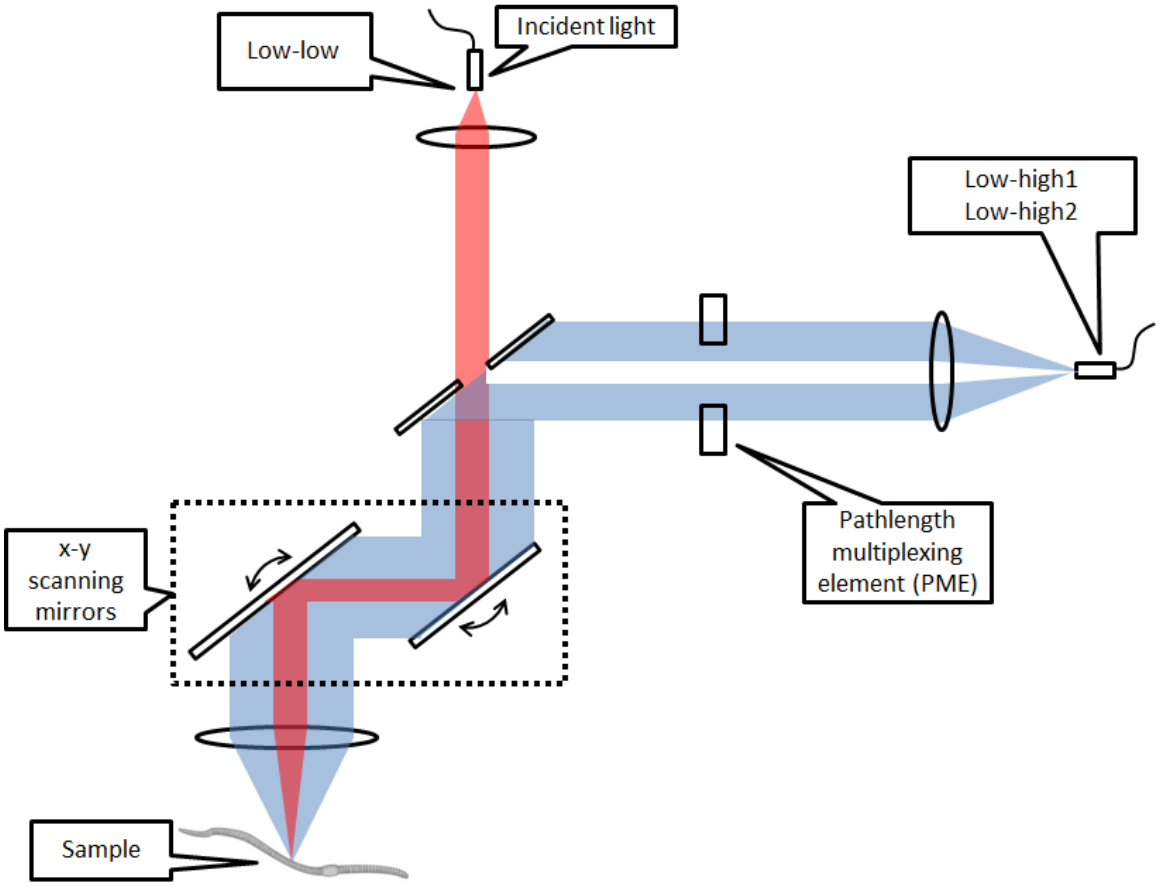

Figure 63: Schematic of a PM-SAD-OCT without degenerate paths.

Additional improvements with the PME can be made. For example, an azimuthal PME may be able to detect the polarimetric-angular anisotropy of RNFL backscattered light (Figure 64). Similar to the current radial PME, the azimuthal PME gives three retinal sub-images when positioned in a PS-OCT: vertical incident/vertical backscattered (short-short path); degenerate vertical/horizontal paths (medium length path); and horizontal incident/horizontal backscattered (long-long path). The azimuthal PME will allow objective measurement of the RNFL backscattering anisotropy (I_H/I_V) and will provide sensitive detection of differences in polarization-angular anisotropy of backscattered light from RGC axons with mitochondria in fission and fusion states.

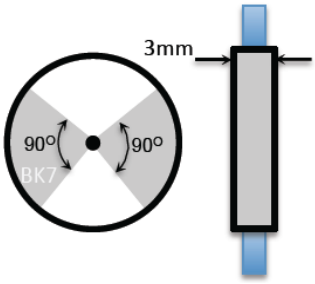

Figure 64: Design of an azimuthal PME. The azimuthal PME will be constructed using two 3mm thick 90-degree angular sectors constructed from BK7 glass. Outer (inner) surfaces of the two glass angular sectors will be fastened with epoxy to 25mm (1mm) stainless-steel rings. Left: end-on view; Right: side view.

With increased number of PMEs with different types and aperture sizes, the difficult operation of PM-SAD-OCT may not be suitable for clinical use. A PME wheel is designed in Figure 65 with multiple PMEs different in types and/or sizes. The PME wheel is designed to be motorized, so that the operator of PM-SAD-OCT can switch to a certain PME conveniently by rotating the PME wheel via a control software.

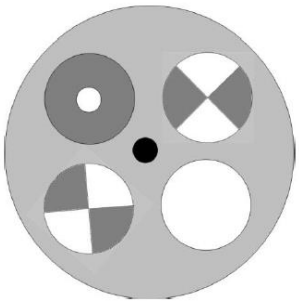

Figure 65: Multiple PMEs on a wheel.

5.7. CONCLUSION OF THIS CHAPTER

In this Chapter, a low resolution pathlength-multiplexed scattering-angle-diverse OCT (PM-SAD-OCT) is designed and built to measure the scattering properties of the sample by providing a new parameter, low-to-high angle backscattering anisotropy

(I_{Low}/I_{High}). Two PM-SAD-OCT studies are performed to demonstrate the application of PM-SAD-OCT on retinal imaging on either human or rats. The third study extends PM-SAD-OCT application to investigate neurodegeneration with an earthworm experiment. Although there are certain difficulties with current PM-SAD-OCT like degenerate paths and insufficient angular resolution, a design for next-generation PM-SAD-OCT is proposed which overcomes many of the current limitations.

The hypothesis underlying the application of PM-SAD-OCT is that the scattering properties of certain tissues (e.g., RNFL) may change in early-stage diseases (e.g. glaucoma). Although scattering changes have been observed in both non-human primate and human eyes [28, 29], more studies are necessary to document the origins of the change of RNFL scattering properties.

References

1. Fischer, H. *Three Main Layers of the Eye*. Available from: http://en.wikipedia.org /wiki/Human_eye#mediaviewer/File:Three_Main_Layers_of_the_Eye.png.
2. Pocock, G.M., *The Relationship between Retinal Ganglion Cell Axon Constituents and Birefringence in the Primate Retinal Nerve Fiber Layer*, in *Biomedical Engineering*. 2009, The University of Texas at Austin: Austin.
3. *EYE AND RETINA*. Available from: http://www.bioon.com/bioline/neurosci /course/eyeret.html.
4. Quigley, H.A., et al., *Retinal ganglion cell death in experimental glaucoma and after axotomy occurs by apoptosis.* Investigative ophthalmology & visual science, 1995. **36**(5): p. 774-786.
5. Quigley, H.A., *Number of people with glaucoma worldwide.* Br J Ophthalmol, 1996. **80**(5): p. 389-93.
6. Quigley, H.A. and A.T. Broman, *The number of people with glaucoma worldwide in 2010 and 2020.* Br J Ophthalmol, 2006. **90**(3): p. 262-7.
7. Anderson, D.R., *Glaucoma: the damage caused by pressure. XLVI Edward Jackson Memorial Lecture.* American Journal of Ophthalmology, 1989. **108**: p. 485-495.
8. Anderson, D.R., *Introductory comments on blood flow autoregulation in the optic nerve head and vascular risk factors in glaucoma.* Survey of Ophthalmology, 1999. **43**(Supplement 1): p. S5-S9.
9. Hernandez, M.R., W.M. Andrzejewska, and A.H. Neufeld, *Changes in the extracellular matrix of the human optic nerve head in primary open-angle glaucoma.* American Journal of Ophthalmology, 1990. **109**(180-188).
10. Hernandez, M.R., J.D. Pena, and J.A. Selvidge, *The optic nerve head in glaucomatous optic neuropathy.* Archives of Ophthalmology, 1997. **115**(389-395).
11. Hernandez, M.R., J.D. Pena, and J.A. Selvidge, *Hydrostatic pressue simulates synthesis of elastin in cultured optic nerve head astrocytes.* Glia, 2000. **32**: p. 122-136.
12. Wax, M.B., *Is there a role for the immune system in glaucomatous optic neuropathy?* Curr Opin Ophthalmol, 2000. **11**: p. 145-150.
13. Neufeld, A.H., M.R. Hernandez, and M. Gonzalez, *Nitric oxide synthase in the human glaucomatous optic nerve head.* Archives of Ophthalmology, 1997. **115**: p. 497-503.

14. Neufeld, A.H. and B. Liu, *Glaucomatous Optic Neuropathy: When Glia Misbehave.* Neuroscientist, 2003. **9**(6): p. 485-495.

15. Tielsch, J.M., et al., *Racial variations in the prevalence of primary open-angle glaucoma.* JAMA: the journal of the American Medical Association, 1991. **266**(3): p. 369-374.

16. Wang, Y., O. Tan, and D. Huang. *Investigation of retinal blood flow in normal and glaucoma subjects by Doppler Fourier-domain optical coherence tomography*. in *SPIE BiOS: Biomedical Optics*. 2009: International Society for Optics and Photonics.

17. Wang, Y., et al., *Measurement of total blood flow in the normal human retina using Doppler Fourier-domain optical coherence tomography.* British Journal of Ophthalmology, 2009. **93**(5): p. 634-637.

18. Huang, D., et al., *Optical coherence tomography.* Science, 1991. **254**(5035): p. 1178.

19. Fercher, A.F., et al., *Measurement of intraocular distances by backscattering spectral interferometry.* Optics Communications, 1995. **117**(1): p. 43-48.

20. Ha, G. and M.W. Lindner, *"Coherence radar" and "spectral radar"—new tools for dermatological diagnosis.* Journal of biomedical optics, 1998. **3**(1): p. 21-31.

21. HUANG, D. *OCT Terminology – Demystified!* 2009; Available from: http://www.ophthalmologymanagement.com/articleviewer.aspx?articleid=102795.

22. Wieser, W., et al., *Multi-megahertz OCT: High quality 3D imaging at 20 million A-scans and 4.5 GVoxels per second.* Optics Express, 2010. **18**(14): p. 14685-14704.

23. *American National Standard for Safe Use of Lasers*, A.N.S. Institute, Editor. 2000.

24. Huang, X.R. and R.W. Knighton, *Microtubules contribute to the birefringence of the retinal nerve fiber layer.* Investigative ophthalmology & visual science, 2005. **46**(12): p. 4588-4593.

25. Weinreb, R.N., C. Bowd, and L.M. Zangwill, *Glaucoma detection using scanning laser polarimetry with variable corneal polarization compensation.* Archives of Ophthalmology, 2003. **121**(2): p. 218-224.

26. Bagga, H., et al., *Scanning laser polarimetry with variable corneal compensation and optical coherence tomography in normal and glaucomatous eyes.* American Journal of Ophthalmology, 2003. **135**(4): p. 521-529.

27. Mohammadi, K., et al., *Retinal nerve fiber layer thickness measurements with scanning laser polarimetry predict glaucomatous visual field loss.* American Journal of Ophthalmology, 2004. **138**(4): p. 592-601.

28. Liu, S., et al., *Retinal nerve fiber layer reflectance for early glaucoma diagnosis.* Journal of Glaucoma, 2013.

29. Dwelle, J., et al., *Thickness, phase retardation, birefringence, and reflectance of the retinal nerve fiber layer in normal and glaucomatous non-human primates.* Investigative ophthalmology & visual science, 2012.

30. Mujat, M., et al., *Retinal nerve fiber layer thickness map determined from optical coherence tomography images.* Optics Express, 2005. **13**(23): p. 9480-9491.

31. Garvin, M.K., et al., *Intraretinal layer segmentation of macular optical coherence tomography images using optimal 3-D graph search.* IEEE Transactions on Medical Imaging, 2008. **27**(10): p. 1495-1505.

32. Paranjape, A.S., et al., *Automated method for RNFL segmentation in spectral domain OCT.* Proc. SPIE, 2008. **6848**: p. 68480N.

33. Mishra, A., et al., *Intra-retinal layer segmentation in optical coherence tomography images.* Optics Express, 2009. **17**(26): p. 23719-23728.

34. Kajić , V., et al., *Robust segmentation of intraretinal layers in the normal human fovea using a novel statistical model based on texture and shape analysis.* Optics Express, 2010. **18**(14): p. 14730-14744.

35. Mayer, M.A., et al., *Retinal Nerve Fiber Layer Segmentation on FD-OCT Scans of Normal Subjects and Glaucoma Patients.* Biomedical Optics Express, 2010. **1**(5): p. 1358-1383.

36. Cabrera Fernández, D., H.M. Salinas, and C.A. Puliafito, *Automated detection of retinal layer structures on optical coherence tomography images.* Optics Express, 2005. **13**(25): p. 10200-10216.

37. Yazdanpanah, A., et al., *Segmentation of intra-retinal layers from optical coherence tomography images using an active contour approach.* IEEE transactions on medical imaging, 2011. **30**(2): p. 484.

38. Klotz, A.C., *2D and 3D multiphase active contours without edges based algorithms for simultaneous segmentation of retinal layers from OCT images.* 2013.

39. Amadieu, O., et al. *Inward and outward curve evolution using level set method*. in *Image Processing, 1999. ICIP 99. Proceedings. 1999 International Conference on*. 1999: IEEE.

40. Osher, S. and R.P. Fedkiw, *Level set methods: an overview and some recent results.* Journal of Computational physics, 2001. **169**(2): p. 463-502.

41. Gomes, J. and O. Faugeras, *Reconciling distance functions and level sets.* Journal of Visual Communication and Image Representation, 2000. **11**(2): p. 209-223.

42. Li, C., et al. *Level set evolution without re-initialization: a new variational formulation*. in *Computer Vision and Pattern Recognition, 2005. CVPR 2005. IEEE Computer Society Conference on*. 2005: IEEE.

43. Chan, T.F. and L.A. Vese, *Active contours without edges.* Image Processing, IEEE Transactions on, 2001. **10**(2): p. 266-277.

44. Hee, M.R., et al., *Polarization-sensitive low-coherence reflectometer for birefringence characterization and ranging.* Journal of the Optical Society of America B, 1992. **9**(6): p. 903-908.

45. De Boer, J.F., et al., *Two-dimensional birefringence imaging in biological tissue by polarization-sensitive optical coherence tomography.* Optics Letters, 1997. **22**(12): p. 934-936.

46. Saxer, C.E., et al., *High-speed fiber based polarization-sensitive optical coherence tomography of in vivo human skin.* Optics Letters, 2000. **25**(18): p. 1355-1357.

47. Everett, M.J., et al., *Birefringence characterization of biological tissue by use of optical coherence tomography.* Optics letters, 1998. **23**(3): p. 228-230.

48. Park, B.H., et al., *In vivo burn depth determination by high-speed fiber-based polarization sensitive optical coherence tomography.* Journal of Biomedical Optics, 2001. **6**: p. 474.

49. Cense, B., et al., *In vivo depth-resolved birefringence measurements of the human retinal nerve fiber layer by polarization-sensitive optical coherence tomography.* Optics letters, 2002. **27**(18): p. 1610-1612.

50. Davé, D.P., T. Akkin, and T.E. Milner, *Polarization-maintaining fiber-based optical low-coherence reflectometer for characterization and ranging of birefringence.* Optics letters, 2003. **28**(19): p. 1775-1777.

51. Götzinger, E., et al., *Polarization maintaining fiber based ultra-high resolution spectral domain polarization sensitive optical coherence tomography.* Optics Express, 2009. **17**(25): p. 22704-22717.

52. Al-Qaisi, M.K. and T. Akkin, *Swept-source polarization-sensitive optical coherence tomography based on polarization-maintaining fiber.* Optics Express, 2010. **18**(4): p. 3392-3403.

53. Park, B.H., et al., *Jones matrix analysis for a polarization-sensitive optical coherence tomography system using fiber-optic components.* Optics letters, 2004. **29**(21): p. 2512-2514.

54. Park, B.H., et al., *Optic axis determination accuracy for fiber-based polarization-sensitive optical coherence tomography.* Optics letters, 2005. **30**(19): p. 2587-2589.

55. Kemp, N., et al., *Depth-resolved optic axis orientation in multiple layered anisotropic tissues measured with enhanced polarization-sensitive optical coherence tomography (EPS-OCT).* Optics Express, 2005. **13**(12): p. 4507-4518.

56. Yamanari, M., S. Makita, and Y. Yasuno, *Polarization-sensitive swept-source optical coherence tomography with continuous source polarization modulation.* Optics Express, 2008. **16**(8): p. 5892-5906.

57. Park, J., et al., *Complex polarization ratio to determine polarization properties of anisotropic tissue using polarization-sensitive optical coherence tomography.* Optics Express, 2009. **17**(16): p. 13402-13417.

58. Elmaanaoui, B., et al., *Birefringence measurement of the retinal nerve fiber layer by swept source polarization sensitive optical coherence tomography.* Optics Express, 2011. **19**(11): p. 10252-10268.

59. Baumann, B., et al., *Swept source/Fourier domain polarization sensitive optical coherence tomography with a passive polarization delay unit.* Optics Express, 2012. **20**(9): p. 10229-10241.

60. Torzicky, T., et al., *Retinal polarization-sensitive optical coherence tomography at 1060 nm with 350 kHz A-scan rate using an Fourier domain mode locked laser.* Journal of biomedical optics, 2013. **18**(2): p. 026008-026008.

61. Roth, J.E., et al., *Simplified method for polarization-sensitive optical coherence tomography.* Optics Letters, 2001. **26**(14): p. 1069-1071.

62. Park, B.H., et al., *Jones matrix analysis for a polarization-sensitive optical coherence tomography system using fiber-optic components.* Optics letters, 2004. **29**(21): p. 2512.

63. Jiao, S., et al., *Optical-fiber-based Mueller optical coherence tomography.* Optics letters, 2003. **28**(14): p. 1206-1208.

64. Jiao, S., et al., *Fiber-based polarization-sensitive Mueller matrix optical coherence tomography with continuous source polarization modulation.* Applied optics, 2005. **44**(26): p. 5463-5467.

65. Oh, W.Y., et al., *High-speed polarization sensitive optical frequency domain imaging with frequency multiplexing.* Optics express, 2008. **16**(2): p. 1096-1103.

66. Yamanari, M., S. Makita, and Y. Yasuno, *Polarization-sensitive swept-source optical coherence tomography with continuous source polarization modulation.* Opt. Express, 2008. **16**: p. 5892-5906.

67. Cense, B., et al., *Thickness and birefringence of healthy retinal nerve fiber layer tissue measured with polarization-sensitive optical coherence tomography.* Investigative ophthalmology & visual science, 2004. **45**(8): p. 2606.

68. Yamanari, M., et al., *Phase retardation measurement of retinal nerve fiber layer by polarization-sensitive spectral-domain optical coherence tomography and scanning laser polarimetry.* Journal of biomedical optics, 2008. **13**: p. 014013.

69. Götzinger, E., et al., *Retinal nerve fiber layer birefringence evaluated with polarization sensitive spectral domain OCT and scanning laser polarimetry: A comparison.* Journal of Biophotonics, 2008. **1**(2): p. 129-139.

70. Mujat, M., et al., *Autocalibration of spectral-domain optical coherence tomography spectrometers for in vivo quantitative retinal nerve fiber layer birefringence determination.* Journal of biomedical optics, 2007. **12**: p. 041205.

71. Götzinger, E., et al., *Retinal nerve fiber layer birefringence evaluated with polarization sensitive spectral domain OCT and scanning laser polarimetry: A comparison.* Journal of Biophotonics, 2008. **1**(2).

72. Huang, X.R. and R.W. Knighton, *Microtubules contribute to the birefringence of the retinal nerve fiber layer.* Investigative ophthalmology & visual science, 2005. **46**(12): p. 4588.

73. Kandel, E.R., J.H. Schwartz, and T.M. Jessel, *Principles of Neural Science, 4th Ed.* 2000, New York: McGraw-Hill.

74. Hanninen, V.A., et al., *Activation of Caspase 9 in rat model of experimental glaucoma.* Current Eye Research, 2002. **25**(6): p. 389-395.

75. Kerrigan-Baumrind, L.A., et al., *Number of ganglion cells in glaucoma eyes compared with threshold visual field tests in the same persons.* Investigative Ophthalmology and Visual Science, 2000. **41**(3): p. 741-748.

76. Fortune, B., G.A. Cull, and C.F. Burgoyne, *Relative course of retinal nerve fiber layer birefringence and thickness and retinal function changes after optic nerve transection.* Investigative Ophthalmology & Visual Science, 2008. **49**(10): p. 4444.

77. Park, J., et al., *Differential geometry of normalized Stokes vector trajectories in anisotropic media.* JOSA A, 2006. **23**(3): p. 679-690.

78. Pocock, G.M., et al., *The relationship between retinal ganglion cell axon constituents and retinal nerve fiber layer birefringence in the primate.* Investigative ophthalmology & visual science, 2009. **50**(11): p. 5238.

79. Yin, B., et al. *High-speed polarization sensitive optical coherence tomography for retinal diagnostics*. 2012.

80. Marquardt, D.W., *An algorithm for least-squares estimation of nonlinear parameters.* Journal of the society for Industrial and Applied Mathematics, 1963. **11**(2): p. 431-441.

81. Kemp, N.J., et al., *High-sensitivity determination of birefringence in turbid media with enhanced polarization-sensitive optical coherence tomography.* JOSA A, 2005. **22**(3): p. 552-560.

82. Glovinsky, Y., H. Quigley, and G. Dunkelberger, *Retinal ganglion cell loss is size dependent in experimental glaucoma.* Investigative ophthalmology & visual science, 1991. **32**(3): p. 484.

83. Wang, B., et al., *Optimized retinal nerve fiber layer segmentation based on optical reflectivity and birefringence for polarization-sensitive optical coherence tomography.* 2011.

84. Schuman, J.S., et al., *Quantification of nerve fiber layer thickness in normal and glaucomatous eyes using optical coherence tomography.* Archives of Ophthalmology, 1995. **113**(5): p. 586.

85. Schuman, J.S., et al., *Optical coherence tomography and histologic measurements of nerve fiber layer thickness in normal and glaucomatous monkey eyes.* Investigative Ophthalmology and Visual Science, 2007. **48**(8): p. 3645-54.

86. Huang, X.-R. and R.W. Knighton, *Microtubules contribute to the birefringence of the retinal nerve fiber layer.* Investigative Ophthalmology and Visual Science, 2005. **46**(12): p. 4588-93.

87. Pocock, G.M., et al., *The Relationship between Retinal Ganglion Cell Axon Constituents and Retinal Nerve Fiber Layer Birefringence in the Primate.* Investigative Ophthalmology and Visual Science, 2009(11): p. 5238-5246.

88. Kong, G.Y.X., et al., *Mitochondrial dysfunction and glaucoma.* Journal of Glaucoma, 2009. **18**(2): p. 93-100.

89. Ju, W.-K., et al., *Elevated Hydrostatic Pressure Triggers Mitochondrial Fission and Decreases Cellular ATP in Differentiated RGC-5 Cells.* Investigative Ophthalmology and Visual Science, 2007. **48**(5): p. 2145-2151.

90. Abu-Amero, K.K., J. Morales, and T.M. Bosley, *Mitochondrial abnormalities in patients with primary open-angle glaucoma.* Investigative Ophthalmology and Visual Science, 2006. **47**(6): p. 2533-41.

91. Huang, X., et al., *Distortion of axonal cytoskeleton: an early sign of glaucomatous damage.* Investigative Ophthalmology and Visual Science, 2011. **52**(6): p. 2879-88.

92. Gaasterland, D. and C. Kupfer, *Experimental Glaucoma in the Rhesus Monkey.* Investigative Ophthalmology and Visual Science, 1974. **13**(6): p. 455-457.

93. Pederson, J. and D. Gaasterland, *Laser-Induced Primate Glaucoma. 1.Progression of Glaucoma.* Archives of Ophthalmology, 1984. **102**(11): p. 1689-1692.

94. Quigley, H.A. and R.M. Hohman, *Laser energy levels for trabecular meshwork damage in the primate eye.* Invest Ophth Visual, 1983. **24**(9): p. 1305-7.

95. Zangwill, L.M., et al., *Discriminating between normal and glaucomatous eyes using the Heidelberg retina tomograph, GDx nerve fiber analyzer, and optical coherence tomograph.* Archives of Ophthalmology, 2001. **119**(7): p. 985.

96. Mittag, T.W., et al., *Retinal damage after 3 to 4 months of elevated intraocular pressure in a rat glaucoma model.* Investigative Ophthalmology and Visual Science, 2000. **41**(11): p. 3451-9.

97. Fraser, J., V. Biousse, and N. Newman, *The Neuro-ophthalmology of Mitochondrial Disease.* Surv Ophthalmol, 2010. **55**(4): p. 299-334.

98. Ju, W., et al., *Elevated hydrostatic pressure triggers mitochondrial fission and decreases cellular ATP in differentiated RGC-5 cells.* Investigative Ophthalmology and Visual Science, 2007.

99. Beauvoit, B., et al., *Correlation between the light scattering and the mitochondrial content of normal tissues and transplantable rodent tumors.* Analytical biochemistry, 1995. **226**(1): p. 167-174.

100. Mourant, J.R., et al., *Mechanisms of light scattering from biological cells relevant to noninvasive optical-tissue diagnostics.* Applied optics, 1998. **37**(16): p. 3586-3593.

101. Pasternack, R.M., J.Y. Zheng, and N.N. Boustany, *Detection of mitochondrial fission with orientation‐dependent optical Fourier filters.* Cytometry Part A, 2011. **79**(2): p. 137-148.

102. Pasternack, R., J. Zheng, and N.N. Boustany, *Detection of mitochondrial fission with orientation‐dependent optical Fourier filters.* Cytometry Part A, 2010.

103. Chalut, K., et al., *Light scattering measurements of subcellular structure provide noninvasive early detection of chemotherapy-induced apoptosis.* Cancer research, 2009.

104. van der Meer, F., et al., *Apoptosis-and necrosis-induced changes in light attenuation measured by optical coherence tomography.* Lasers in Medical Science, 2010.

105. Farhat, G., et al., *Detecting apoptosis using dynamic light scattering with optical coherence tomography.* Journal of Biomedical Optics, 2011.

106. Yin, B., et al., *Degradation in the degree of polarization in human retinal nerve fiber layer.* Journal of biomedical optics, 2014. **19**(1): p. 016001-016001.

107. Huang, X., et al., *Reflectance Decrease Prior to Thickness Change of the Retinal Nerve Fiber Layer in Glaucomatous Retinas.* Investigative Ophthalmology and Visual Science, 2011.

108. Pyhtila, J., R. Graf, and A. Wax, *Determining nuclear morphology using an improved angle-resolved low coherence interferometry system.* Optics Express, 2003. **11**(25): p. 3473-3484.

109. Wax, A., et al., *Cellular organization and substructure measured using angle-resolved low-coherence interferometry.* biophysical journal, 2002. **82**(4): p. 2256-2264.

110. Iftimia, N., B.E. Bouma, and G.J. Tearney, *Speckle reduction in optical coherence tomography by "path length encoded" angular compounding.* Journal of biomedical optics, 2003. **8**(2): p. 260-263.

111. Desjardins, A., et al., *Angle-resolved optical coherence tomography with sequential angular selectivity for speckle reduction.* Optics Express, 2007. **15**(10): p. 6200-6209.

112. Desjardins, A., et al., *Speckle reduction in OCT using massively-parallel detection and frequency-domain ranging.* Optics Express, 2006. **14**(11): p. 4736.

113. Klein, T., et al., *Joint aperture detection for speckle reduction and increased collection efficiency in ophthalmic MHz OCT.* Biomedical Optics Express, 2013. **4**(4): p. 619.

114. Pyhtila, J.W., et al., *Fourier-domain angle-resolved low coherence interferometry through an endoscopic fiber bundle for light-scattering spectroscopy.* Optics letters, 2006. **31**(6): p. 772-774.

115. Mo, J., M. de Groot, and J.F. de Boer, *Focus-extension by depth-encoded synthetic aperture in Optical Coherence Tomography.* Optics Express, 2013. **21**(8): p. 10048-10061.

116. Werkmeister, R.M., et al., *Bidirectional Doppler Fourier-domain optical coherence tomography for measurement of absolute flow velocities in human retinal vessels.* Optics letters, 2008. **33**(24): p. 2967-2969.

117. Zotter, S., et al., *Visualization of microvasculature by dual-beam phase-resolved Doppler optical coherence tomography.* Optics Express, 2011. **19**(2): p. 1217.

118. Pedersen, C.J., et al., *Measurement of absolute flow velocity vector using dual-angle, delay-encoded Doppler optical coherence tomography.* Optics letters, 2007. **32**(5): p. 506-508.

119. Makita, S., et al., *Comprehensive in vivo micro-vascular imaging of the human eye by dual-beam-scan Doppler optical coherence angiography.* Optics Express, 2011. **19**(2): p. 1271-1283.

120. Hildebrand, G.D. and A.R. Fielder, *Anatomy and Physiology of the Retina*, in *Pediatric retina*. 2011, Springer. p. 39-65.

121. Pocock, G.M., et al., *The relationship between retinal ganglion cell axon constituents and retinal nerve fiber layer birefringence in the primate.* Investigative ophthalmology & visual science, 2009. **50**(11): p. 5238-5246.

122. Leclère, F., et al., *Microsurgery and liver research: Lumbricus terrestris, a reliable animal model for training?* Clinics and research in hepatology and gastroenterology, 2013. **37**(2): p. 166.

123. Gad, S.C., *Animal models in toxicology*. 2006: CRC Press.

124. Drewes, C., *Functional organization of the nervous system in Lumbriculus variegatus*. 2002.

Vita

Bingqing Wang was born in Shenyang, Liaoning, China in 1987. He obtained the B.E. degree in Biomedical Engineering in 2009 from Zhejiang University, Hangzhou, China. In August 2009, Bingqing Wang entered the Ph.D. program in the Department of Biomedical Engineering at The University of Texas at Austin, under the joint supervision of Dr. Henry G. Rylander III and Dr. Thomas E. Milner. His research interests include medical imaging, modeling, and image processing.

Permanent email: wbq1987@gmail.com

This dissertation was typed by the author.